

Towards the production of core-shell nanoparticles with fluidized bed ALD

Proefschrift

ter verkrijging van de graad van doctor
aan de Technische Universiteit Delft,
op gezag van de Rector Magnificus prof.ir. K.C.A.M. Luyben;
voorzitter van het College voor Promoties,
in het openbaar te verdedigen op
22 januari om 12.30 uur

door
Arjen Peter DIDDEN,
Chemisch ingenieur,
Geboren te Koudekerk aan den Rijn

Dit proefschrift is goedgekeurd door de Promotoren :

Prof. dr. B. Dam en Prof. dr. ir. R. van de Krol

Samenstelling promotiecommissie:

Rector Magnificus

Voorzitter

Prof. dr. B. Dam

Technische Universiteit Delft, promotor

Prof. dr. ir. R. van de Krol

Helmholtz-Zentrum Berlin für Materialien und Energie
GmbH en Technische Universität Berlin, Duitsland,
promotor

Onafhankelijke leden:

Prof. dr. S.D. Tilly

University of Zürich, Zwitserland

Prof. dr. C. Detavernier

Universiteit Gent, België

Prof. dr. ir. W.M.M. Kessels

Technische Universiteit Eindhoven

Prof. dr. A. Schmidt-Ott

Technische Universiteit Delft

Dr. ir. J.R. van Ommen

Technische Universiteit Delft

Prof dr. F.M. Mulder

Technische Universiteit Delft, Reservelid

© Arjen Peter Didden, 2015

The research work presented in this thesis was funded by the Thin Film Nanomanufacturing program of the Dutch Technology Foundation STW (project 10016) and supported by NXP (Veldhoven, the Netherlands) and AST b.v. (Leeuwarden, the Netherlands).

The artwork on the cover is by Desiré Cok.

CONTENTS

1	INTRODUCTION	5
1.1	NANOPARTICLES	7
1.2	ATOMIC LAYER DEPOSITION	9
1.2.1	<i>Basic principles of ALD</i>	<i>9</i>
1.2.2	<i>ALD of TiO₂</i>	<i>11</i>
1.2.3	<i>ALD of TiN</i>	<i>14</i>
1.3	FLUIDIZATION OF NANOPARTICLES	16
1.4	THESIS STRUCTURE	20
2	TITANIUM NITRIDE: A NEW OHMIC CONTACT MATERIAL FOR N-TYPE CDS	21
2.1	INTRODUCTION	23
2.2	EXPERIMENTAL	24
2.3	RESULTS AND DISCUSSION	25
2.3.1	<i>Texture of the CdS film</i>	<i>25</i>
2.3.2	<i>The TiN/CdS contact</i>	<i>26</i>
2.3.3	<i>Mott-Schottky analysis of the CdS films</i>	<i>29</i>
2.3.4	<i>Au/TiN/CdS diode</i>	<i>34</i>
2.4	CONCLUSIONS	37
3	PHOTOCORROSION MECHANISM OF TiO₂-COATED PHOTOANODES	39
3.1	INTRODUCTION	41
3.2	EXPERIMENTAL	43
3.3	RESULTS AND DISCUSSION	44
3.4	CONCLUSIONS	55
4	FLUIDIZED-BED ATOMIC LAYER DEPOSITION REACTOR FOR THE SYNTHESIS OF CORE-SHELL NANOPARTICLES	57

4.1	INTRODUCTION	58
4.2	APPARATUS DESCRIPTION	59
4.2.1	<i>Precursor dosing</i>	60
4.2.2	<i>Reactor</i>	61
4.2.3	<i>Residual gas treatment</i>	63
4.2.4	<i>Process control</i>	64
4.2.5	<i>Safety</i>	65
4.2.6	<i>Precursor selection</i>	66
4.3	EXPERIMENTAL VERIFICATION	66
4.4	CONCLUSION	74
5	DEPOSITION OF CONDUCTIVE TIN SHELLS ON SiO₂ NANOPARTICLES WITH A FLUIDIZED BED ALD REACTOR	75
5.1	INTRODUCTION	77
5.2	EXPERIMENTAL	78
5.3	RESULTS AND DISCUSSION	80
5.3.1	<i>Oxidation of TiN Shell</i>	80
5.3.2	<i>Film growth rate</i>	81
5.3.3	<i>Shell composition and structure</i>	87
5.3.4	<i>Shell conductivity</i>	90
5.4	CONCLUSIONS	92
5.5	APPENDIX	93
6	SUMMARY AND OUTLOOK	95
7	SAMENVATTING EN VOORUITBLIK	99
	REFERENCES	103
	DANKWOORD	111
	CURRICULUM VITAE	113
	PUBLICATIONS	114

1 INTRODUCTION

1.1 Nanoparticles

Already since the 9th century, copper nanoparticles have been used to give pottery and glassware a “magic” shiny luster, making it nanotechnology *avant le lettre*.¹ It was, however, until after the development of modern-day tools like electron microscopy and atomic force microscopy that we finally begin to understand nanostructures. This initiated the search for nanoparticle applications.

In most applications, nanoparticles are used for their large specific surface area.² Catalyst nanoparticles have a high activity and reduce the amount of material required.^{3,4} In Li-ion batteries, nanostructures are used for their mechanical stability upon charge-discharge cycling and for their large reactive surface area.⁵ Other applications where feature size is the most important factor are hydrogen storage,⁶ sensors,⁷ electronics,^{8, 9} and medicines.¹⁰⁻¹⁸

Another reason to use nanoscale is that upon decreasing the feature size, the material properties start to differ from bulk materials. This is called the quantum size effect. Semiconductor quantum dots, which are nanocrystals with a typical diameter <10 nm, are the most exciting example of size-dependent material properties. The band gap of quantum dots is dependent on the size of the particles becoming larger with decreasing diameter. The quantum size effect is also thought to enhance the phenomenon of multiple exciton generation (MEG), a process in which two electron-hole pairs are created with a single photon.^{19, 20} This, combined with the variable band gap, high quantum yields²¹ and easy preparation methods, makes them ideal starting materials for third generation photovoltaic cells.²²

Even though nanoparticles seem promising, they also have their limitations. Due to their large surface area, many nanoparticles are highly reactive and hence need to be protected against environmental influences. By coating the particle with a thin inert layer, creating a so-called core-shell particle, provides an elegant solution for many

applications.²³ Applications of such core-shell particles can already be found in sunscreens, printable inks,⁹ bio-compatible quantum dots,²⁴ and MRI contrasting agents.²⁵

Besides protection, the core-shell structure may also enhance the functional properties of nanoparticles in other ways. For example, shells may change the color of nanoparticles, increase their solubility, or affect the life time of excitons in quantum dots.^{26, 27} Furthermore, if shells of precious metal catalysts (e.g. Pt or Ni) are deposited on inexpensive carriers such as SiO₂ or on metal cores, the catalytic activity per kg of metal can be greatly enhanced.^{28, 29} Depositing a conductive layer on nanoparticles helps to make electrical contacts on nanoparticle devices such as solar cells and sensors, and thus increase the conductivity and performance of nanoparticle-based solar cells.

Shells of core-shell particles have to meet certain requirements to be effective. First of all, the material has to be chemically inert with respect to the core as well as the environment in which it is to be used. The use of corrosive chemicals and high temperatures during shell deposition are to be avoided. Furthermore, the coating should be homogeneous and thick enough to provide protection, yet thin enough to maintain the core functionality.

In most cases, the shells are deposited using a wet-chemical method by precipitation of the shell on the cores, or by simultaneous synthesis of core and shell. With these methods it is, however, difficult to control the shell thickness and homogeneity. As a result, the product is often contaminated with uncoated particles and particles that consist entirely of the shell material.²⁷ Furthermore, precipitation reactions are difficult to scale up to the large production volumes required for practical applications.²⁷

In this thesis, the use of Fluidized Bed Atomic Layer Deposition (FB-ALD) to deposit conductive and protective shells on nanoparticles is investigated. This technique, first developed by Weimer et al.,³⁰ serves as an alternative to wet-chemical synthesis techniques. It combines the possibility of handling nanoparticles and the scalability of fluidized bed reactors with the precise thickness control, coating homogeneity, and versatility of Atomic Layer Deposition (ALD). Figure 1-1 gives an indication of the typical

differences of particles coated with FB-ALD and precipitation from a solution. The FB-ALD grown shells are much thinner and more uniform than the solution-grown shells.

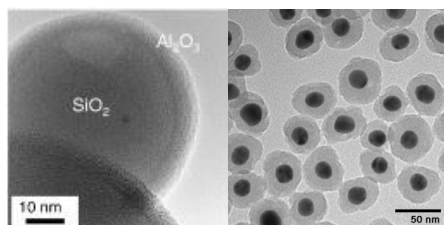


Figure 1-1: Difference between ALD coated particles and particles coated with a precipitation reaction. Left hand side image shows SiO₂-Al₂O₃ core-shell particles by FB-ALD,³¹ right hand side image shows Au@SiO₂ particles synthesized with a precipitation reaction.³²

To understand the FB-ALD process, the principles of ALD as well as fluidized bed reactors should be properly understood. The ALD process is described in section 1.2, where special attention is given to the deposition of TiO₂ and TiN. In section 1.3, the principles of fluidized bed reactors are described. Section 1.4 gives the main goals and outline of this thesis.

1.2 Atomic layer deposition

Atomic Layer Deposition (ALD) is a thin film deposition technique based on the self-limiting adsorption of suitable metal-precursors. By adding metal- and non-metal precursors in a sequential order and with sufficient purging in between the precursors, self-limiting layer-by-layer growth can be obtained. ALD has been successfully used to deposit thin films of a wide variety of materials, ranging from pure metals and metal oxides to nitrides and sulfides.³³ In this section, the basic principles and limitations of ALD in general, as well as the particular conditions for the deposition of TiO₂ and TiN, will be described.

1.2.1 Basic principles of ALD

An ALD cycle typically consists of four steps: metal precursor adsorption, reactor chamber purge, precursor oxidation, and a second reactor chamber purge. During the first step, the

metal precursor vapor is brought into the reactor. The precursor attaches to the substrate surface by chemisorption. After all surface sites are covered with precursor molecules, the chemisorption of molecules will stop. At this stage, increasing the precursor dose does not further increase the growth rate, i.e., the growth is saturated. This self-limiting adsorption mechanism is the basis for the excellent control over the growth process of ALD layers. After saturating the surface, the reactor is purged to remove all remaining precursor vapor and reaction by-products. The second pulse is used to oxidize (in case of metal oxide deposition) or reduce the adsorbed precursor molecule (in case of metal deposition). After completion of the reaction, the reactor is purged again and a monolayer has formed. In order to increase the layer thickness the cycle must be repeated until the desired thickness is achieved. Typically, the amount of precursor needed to saturate the surface is determined by varying the precursor exposure (pressure \times time) and measuring the resulting growth rate. A typical result of such an experiment is given in Figure 1-2.

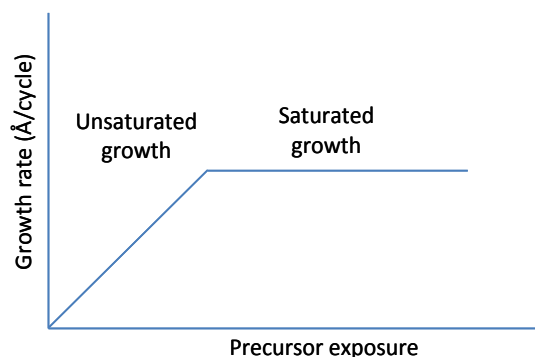


Figure 1-2: Typical relation between precursor exposure and growth rate

Precursors need to meet a number of criteria to be suitable for ALD processes. First of all the metal precursor should be able to react with the surface in a self-limiting manner. This means that the chemisorption reaction should be irreversible and that the precursor cannot react with itself. The precursor should also be stable under the reaction conditions, while it has to be highly reactive with the second precursor. Both precursors should have

a sufficiently high vapor pressure in order to reduce the processing time. This, however, also depends on the reactor system that is used.

An important parameter is the deposition temperature window. The effect of temperature on the growth rate is rather complex and involves several different effects. Low deposition temperatures can cause low reactivity of the precursors, resulting in low growth rates. However, at low temperatures, water may condensate on the sample surface, causing uncontrolled growth. Too high temperatures, on the other hand, can cause thermal decomposition of the precursors, also resulting in growth rates higher than 1 monolayer per cycle. Too high temperatures can also cause precursor desorption, resulting in lower growth rates. The effect of temperature is summarized in Figure 1-3.

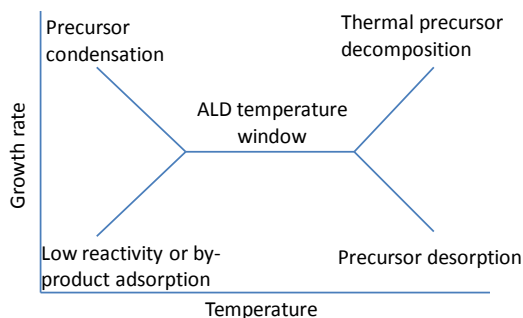
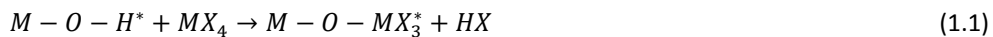


Figure 1-3: Overview of the ALD temperature window.

1.2.2 ALD of TiO_2

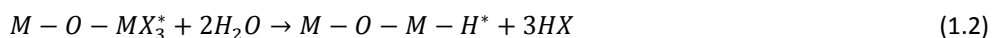
TiO_2 is a dielectric material that is widely used as in microelectronics, pigments, cosmetics, and photocatalysts. In this thesis, TiO_2 is deposited on SiO_2 nanoparticles as a test-case for the FB-ALD reactor and as a protective anti-corrosion layer on CdS films. To obtain the desired homogeneous TiO_2 coatings, the deposition process should be well understood. A short review describing the deposition chemistry and most important deposition conditions is given below.

The generic ALD reaction mechanism of TiO_2 is given below. The Ti precursor (TiX_4) reacts with an OH terminated surface site (denoted with an *) in the following manner.



Because each surface site can only react with one precursor molecule, the amount of adsorbed TiX_4 is limited to the amount of surface sites available. Table 1-1 gives an overview of the most commonly used ALD precursors.

Once the surface is saturated and the reactor is purged, the adsorbed precursor is oxidized. This can be achieved by different methods (cf. Table 1-1). In this thesis water is always used as oxidizing agent, and the reaction can be described as follows:



In this step, all ligands are removed from the metal atom and replaced by new oxygen atoms. After reaction completion and reactor chamber purge, the surface is OH-terminated again and the deposition cycle can be repeated to create thicker layers.

To select the optimal deposition process, a few selection criteria need to be weighed. The most important criteria are the growth rate, the acceptable deposition temperature, the formation of corrosive by-products, and the quality of the deposited layer in terms of homogeneity, morphology and impurities. For this thesis, the TiO_2 coatings are mainly used as test-case for the FB-ALD reactor and as protective anti-corrosion layer. For these applications, the film growth rate, homogeneity, and morphology, as well as the formation of corrosive by-products are the most important parameters.

TiO_2 growth rates are typically in the order of $0.1 - 1.8 \text{ \AA/cycle}$, which is much lower than the expected monolayer growth (anatase TiO_2 has lattice parameters of 3.7845 and 9.5143 \AA).⁴⁵ This is due to steric hindrance between the adsorbed precursor molecules. The ligands attached to the Ti atom block neighboring adsorption sites, limiting the density of adsorbed precursor molecules. However, the fact that growth rates with TDMAT (large ligands) are higher than $TiCl_4$ (small ligands), indicates that other factors, such as water adsorption at low temperatures and thermal decomposition of TDMAT, are also involved.⁴⁶

Table 1-1: Overview of TiO₂ and TiN ALD precursors. TDMAT is tetrakis (dimethylamino) titanium, TTIP is titanium tetra-isopropoxide.

<i>Precursor</i>	<i>Oxidizer</i>	<i>Temperature</i> °C	<i>Growth rate</i> Å/cycle	<i>Refs.</i>
TiCl ₄	H ₂ O	200-300	0.4-0.54	34-36
TiCl ₄	O ₂ plasma	100-200	1.35	37
TiI ₄	H ₂ O		1.8	38
TDMAT	H ₂ O	30-330	0.6-1.5	39, 40
TDMAT	O ₂ plasma	30-250	0.6-1.8	39, 41
TDMAT	H ₂ O plasma	30-300	0.6-1.6	39
TTIP	O ₃	150-250	0.52	42
TTIP	H ₂ O ₂	100-250	1.2	43
TTIP	H ₂ O	50-325	0.1-0.6	39, 43, 44
TTIP	H ₂ O plasma	50-325	0.4-0.5	39
TTIP	O ₂ plasma	50-325	0.4	39

The morphology and structure of the deposited films strongly depend on the substrate and the reaction conditions. TiO₂ film growth during the initial cycles on HF-cleaned silicon, GaAs, mica and metals is mostly island-like, giving films with a relatively high roughness. ALD on RCA-cleaned Si or Al₂O₃ gives more homogeneous films. This suggests that an O-H terminated substrate surface (RCA-cleaned Si has a thin oxide film) is crucial in obtaining homogeneous films.^{35, 47-50}

Most ALD-TiO₂ films are amorphous or only partly crystalline. The crystalline fraction increases with the amount of cycles and the deposition temperature. Anatase can be formed at temperatures > 150 °C with TiCl₄ and at temperatures > 250 °C with TDMAT. With TTIP, the film remains amorphous. The layer thickness is also important. Thin layers (<1000 cycles) typically are amorphous.

In summary, TiCl₄, H₂O and high temperatures are preferred for the deposition of crystalline layers. Major drawbacks of TiCl₄ are, however, the formation of corrosive gaseous HCl and Cl impurities in the TiO₂ layer. Since we need to avoid this, TDMAT and H₂O are used for the work described in this thesis.

1.2.3 ALD of TiN

Titanium nitride is a conductive material, widely used in the electronics industry. Because of its high conductivity, it can act as electrode material in, for example, CMOS technology and as a diffusion barrier between Si devices and Cu and W contacts.⁵¹ Because ALD provides excellent control over thickness and the ability to deposit highly conformal layers in high aspect ratio pores (which is required for the ever decreasing dimensions in microelectronics⁵²), TiN-ALD is intensely investigated.

In this work, TiN is used as Ohmic contact material for CdS films and used to demonstrate that nanoparticles can be coated with conductive coatings in the fluidized bed ALD reactor. The most important requirements of TiN for this research are the growth rate and the conductivity of the films. A short review of TiN deposition conditions influencing this is given below.

The precursors that are used in TiN-ALD are essentially the same as in TiO₂. The reaction mechanism is, however, rather different. In contrast to TiO₂, the Ti ion in TiN has a charge of 3+. This means that the Ti needs to be reduced during one of the half-reactions. To aid this reduction step, sometimes reducing agents such as Zn or trimethylaluminium (TMA) are added. The growth rates reported in literature vary from 0.1-3.5 Å/cycle. For both precursors, the growth rate depends on the deposition temperature. A higher temperature gives a higher growth rate.⁵³⁻⁵⁶

The exceptionally high growth rates with TDMAT are obtained at relatively high deposition temperatures (>200 °C). The fact that the growth-per-cycle exceeds one monolayer of TiN indicates that the adsorption of TDMAT is not self-limiting at high temperatures. High growth rates can be caused by thermal decomposition of TDMAT at temperatures > 200 °C⁴⁶ or by excessive NH₃ adsorption on the TiN surface.⁵⁷

Table 1-2 gives an overview of the deposition processes described in literature. The growth rates reported in literature vary from 0.1-3.5 Å/cycle. For both precursors, the growth rate depends on the deposition temperature. A higher temperature gives a higher growth rate.⁵³⁻⁵⁶

The exceptionally high growth rates with TDMAT are obtained at relatively high deposition temperatures (>200 °C). The fact that the growth-per-cycle exceeds one monolayer of TiN indicates that the adsorption of TDMAT is not self-limiting at high temperatures. High growth rates can be caused by thermal decomposition of TDMAT at temperatures > 200 °C⁴⁶ or by excessive NH₃ adsorption on the TiN surface.⁵⁷

Table 1-2: Overview of most used precursors for TiN-ALD. In this table, TMA is trimethylaluminum

<i>Precursor</i>	<i>Reducing agent</i>	<i>Temperature °C</i>	<i>Growth rate Å/cycle</i>	<i>Refs.</i>
TiCl ₄	NH ₃	300-425	0.1-0.26	53, 58, 59
TiCl ₄	N ₂ -H ₂ plasma	100-400	0.25-0.65	54, 58, 60
TiCl ₄	NH ₃ and TMA	275	0.45	61
TDMAT	NH ₃	150-300	0.5-3.5	55
TDMAT	NH ₃ plasma	50-300	0.5-3.5	55
TDMAT	N ₂ plasma	50-350	0.5-4	55

The growth rate of TiN is not constant throughout the process. Most TiCl₄ processes suffer from a reduced growth rate during the first cycles.^{58, 59, 62} For TDMAT, however, growth rate enhancement is reported for the first cycles.⁵⁵ The initial growth of TiN on Si wafers is island-like and it takes several cycles for the TiN layer to be completely closed.⁶² The precursors in the reaction preferably adsorb on TiCl_x and NH_y groups rather than on SiO₂ surfaces. This growth mode eventually leads to polycrystalline, low density films. The TDMAT process seems to give the lowest-density TiN⁵⁷ (3.0 g/cm³, whereas bulk TiN has a density of 5.22 g/cm³)⁶³ the TiCl₄ process gives densities of ~4 g/cm³.⁶²

The island growth and high porosity of the TiN films have their effect on the conductivity of the material. Because the intended use of the TiN coatings is to serve as electric contact material, the resistivity of the material should be as low as possible. The resistivity - usually a material constant independent of size of the test piece - decreases sharply with decreasing film thicknesses (< 10 nm). This is believed to be caused by a poor contact between TiN islands (the concentration is below the percolation threshold) that make up very thin films.^{58, 60}

The island-like growth and concomitant porosity of ALD-TiN also influences the conductivity of the films in another way. TiN quickly reacts with air, forming a 1-2 nm passivation layer.⁶⁴ In porous films, the oxygen diffuses into the ALD-TiN layer and may oxidize a significant fraction of the TiN film. Large concentrations of O impurities that could not be attributed to the deposition process are found in layers of ALD-TiN.⁵⁷ The rapid oxidation of pristine TiN as well as the diffusion of O₂ into the TiN film have been observed in this work and described in chapter 5.

Films deposited with TiCl₄ usually have a lower resistivity than films deposited with TDMAT.^{51, 55, 57, 58} Also, the density and amount of impurities are lower for films deposited with TiCl₄.^{51, 65} Therefore this is the process that is mostly used. There are, however, some drawbacks in the use of TiCl₄ processes, the most important being the by-products of the deposition reaction. The main by-product is HCl, which is a corrosive gas and reported to corrode Cu substrates during deposition.⁵³ Another issue is the reaction between NH₃ and HCl that results in the formation of NH₄Cl, which leaves a powdery deposit on the sample.⁵³ For the work described in this thesis, the formation of corrosive gasses should be absolutely avoided. It was therefore decided to avoid the use of TiCl₄, and instead use TDMAT as a precursor for TiN films.

1.3 Fluidization of nanoparticles

In the FB-ALD reactor, ALD is carried out on particles floating in a fluidized bed reactor. This type of reactor is widely used in industrial processes where gas and solids need to be brought into contact with each other. Applications vary from large cracking reactors in oil refineries, in which evaporated oil fractions react with catalyst particles, to the production of pharmaceuticals, in which fluidized beds are used to dry medicines. In this section, the basic principles of fluidization and the specific aspects of nanoparticles fluidization with low-density gasses will be discussed and key process parameters are given.

In a fluidized bed reactor, a fluid (gas or liquid) is blown through a bed of loose particles. Because in this thesis gas will be used as fluidizing agent, the description will focus on the fluidization of particles by a gas.

In a fluidized bed reactor, the gas enters the bed via a distributor located at the bottom of the reactor. The gas flows upward through the particle bed and exerts an upwards force on it. The particles are pulled downwards by their own weight. At low gas flows, the upwards force will not be high enough to overcome the gravitational pull on the particle bed and the gas will find its way through the bed via small channels. Upon increasing the gas flow, the upwards force will become higher and at some point it will be high enough to balance the downwards force of the particles. The particles will then start to move through the reactor chamber. This is called the fluidized state. If the gas flow is further increased, the bed expands; waves and gas bubbles will start to appear in the fluidized bed. If the flow becomes too high, the particles will be blown out of the reactor. The three stages of fluidization are summarized in Figure 1-4.

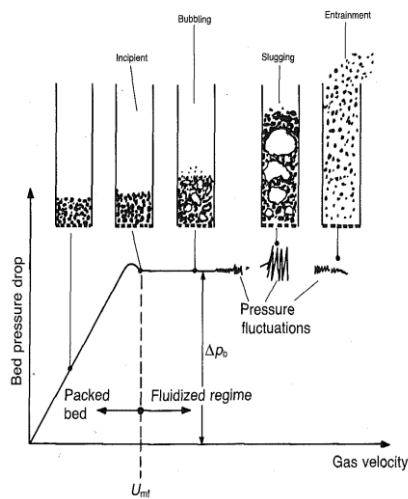


Figure 1-4: different regimes of fluidization and the corresponding Δp (from Kunii and Levenspiel⁶⁶)

The minimum gas velocity at which the bed is still in its fluidized state (u_{mf}) can be determined by measuring the pressure drop between the bottom and the top of the particle bed (Δp). At low gas flows, the gas will channel through the fixed bed of particles and Δp will depend in a non-linear fashion on the gas velocity as described by the Ergun equation.⁶⁶ At velocities $> u_{mf}$, Δp will be independent of the gas velocity and

approximately equal to the static pressure caused by the particle weight. This is calculated with the following equation, in which $m_{particles}$ is the particle mass, g the gravitational constant (9.81 m/s^2), and $A_{reactor}$ the surface area of the reactor vessel:

$$\Delta p \approx \frac{m_{particles}g}{A_{reactor}} \quad (1.3)$$

To estimate the minimum fluidization velocity before doing an experiment, a balance of the upwards drag force exerted by the gas and the weight of the bed should be made. The equation for u_{mf} of small particles is⁶⁶

$$u_{mf} = \frac{d_p^2(\rho_s - \rho_f)g}{150\mu} \frac{\varepsilon_{mf}^3 \sigma^2}{1 - \varepsilon_{mf}} \quad (1.4)$$

In this equation, d_p is the particle diameter (m), ρ_s and ρ_f the density of solid and gas (kg/m^3), μ the viscosity of the gas (Pa s), ε_{mf} the bed voidage at incipient fluidization (-) and σ the shape factor of the particles (1 for spherical particles).

Even though ε_{mf} —and therefore also u_{mf} —is difficult to determine, several important trends can be found in this equation. For equation 1.4 to be valid, the gas must have a measurable viscosity. However, at the low gas pressures usually applied in ALD processes, this is not trivial. An easy way to estimate the nature of the flow through a tube is the Knudsen number (Kn), which is defined as

$$Kn \equiv \frac{\ell}{d_{tube}} \quad (1.5)$$

In this equation, d_{tube} (m) is the tube diameter and the gas molecules mean free path ℓ is calculated with the equation

$$\ell = \frac{k_B T}{\sqrt{2} \pi d_{molec}^2 p} \quad (1.6)$$

Here, k_B is the Boltzmann constant ($1.381 \times 10^{-23} \text{ J/K}$),⁶³ T the temperature (K), d_{molec} the molecular diameter of the gas (m), and p the pressure (Pa). At $Kn \gg 1$, the flow is

molecular, meaning that the gas has no viscosity and particles cannot be fluidized. At $Kn < 1$, the flow is viscous and fluidization can occur.⁶⁷

The viscosity of low density gasses depends strongly on temperature, but is independent of the pressure.⁶⁸ The density of gasses is typically negligible when compared to the density of solids. If we use these assumptions in the equation 1.4, we learn that u_{mf} is largely independent of the gas pressure.

The estimates for the u_{mf} of nanoparticles usually differ by a few orders of magnitude from the measured values. For example, spherical 20 nm SiO₂ dioxide particles ($\rho_s = 2100 \text{ kg/m}^3$)⁶³ fluidized with Ar at room temperature and atmospheric pressure ($\mu = 2.1 \times 10^{-5} \text{ Pa s}$ and $\rho_f = 1.8 \text{ kg/m}^3$)⁶³ have a $u_{mf} < 3 \times 10^{-9} \text{ m/s}$, whereas the measured u_{mf} is usually in the order of a 10^{-2} m/s .⁶⁹⁻⁷³

This orders-of-magnitude difference is caused by strong agglomeration due to strong London-van der Waals forces. Typical nanoparticle agglomerates have a diameter of 100-500 μm , depending on the material. These agglomerates tend to have a loose, open structure and a very low density.⁶⁹

The strong agglomeration forces make nanoparticles often difficult to fluidize, and some form of assistance is needed. Among the assistance methods are vibrating beds, centrifugal force, stirred columns, electric and magnetic fields and addition of chemicals.⁷⁴

Even though nanoparticles always agglomerate, the agglomerates are usually loose. During the process they continuously break up in smaller agglomerates and re-agglomerate with other particles. Due to this dynamic agglomeration process, all sides of each particle become available precursor adsorption. This makes the complete coating of nanoparticles by ALD in a fluidized bed possible, despite the agglomerated nature of the nanoparticles.⁶⁹

In summary, nanoparticles are generally present in the form of large agglomerates but ALD is still possible. The size and density of these agglomerates as well as the gas viscosity

determine the minimum velocity required to fluidize the particle bed. To improve the fluidization, assistance is often required.

1.4 Thesis structure

One of the central questions in this thesis is whether a powder of loosely-agglomerated nanoparticles can be conformally coated with protective and electrically conducting layers. To systematically address this, the problem is divided into four sub-questions. The first question is whether the contact between the conductive layer and the nanoparticle material is Ohmic. This question is answered for TiN and CdS in chapter 2.

In chapter 3, we investigate whether ALD films can be used as protective barriers and how corrosion does occur in coated semiconductor films. The use of TiO₂ layers to protect CdS films against photocorrosion is used as model system.

In chapter 4, the construction of a FB-ALD reactor is described in detail. Chemical analysis and TEM measurements are used to confirm that SiO₂-TiO₂ core-shell nanoparticles can be synthesized in the reactor.

In chapter 5, we report on the deposition of TiN-layers on SiO₂ nanoparticles in a FB-ALD reactor. Chemical analysis, XPS, and TEM are used to show that indeed TiN is deposited. The conductive nature of the coatings is demonstrated with 2-point resistance measurements.

2 TITANIUM NITRIDE: A NEW OHMIC CONTACT MATERIAL FOR N-TYPE CDS*

In devices based on CdS, indium is often used to make Ohmic contacts. Since indium is scarce and expensive, suitable replacement materials need to be found. In this work we show that sputtered titanium nitride forms an Ohmic contact with n-type CdS. The CdS films, deposited with chemical bath deposition, have a hexagonal crystal structure and are polycrystalline, mostly with a (002) texture. The thickness of the films is ~ 600 nm, and the donor density is $1.9 \times 10^{16} \text{ cm}^{-3}$. The donor density increases to $1.5 \times 10^{17} \text{ cm}^{-3}$ upon annealing. The contact resistivity of sputtered TiN on CdS is found to be $4.7 \pm 0.6 \Omega \text{ cm}^2$. This value is sufficiently small to avoid large resistive losses in most CdS device applications. To demonstrate the use of TiN in a CdS device, a Au/CdS/TiN Schottky diode was constructed. The diode has a potential barrier of 0.69 V and an ideality factor of 2.2.

* This chapter has been published: Arjen Didden, Hemme Battjes, Raymond Machunze, Bernard Dam, and Roel van de Krol, *Journal of Applied Physics* **110** (2011) 033717

2.1 Introduction

CdS is an n-type semiconductor with a direct band gap of 2.42 eV⁶³ that can be employed in a large variety of optoelectronic devices, such as highly efficient CIGS⁷⁵ and CdTe⁷⁶ solar cells and photodetectors, as well as gas sensors,^{77, 78} field effect transistors,^{79, 80} and LEDs.⁸¹ For most of these applications indium is used to form an Ohmic contact with CdS. However, since indium is a relatively scarce metal and at the same time a major component of transparent conducting oxides used in devices such as solar cells, touch screens, O-LEDs and flat panel displays, it is becoming increasingly expensive. This drives the search for alternative Ohmic contact materials that can replace indium.

We propose the use of titanium nitride (TiN) as an alternative for indium in n-type CdS devices. TiN is a well-known material that is both relatively low-cost and widely used in several applications, such as wear-resistant coatings on cutting tools, and Cu diffusion barriers in Si technology. Moreover, it is a material that can be deposited at temperatures as low as 60 °C by Metal-Organic Atomic Layer Deposition (MO-ALD).⁵⁷ This could make it a suitable contact material for applications based on CdS quantum dots, such as quantum dot solar cells, in which low-temperature processing is required to prevent the nanoparticles from sintering and losing their quantum-size effects.⁸²

Reported work functions of TiN vary between 3.5 and 4.4 eV.^{83, 84} This is slightly lower than the reported electron affinities for CdS, which range between 4.4 and 4.8 eV.^{85, 86} Based on these values, TiN is expected to form an Ohmic contact with n-type CdS. Obtaining an Ohmic contact in real devices is, however, not trivial. Due to Fermi-level pinning induced by interface defect states, Schottky-type potential barriers are often formed where Ohmic contacts would be expected. This is illustrated by metals such as Al^{87, 88} and Zn,⁸⁹ which form a Schottky contact with n-type CdS despite their lower work functions. In this paper we investigate the electrical properties of the TiN/CdS contact, and show that an Ohmic contact is indeed formed.

2.2 Experimental

The CdS films were grown on FTO-coated glass (fluorine-doped tin dioxide, $15 \Omega/\square$, TEC 15, Libbey-Owens-Ford) and glass substrates (2×3 cm) by Chemical Bath Deposition (CBD).⁹⁰⁻

⁹² The substrates were cleaned by ultrasonic rinsing in acetone and ethanol, followed by a 5 s dip in a dilute HCl solution (17.5 %) and subsequent rinsing with ultrapure deionized water (Milli-Q, $18.2 \text{ M}\Omega\text{cm}$). After cleaning, the substrates were submerged in 60 ml ultrapure water that was heated to 70°C . CdS films were deposited by adding reactants from aqueous stock solutions (all prepared in ultrapure water) in the following order: 300 μl of 0.5 M CdCl_2 hemi-pentahydrate (Aldrich, ACS reagent grade), 1320 μl 2 M NH_4Cl (JT Baker, 99.5%), and 3800 μl of 13.2 M NH_4OH solution (JT Baker). After 15 minutes of homogenization with a magnetic stirrer, 1800 μl of 1M thiourea (Aldrich, ACS reagent grade) was added slowly. After 60 minutes, the samples were taken out of the bath and cleaned ultrasonically in ultrapure water for 30 seconds and rinsed with ultrapure water to remove loose particle deposits. Thicker layers were obtained by repeating the cycle of deposition, ultrasonic cleaning, and rinsing multiple times.

TiN contacts were deposited on CdS films and glass substrates by reactive unbalanced magnetron sputtering in an industrial PVD system (Hauzer HC 750). The substrate temperature was $200 \pm 20^\circ\text{C}$. Prior to the deposition of TiN, the substrates were plasma-etched (4×10^{-3} mbar Ar) to remove impurities from the surface. The substrates performed a planetary motion in front of a $600 \times 120 \text{ mm}^2$ titanium target; the nitrogen and argon flows during deposition were 37 sccm and 115 sccm, respectively, yielding a deposition pressure of 4×10^{-3} mbar. The base pressure of the system was 4×10^{-5} mbar. The film was ion-bombarded during growth by applying a substrate bias voltage of -125 V in order to increase the density. The target power was 5 kW and the target voltage was 600 V, resulting in a deposition rate of 4.5 nm/s. Typical deposition times were 44 minutes, resulting in $\sim 200 \text{ nm}$ thick films. For comparison with the TiN contacts, Au Schottky contacts were deposited by thermal evaporation from a resistively heated tungsten boat in a home-built vacuum chamber having a base pressure of 10^{-7} mbar.

Film thickness values were measured with a Dektak 3 Profilometer. Grazing incidence X-ray diffraction spectra were measured with a Bruker D8 Advance diffractometer using Cu- K_{α} radiation and an incident angle of 0.9°.

Current-voltage measurements were carried out with an EG&G 283 potentiostat (Princeton Applied Research). Voltage-dependent impedance measurements were carried out with a Solartron 1255 frequency response analyzer in combination with the EG&G 283 potentiostat. The contact resistivity of the TiN/CdS contacts was measured with four-point probe measurements using a Keithley 2001 multimeter and the EG&G 283 potentiostat, using spring-loaded gold contact pins.

2.3 Results and discussion

2.3.1 Texture of the CdS film

The grazing incidence X-ray diffraction spectrum of the CdS film on a FTO substrate is shown in Figure 2-1. Two phases, cubic and hexagonal, have been reported in the literature on chemical bath deposition of CdS.^{91, 93-95} The diffraction pattern of our sample reveals a strong CdS peak at 26.7° and a very small peak at 48°, which correspond to the (002) and (103) planes of hexagonal CdS, respectively. No traces of the cubic phase are observed. The diffraction pattern indicates a preferred growth direction with the c-axis oriented perpendicular to the surface. The same (002) orientation is found for films grown on uncoated glass substrates, and has also been observed by other authors.⁹³⁻⁹⁵

For hexagonal CdS, a (002) orientation implies that the closest-packed lattice planes are exposed to the reaction mixture during growth. We attribute this to an atom-by-atom growth mechanism, as reported previously by Ortega-Borges et al. for chemical bath-deposited CdS.⁹⁶ The reversible adsorption of ions from the solution allows the ions to find the energetically most favorable sites, analogous to surface diffusion processes that occur at sufficiently high substrate temperatures during physical vapor deposition (e.g. sputtering).⁹⁷ The dynamic adsorption-desorption equilibrium in the CBD solution leads to recrystallization during film growth, and the growing film aims for the thermodynamically

most stable configuration. Since the closest-packed lattice planes have the lowest surface energy, columnar growth with the (002) planes parallel to the surface will occur. This growth mechanism is analogous to the ‘Type II’ growth described by Mahieu et al. for sputter-deposited films.⁹⁷ The deposited films have a clear and homogeneous appearance, which is indeed consistent with such a slow atom-by-atom growth. The thickness of the films after three deposition cycles was ~600 nm, which corresponds to ~200 nm per cycle.

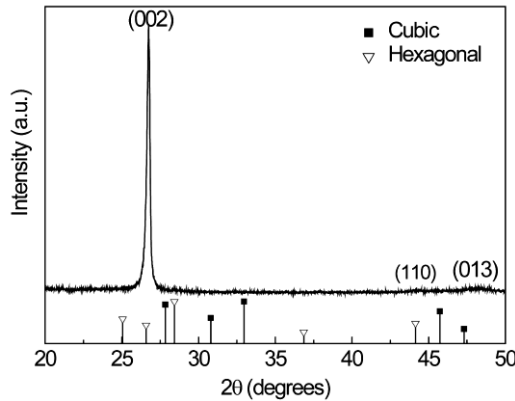


Figure 2-1: Grazing incidence X-ray diffraction pattern of an as-deposited CdS film on a FTO substrate.

2.3.2 The TiN/CdS contact

To investigate the electrical properties of the TiN/CdS contact, circular TiN and Au contacts with diameters of 2 and 1 mm, respectively, were deposited on the CdS film using a mask. The contacts were first deposited in a co-planar manner, as depicted in Figure 2-2 (a) and (b), to prevent short-circuiting through pin-holes in the CdS film. The *J-V* curves of the Au/CdS/TiN system (Figure 2-2(c)) reveal asymmetric diode-like behavior, indicating that one contact is blocking while the other one is Ohmic. Au has an electron work function of 5.3-5.5 eV⁶³ and is well known to form a Schottky contact with CdS.⁹⁸ The *I-V* curve indeed confirms that the CdS/Au Schottky junction is forward biased when a positive potential is applied to the Au contact. The TiN/CdS contact must therefore be Ohmic in nature. This is indeed consistent with the fully Ohmic behavior that is observed when measuring between two TiN contacts, also shown in Figure 2-2(c).

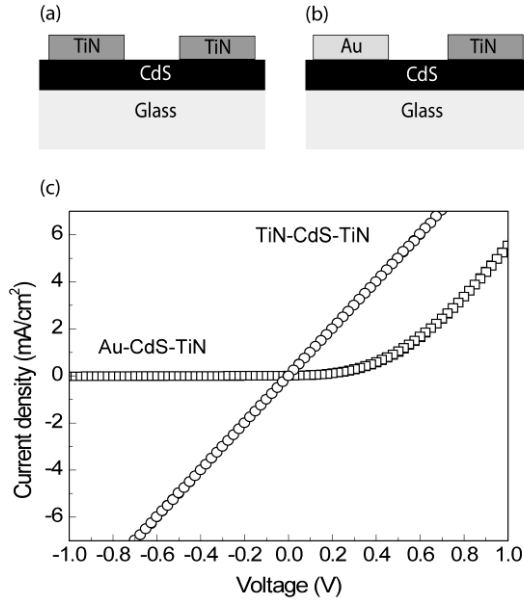


Figure 2-2: Schematic representation of the lateral (co-planar) geometry of the TiN/CdS/TiN (a) and TiN/CdS/Au (b) device structures. (c) J-V curves of the TiN/CdS/TiN (open circles) and the Au/CdS/TiN (open squares) structures.

When TiN is to be used as Ohmic contact material for CdS, both the bulk resistivity of the TiN layer and the contact resistance should be small enough not to cause a large voltage drop and adversely affect device performance. To determine the contact resistance, two-, three- and four-point resistance measurements were carried out using the configuration shown in Figure 2-3(a). The two-point resistance is given by e.g. $R_{12,12} = R_{bulk} + 2R_{contact}$, whereas the three-point resistance is given by $R_{13,12} = R_{bulk} + R_{contact}$. The contribution of $R_{contact}$ is negligible in the case of a four-point measurement. Comparing several sets of two-, three- and four-point resistance measurements therefore allows us to determine $R_{contact}$. Measurements on a rectangular ($2 \times 17 \text{ mm}^2$) section of a 600 nm CdS film with 2 mm TiN contacts yield a value of $R_{contact} = 330 \pm 50 \Omega$. It should be noted that this value also includes contributions from the resistance between the gold pins and the TiN contacts, but separate measurements on a sputtered TiN film show this resistance to be negligible ($\sim 1.1 \Omega$). The spreading resistance can also be neglected for these large contact

areas. After normalizing R_{contact} with respect to surface area, a value of $10 \pm 1.6 \, \Omega \, \text{cm}^2$ is found for the specific contact resistivity between TiN and CdS.

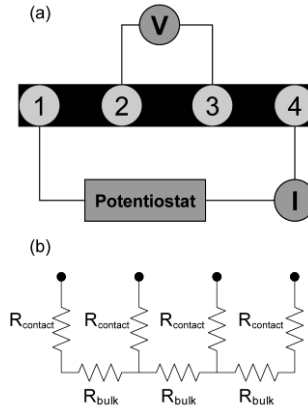


Figure 2-3: (a) Layout of four-point resistance measurements. A current sent through points 1 and 4 gives rise to a potential difference between points 2 and 3, from which the resistance $R_{14,23}$ ($=V_{1,2}/I_{1,4}$) is calculated. The rectangular dark-gray area is isolated from the surrounding material by cuts with a diamond scriber. (b) Equivalent circuit showing the bulk resistance and series resistance components.

This value is several orders of magnitude higher than the contact resistivity reported for other TiN contacts on, for example, GaN and Si devices.⁹⁹⁻¹⁰¹ The high value might be partly due to so-called ‘current crowding’ at the contacts, which means that only part of the TiN contact area is active in the transport of current from and to the CdS. This effect occurs because the diameter of the contact is much larger than the film thickness, and the current always chooses the path of the least resistance.¹⁰² While a detailed quantitative analysis is not possible with the current contact geometry, it is important to realize that the reported value of $10 \pm 1.6 \, \Omega \, \text{cm}^2$ represents an upper limit for R_{contact} due to this effect.

To investigate the stability of the TiN/CdS contact, the sample was exposed to air for a period of 12 months. During this period, the contact resistivity increased by a factor of ~ 3 to $34 \pm 3 \, \Omega \, \text{cm}^2$. The exact origin of the increased resistance is unknown, but the formation of a barrier layer by interdiffusion between TiN and CdS or oxidation of CdS via oxygen transport along grain boundaries perpendicular to the TiN/CdS interface is a likely

cause. Further optimization of the growth conditions may lead to fewer grain boundaries and improved stability in air, but this is beyond the scope of the present study.

2.3.3 Mott-Schottky analysis of the CdS films

Although the data in Figure 2-2(c) as well as the four-point resistance measurements strongly suggest that the TiN/CdS contact is Ohmic, there is a possible alternative explanation for the apparent Ohmic behavior that has to be considered. The exposure of the CdS films to vacuum at high temperatures prior to TiN sputtering, and/or (re-)sputtering of CdS in the initial phase of TiN deposition may have caused a preferential removal of sulfur atoms from the CdS lattice.¹⁰³ These sulfur vacancies act as electron donors and hence increase the concentration of free electrons in the CdS. Using the Kröger-Vink notation, this reaction can be written as follows:



At high sulfur vacancy concentrations, say $>10^{20} \text{ cm}^{-3}$, the concomitantly high donor density results in a very narrow depletion layer. Tunneling of electrons through such a narrow depletion layer would result in apparent Ohmic behavior, even though a Schottky barrier is in fact present.

To investigate this possibility, the donor density of the CdS films has been determined from the space charge capacitance using impedance spectroscopy. Towards this end, Au contacts were evaporated on as-deposited and vacuum-annealed CdS films. As shown previously, these contacts form Schottky barriers and a space charge layer is therefore formed in the CdS region close to the Au contact. FTO layers were used as an Ohmic back-contact,¹⁰⁴ resulting in the parallel plate layout depicted in Figure 2-4 (a) (next page).

Figure 2-4 (c) shows a Nyquist plot of the impedance of a vacuum-annealed FTO/CdS/Au sample. Similar data have been obtained for the as-deposited CdS films (not shown). The relation between the real (Z') and the imaginary part of the impedance (Z'') has the shape of a semicircle. The diameter of the circle depends strongly on the applied bias potential, which shows that the impedance is dominated by the space charge capacitance. The

semicircle is slightly depressed, which indicates small deviations from the ideal capacitive behavior which we attribute to the presence of trap states in the CdS bulk or at the CdS/Au interface. The data can be fitted using an equivalent circuit containing a series resistor (R_1) and a resistor in parallel (R_2) with a constant phase element (CPE), as illustrated in Figure 2-4(b).

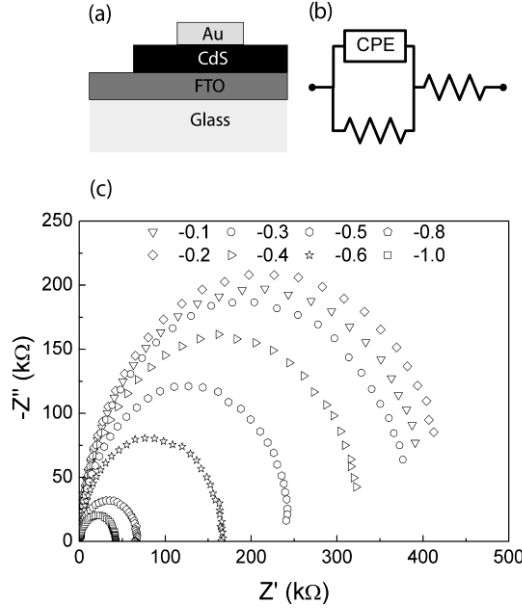


Figure 2-4: (a) Layout of the impedance spectroscopy sample. (b) Equivalent circuit used to fit the impedance data, in which R_1 and R_2 are resistors and CPE is a constant phase element. (c) Nyquist plot of an FTO/CdS/Au sample annealed at 350°C in vacuum. The frequency ranges from 100 kHz to 100 Hz in the clockwise direction.

The complex impedance Z of a constant phase element is given by

$$Z = \frac{1}{Q(j\omega)^n} \quad (2.2)$$

Here, ω is the angular frequency (rad/s), and n is the non-ideality factor of a CPE. For $n = 1$, the CPE is an ideal capacitor with a capacitance $C = Q$, whereas the element is purely resistive for $n = 0$ ($R = Q^{-1}$). For $0 < n < 1$, which is the case for a depressed semicircle, the

equivalent capacitance of the CPE (with the dimensionally correct units of Farads) can be calculated with¹⁰⁵

$$C = Q(\omega_{\max})^{n-1} \quad (2.3)$$

This equation was used to convert the CPE values, obtained from the fitted impedance spectra, to actual space charge capacitance values. The average value of the non-ideality factor obtained from the fit is 0.97 ± 0.01 .

Figure 2-5 shows the calculated space charge capacitances, plotted as $(1/C_{sc})^2$, as a function of the applied bias potential for an as-deposited and a vacuum-annealed CdS sample. From the slope of the line, the donor density N_D of the CdS can be obtained using the Mott-Schottky equation¹⁰⁶

$$\left(\frac{A}{C}\right)^2 = \left(\frac{2}{e\epsilon_0\epsilon_r N_D}\right) \left(V - \varphi_{bi} - \frac{k_B T}{e}\right) \quad (2.4)$$

Here, ϵ_0 is the permittivity of vacuum (8.854×10^{-12} F/m), ϵ_r is the static dielectric constant (8.7 for CdS¹), φ_{bi} is the built-in potential of the junction, V is the applied bias potential, A is the surface area, and all other symbols have their usual meaning. Donor density values of 1.9×10^{16} cm⁻³ and 1.5×10^{17} cm⁻³ are obtained for the as-deposited and vacuum-annealed samples, respectively. The donor density of the as-deposited sample is comparable to the values reported in the literature for CdS films deposited with CBD under similar conditions.^{95, 107, 108} The donor density of the vacuum-annealed sample is an order of magnitude higher due to the loss of sulfur (cf. Eq. (1)). To see if tunneling can play a role under these conditions, the corresponding width w of the depletion layer at an applied bias of 0 V, is calculated using the following expression:¹⁰⁹

$$w = \sqrt{\frac{2\epsilon_0\epsilon_r(\varphi - \frac{k_B T}{e})}{eN_D}} \quad (2.5)$$

For a donor density of 2×10^{17} cm⁻³ and a typical built-in potential of 0.1 – 0.5 V, a

depletion layer width between 20 and 50 nm is found. Clearly, this rules out the possibility of tunneling through the depletion layer. This supports our assertion that TiN forms a true Ohmic contact with CdS.

It should be noted that there is a significant difference in the intercept with the voltage axis for the as-deposited and vacuum-annealed samples. Since the intercept with the voltage-axis is effectively the same as the built-in potential of the Schottky barrier (ϕ_{bi}), this means that the built-in potentials of the Schottky barriers are significantly different. The Schottky barrier height ϕ_{Bn} can be calculated with $\phi_{Bn} = (\phi_{bi} + \xi + k_B T/e)$.¹⁰⁹ The parameter ξ is the difference between the Fermi level and the conduction band in the semiconductor bulk, and is given by¹¹⁰

$$\xi = k_B T \ln \left(\frac{N_c}{N_D} \right) \quad (2.6)$$

In this equation, N_c is the effective density of states in the conduction band:

$$N_c = 2 \left(\frac{2\pi m_e^* k_B T}{h^2} \right)^{\frac{3}{2}} \quad (2.7)$$

Extrapolation of the linear fits in Figure 2-5 yields intercepts of 0.47 ± 0.03 and 0.91 ± 0.01 V. From the measured donor densities and an electron effective mass m_e^* of $0.21 \times m_0$,¹¹⁰ barrier heights of 0.59 ± 0.03 and 0.98 ± 0.01 V are calculated for the as-deposited and vacuum annealed samples, respectively. Both these values are within the range of 0.2-1.02 V reported for Au/CdS Schottky diodes prepared with CBD.^{95, 111, 112} The smaller barrier height of the as-deposited sample is attributed to the presence of a second phase, possibly CdO,¹⁰³ at the Au/CdS interface. This phase forms an insulating layer that accommodates part of the work function difference between CdS and Au. The insulating layer is not present when the CdS is annealed under vacuum prior to depositing the Au contact. This means that the entire work function difference then falls across the space charge layer in the CdS, which explains the larger values for the built-in potential and barrier voltage. The exact nature of the insulating layer is unknown, but it either has a

high enough vapor pressure to evaporate during vacuum annealing, or the vacuum anneal increases its conductivity to a degree that it cannot sustain a significant voltage drop. Due to its negligible vapor pressure at 350 °C,¹¹³ CdO is unlikely to evaporate, but its (n-type) conductivity is indeed likely to increase through oxygen loss during a vacuum anneal at this temperature.

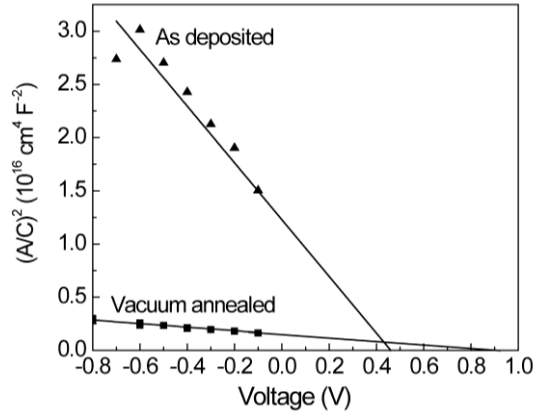


Figure 2-5: Mott-Schottky plot for the Au/CdS junction of an as-deposited and a vacuum-annealed sample, with capacitance values obtained from the fits of the impedance spectra.

The donor density values found above can be used to estimate the degree of non-stoichiometry of the CdS. Here, we assume that sulfur vacancies are the main source of electron donors. The degree of ionization can be calculated with:¹¹⁰

$$\frac{N_D^+}{N_D} = \frac{1}{1 + g_D \exp\left(\frac{E_F - E_D}{k_B T}\right)} \quad (2.8)$$

The donor level E_D of the doubly-ionized sulfur vacancy ($V_S^{\bullet\bullet}$) is located 0.445 eV below the conduction band edge.⁹³ For n-type CdS with an (ionized) donor density of $1.9 \times 10^{16} \text{ cm}^{-3}$, the Fermi level at room temperature is 0.12 eV (cf. Eq. 2.6) below the conduction band, so $(E_F - E_D) = 0.325 \text{ eV}$. The degeneracy factor g_D has the standard value of 2.¹¹⁰ This results in an ionization degree of 0.83% for the as-deposited sample, indicating that the concentration of sulfur vacancies is $1.9 \times 10^{16} / 0.0083 = 2.3 \times 10^{18} \text{ cm}^{-3}$. This corresponds

to approximately 0.01% of the total number of sulfur ions, indicating that these chemical bath-deposited films are highly stoichiometric.¹¹⁴

2.3.4 Au/TiN/CdS diode

Now that a high donor concentration in the CdS can be ruled out as a possible cause for the observed Ohmic nature of the TiN/CdS contact, we turn our attention to the CdS/TiN interface. To investigate the possibility that sputter-induced damage in the CdS is responsible for the Ohmic contact behavior of the TiN/CdS junction, CdS films were deposited on top of the TiN films with CBD. With this configuration the presence of sputter-induced damage in CdS near the TiN/CdS interface can be excluded. Moreover, since TiN is less prone to oxidation than CdS, adverse effects of an oxide interface layer can be minimized. After CBD, the CdS film was annealed at 250 °C in vacuum. The sample was then quickly transferred to the evaporation chamber to minimize oxidation and Au contacts were evaporated onto the CdS film to create a Schottky contact. The structure of this Au/CdS/TiN Schottky diode is given in the inset of Figure 2-6 (next page). The current-voltage behavior of this structure, shown in Figure 2-6, reveals that a non-blocking (Ohmic) contact is again formed at the TiN/CdS junction. This clearly demonstrates that sputter damage does not affect the behavior of the junction, and that it is inherently Ohmic in nature.

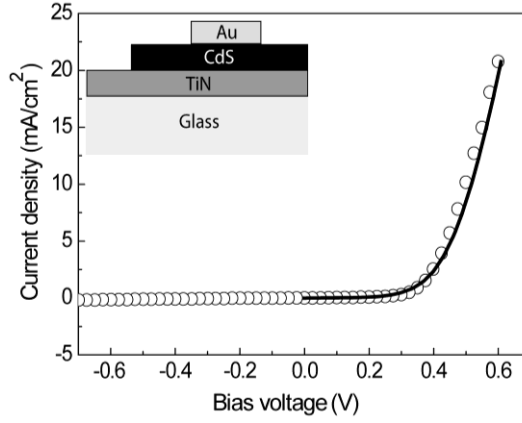


Figure 2-6: IV curve of an Au/CdS/TiN diode, with the Au contact connected as the working electrode of the device. The open squares are the measured values, and the solid line is a best fit of the current to Eq. 2.11. The inset of the graph shows the layout of the sample with parallel contacts.

Even though the I - V curve of the Au/CdS/TiN diode presented in Figure 2-6 shows a clear diode-like behavior, it does not follow the ideal exponential behavior expected for a Schottky diode.¹⁰⁹ At low currents, the curve is approximately exponential, but as the current increases, the behavior starts to become linear. This indicates a resistive component in series with the Au/CdS Schottky junction that causes a voltage drop that is comparable to the diode voltage drop. This means that

$$V = \Delta V_{diode} + \Delta V_{resistor} \quad (2.9)$$

The voltage drop over the diode can be calculated rewriting the standard expressions for the J - V characteristics of a Schottky diode¹⁰⁹ and Ohm's law and rewriting it for forward bias:

$$V = \frac{nk_B T}{e} \ln\left(\frac{J+J_0}{J_0}\right) + JR \quad (2.10)$$

Here, n is the diode's dimensionless non-ideality factor. The saturation current J_0 is given by¹⁰⁹

$$J_0 = A^* T^2 \exp\left(-\frac{e\phi_{Bn}}{k_B T}\right) \quad 2.11$$

The value of the effective Richardson constant A^* is $120 \times (m^*/m_0) \text{ A/cm}^2\text{K}^2$, which yields a value of $23 \text{ A/cm}^2\text{K}^2$ using $m^* = 0.19 \times m_0$ for CdS.^{112, 115}

The barrier height, series resistance and the non-ideality factor have been obtained from the fit of the data. The barrier height is $0.69 \pm 0.01 \text{ V}$, which is in the range of values obtained from the Mott-Schottky measurements. The non-ideality factor is 2.2 ± 0.1 , which is in good accordance with values of Schottky diodes made from nanocrystalline CdS films.^{111, 112, 116} The series resistance obtained from the fit is $149 \pm 18 \Omega$, which represents the sum of the bulk CdS resistance and the contact resistance of the TiN/CdS contact. Because the distance between the Au contact and the TiN back contact is only a few hundred nanometers, the magnitude of the bulk resistance is negligible. This implies that the value of the series resistance is approximately equal to the contact resistance, which leads to a contact resistivity of $4.7 \pm 0.6 \Omega\text{cm}^2$. This is a factor of ~ 2 lower than the upper-limit value determined for the lateral contact configuration.

To summarize the findings, a band diagram of the Au/CdS/TiN Schottky diode is proposed in Figure 2-7.

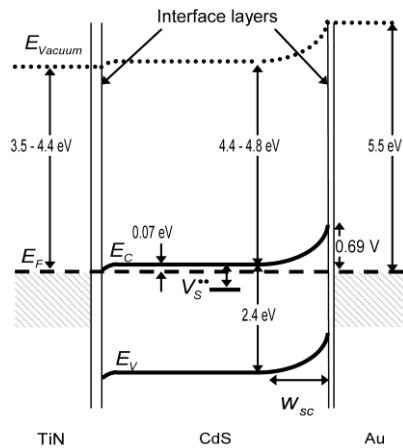


Figure 2-7: Proposed band diagram of the Au/CdS/TiN Schottky diode under equilibrium conditions.

2.4 Conclusions

We have demonstrated that sputtered TiN forms an Ohmic contact with n-type CdS made by chemical bath deposition. This is in accordance with the expectations based on the work functions of both materials. The existence of a semi-Ohmic contact in the form of a narrow Schottky barrier through which electrons can tunnel, could be ruled out explicitly. A value of $4.7 \pm 0.6 \, \Omega\text{cm}^2$ has been found for the contact resistivity of a sputtered TiN contact on n-type CdS. This implies that the Ohmic voltage loss for a standard current density of $10 \, \text{mA/cm}^2$ is less than 50 mV, which is acceptable for most applications. We have demonstrated the feasibility of TiN as an Ohmic contact material for CdS by having fabricated a TiN/CdS/Au Schottky diode. This diode showed an ideality factor of 2.2 and a Schottky barrier height between 0.6 and 1.0 V, depending on the treatment of the CdS prior to depositing the Au Schottky contact.

3 PHOTOCORROSION MECHANISM OF TiO₂-COATED PHOTOANODES*

Atomic layer deposition was used to coat CdS photoanodes with 7 nm thick TiO₂ films to protect them from photocorrosion during photoelectrochemical water splitting. Photoelectrochemical measurements indicate that the TiO₂ coating does not provide full protection against photocorrosion. The degradation of the film initiates from small pinholes and shows oscillatory behavior that can be explained by an Avrami-type model for photocorrosion that is halfway between 2-D and 3-D etching. XPS analysis of corroded films indicates that a thin layer of CdS remains present on the surface of the corroded photoanode that is more resilient towards photo-corrosion.

* This chapter has been published: Arjen Didden, Philipp Hillebrand, Bernard Dam, and Roel van de Krol: Photocorrosion Mechanism of TiO₂-Coated Photoanodes, *International Journal of Photoenergy* (2015) 457980

3.1 Introduction

CdS films have ideal band positions for photoelectrochemical water splitting¹¹⁷ but one of the limiting factors is the severe photocorrosion that the films experience in aqueous media.¹¹⁸ To protect CdS photoanodes from photocorrosion, the surface of the film can be modified with a catalyst that promotes the water splitting reaction, or to add a hole scavenger to the electrolyte. In both cases, the photocorrosion is suppressed through kinetic competition.

An alternative protection mechanism is to deposit a protective coating that creates a physical barrier between electrolyte and the photoactive material.¹¹⁹⁻¹²² Two strategies have been reported in literature. One is to find a hole-conducting material that is stable in electrolyte and has a valence band level that is positioned between that of the photoanode and the oxygen evolution potential of water.¹¹⁹ In this case, the charge carriers can easily transfer from the bulk semiconductor to the coating layer and, subsequently, into the electrolyte. An example of this are the “leaky” TiO₂/Ni films that were recently reported by Hu et al.¹²³ The other strategy is to coat the photoactive material with an extremely thin layer that is thick enough to provide full protection but thin enough to enable tunneling of holes through it.^{120, 121}

In view of its excellent chemical stability, TiO₂ is a promising candidate as an ultrathin protection layer for CdS photoanodes. The band diagram of CdS/TiO₂ system is given in Figure 3-1. Because the TiO₂ valence band edge lies below the CdS level, the layer should be extremely thin in order to let holes tunnel through. Depositing such ultrathin protection layers requires a very high degree of precision and thickness control. Atomic layer deposition (ALD) is a well-suited technique for this purpose, which allows ultrathin layers of a variety of materials to be deposited by employing a sequence of self-limiting adsorption reactions. The self-limiting nature of the reactions gives homogeneous coatings with an excellent thickness control.³³

Even though coating with a protective layer does improve the stability of photoelectrodes, it often does not provide full protection. For example, Cu_2O photocathodes were found to degrade even after more than 10 nm TiO_2 had been deposited with ALD.^{120, 124} Furthermore, corrosion experiments on other types of substrates that were coated with ALD films show that, in spite of the excellent conformal coverage that is normally ascribed to ALD coatings, corrosion still occurs.¹²⁵⁻¹²⁷ In order to improve the effectiveness of the coating, the photocorrosion mechanism has to be understood.

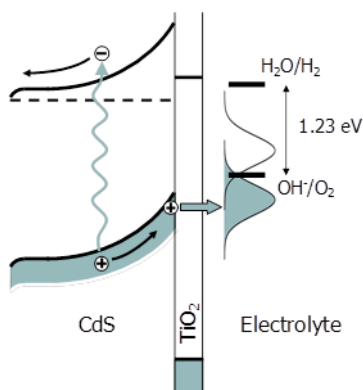


Figure 3-1: Band diagram of a TiO_2 -coated CdS photoanode, illustrating the possibility of hole transfer by tunneling if the TiO_2 film is sufficiently thin. The redox couple's distribution of states in the electrolyte is indicated in this figure as well.

There are several ways to measure corrosion rates, for example by soaking the samples in corrosive liquid for a given time and comparing the properties of coated and uncoated samples.¹²⁶ Yet, most of these techniques only give phenomenological output and do not provide insights into the exact mechanism of (photo-) corrosion. Electrochemical measurements, on the other hand, can give more detailed insights into the corrosion mechanism of coated samples over time. For example, when there is a potential difference between the substrate and the protective coating layer, the degradation of the coating can be followed by measuring changes in the potential or polarization over time.¹²⁸ Also, electrochemical impedance spectroscopy has been used to describe corrosion mechanisms.^{125, 127} In this paper, we explore the photocorrosion mechanism for

an n-type CdS film covered by a thin ALD-deposited TiO₂ protection layer using time-resolved photocurrent measurements. We will show that the behavior can be described with an Avrami-type model that suggests that corrosion mainly takes place in the lateral direction. Moreover, we show that the addition of a hole scavenger cannot fully suppress degradation.

3.2 Experimental

Polycrystalline, ~100 nm thick CdS films were deposited on FTO substrates (fluorine-doped tin dioxide, 15 Ω /sq., TEC 15, Libbey-Owens-Ford) with chemical bath deposition (CBD) according to a method described in section 2.2. Before CBD, the substrates were cleaned by ultrasonic rinsing in acetone and ethanol, followed by a 5 s dip in a dilute HCl solution (17.5 %) and subsequent rinsing with ultrapure de-ionized water (Milli-Q, 18.2 M Ω cm).

After CBD, the samples are rinsed and cleaned ultrasonically in ultrapure water (Milli-Q, 18.2 M Ω cm) to remove loose particulate matter, and subsequently dipped in H₂O₂ and rinsed with ultrapure water. Prior to coating by ALD, the samples were rinsed with ultrapure water and blow-dried with nitrogen. The CdS films were coated with TiO₂ in a home-built ALD reactor. TDMAT (*tetrakis*-dimethylaminotitanium, SAFC electronic grade) and water (Milli-Q) were used as precursors for TiO₂ deposition. TDMAT was used as Ti-precursor instead of the more common precursor TiCl₄ to prevent formation of corrosive HCl as by-product during the ALD reaction. The deposition temperature was 200 °C and the base pressure 1 Pa. All precursors were fed to the reactor by evaporation, without using a carrier gas. To ensure a sufficient vapor pressure, the TDMAT container was heated to 70 °C and the supply lines were heated to 80 °C to prevent condensation. Pulse times used were 3 s and 10 ms for the TDMAT and water respectively. The TiO₂ growth rate, measured on Si wafers with *in-situ* ellipsometry using a Woollam M2000 F spectroscopic ellipsometer, was 1.2 Å/cycle. After deposition, the samples were annealed at 450 °C to form crystalline anatase TiO₂.

Photoelectrochemical measurements were carried out in a three-electrode cell made from Teflon, using an Ag/AgCl reference electrode and a Pt counter electrode. Solutions of KOH (Sigma Aldrich reagent grade, 0.1 M) and Na₂SO₃ (Sigma Aldrich reagent grade, 0.5 M) in water (Milli-Q) served as electrolyte. The potential was applied by a potentiostat (Princeton Applied Research, model EG&G 283), and a class AAA solar simulator (AM1.5, 1000 W/m², Newport Sol3A type 94023-ASR3) was used to illuminate the samples.

X-ray photoelectron spectroscopy (XPS) measurements were carried out with a Specs XR50 X-ray source (Mg K α radiation) and a Phoibos 100 analyzer.

3.3 Results and discussion

Thin TiO₂ layers were deposited on polycrystalline CdS films. The sample geometry is given in Figure 3-2. The polycrystalline CdS films were n-type, with a film thickness of approximately 100 nm. A more detailed description of the CdS films is given in section 2.3.

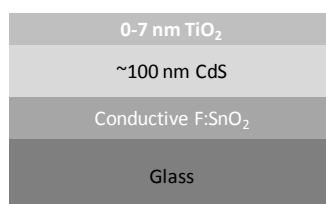


Figure 3-2: Sample structure of the CdS photoanodes coated with thin TiO₂ films.

When we look at the I-V curves of samples coated with 30 and 60 cycles of ALD (Figure 3-3a and 3b) taken in KOH electrolyte in the dark and under simulated solar radiation, the first thing that stands out is that the samples are not stable over several voltage cycles when exposed to light (reference samples without ALD coating degraded too fast for meaningful I-V curves to be recorded). For the sample with 30 ALD cycles we first observe an increase in photocurrent (up to I-V cycle 5) after which the photocurrent decreases again. For the sample with 60 ALD cycles, the highest photocurrent is measured in the first I-V cycle and the photocurrent gradually decreases after each consecutive cycle. Clearly, even after 60 cycles ALD (~7 nm TiO₂ coating), the coating is not thick enough to

provide sufficient protection against photocorrosion. Furthermore, the current density of the sample coated with 60 cycles is about two orders of magnitude smaller than that of the sample coated with 30 cycles. This suggests that the coating layer on top of the CdS film blocks the current. Also for these films, the photocurrent of the coated samples is not stable during cycling.

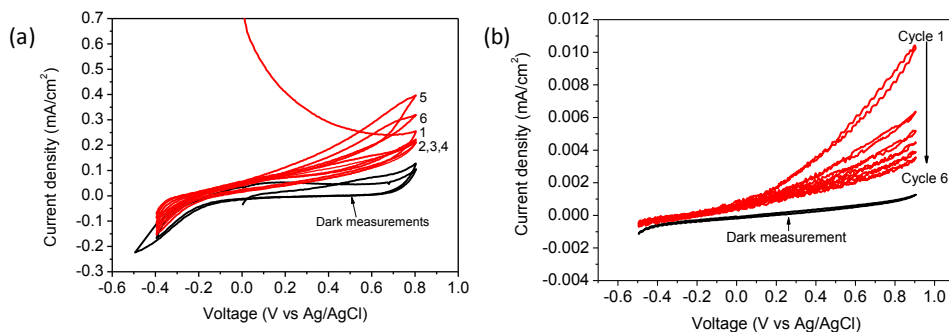


Figure 3-3: I-V curves in 0.1 M KOH solution of CdS films coated with 30 (a) and 60 ALD cycles of TiO₂ (b). Scan rates were 100 mV/s. Red lines represent photocurrent measurements, black lines dark measurements.

To investigate the transient behavior of coated samples, the photocurrent was measured at a fixed potential of 0.5 V vs. Ag/AgCl. Figure 3-4 gives a typical result of the behavior of coated samples over time. After turning on the light at $t = 0$, the current instantaneously rises to a maximum, then decreases, rises again, and finally slowly decays to zero.

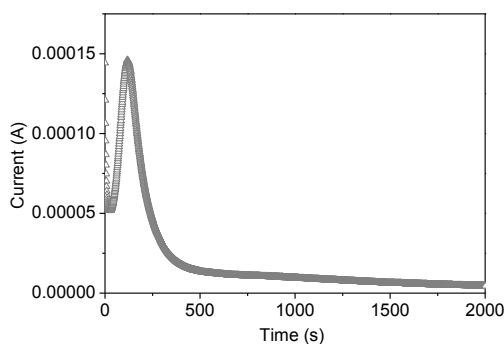


Figure 3-4: Development of current over time in 0.1 M KOH upon illumination of a CdS sample coated with 200 ALD cycles.

The oscillatory behavior of the photocurrent can be modeled by assuming that the photocurrent is the sum of the photocorrosion and water oxidation reactions that occur simultaneously at the photoanode ¹²⁹⁻¹³¹:



Photo-induced water oxidation at semiconductor electrodes has been extensively studied, and to the best of our knowledge has never been reported to give oscillatory behavior. We therefore attribute the photocurrent to photocorrosion of CdS (reaction 3.1). We can explain this behavior by assuming that corrosion is initiated from a number of defects in the coating, as schematically shown in Figure 3-5 (next page). These defects can be microscopic pinholes or cracks caused by incomplete surface coverage, annealing, or lattice mismatch between CdS and TiO₂ (Figure 3-5A). Starting at these defects, the CdS layer is etched away (Figure 3-5B, C). Due to the etching, the etched regions expand (Figure 3-5D), until they converge with other regions (Figure 3-5E). The etching will continue until the entire layer is consumed.

Inspection of partially corroded samples with an optical microscope (Figure 3-6) confirms that corrosion pits are formed in the CdS film. The large corroded areas seem to be made up of smaller, more or less circular corrosion pits that have joined together. This is indeed consistent with the mechanism proposed above.

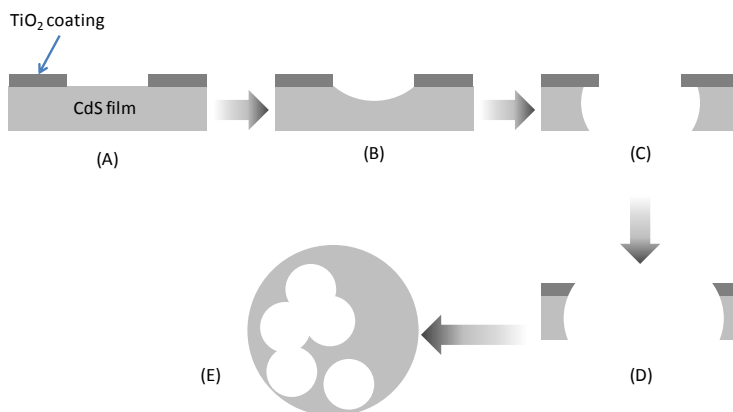


Figure 3-5: Schematic view of the corrosion mechanism where the corrosion starts with the presence of pinhole or crack in the pristine sample (A) at which the corrosion is initiated (B). The corrosion then expands in all directions until the substrate underneath the CdS is reached (C), after which the corrosion pit expands in lateral direction (D) until it merges with one or more neighboring corrosion pits (E).

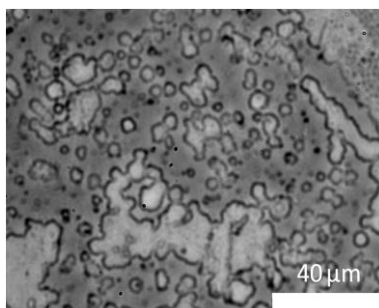


Figure 3-6: Optical micrograph of a CdS film coated with 60 cycles ALD after a photo-electrochemical experiment.

This behavior can be translated to the observed current oscillations by assuming that the photocurrent is caused by corrosion of the film. The two holes required for every molecule of CdS that is etched away (see Eq. 3.1) will contribute to the photocurrent.

The high current immediately after switching on the light, is due to excitation of electron-hole pairs. But since the flux of holes to the surface is larger than the rate at which they

can be consumed by chemical reactions, they accumulate near the surface. As a result, recombination increases, which leads to a decrease of the current. This transient behavior is often observed in photoelectrochemical experiments that use chopped illumination. The decrease in current resembles the discharge of a capacitor over time, where the charge of the capacitor corresponds to the number of accumulated holes. This can be expressed as the recombination current:

$$I_{\text{recomb.}} = I_0 \exp\left(-\frac{t}{\tau}\right) \quad (3.3)$$

In this equation, I_0 is the initial current (A), t is time (s) and τ is the time constant of the decay (s).

Since the area of the pinholes is small and the decay of the photocurrent due to recombination is fast, the contribution of photocorrosion is most likely negligible for the first transient peak at $t < 50$ s in Fig. 4. Assuming that the corrosion reaction only takes place at the edges of the small pin holes, the corrosion rate will gradually increase with the size of the holes as the CdS at the edges dissolves. Larger circumferences of the holes lead to larger reactive surfaces (Figure 3-5C \rightarrow D). The availability of more reactive surface will increase the photocurrent, which marks the start of the second current peak at $t > 50$ s.

This increase in photocurrent will continue until one corrosion pit converges with a second, and perhaps third pit (Figure 3-5E). When two pits meet, the point where they merge will contain no more CdS and, hence, their amount of reactive surface area will decrease. This will slow down the growth of the reactive surface until at some point it will start to decrease. This corresponds to the sharp decrease in photocurrent after the peak. As shown in Figure 4, the current decreases quickly to values below 0.05 mA/cm^2 , after which the photocurrent levels off more gradually towards the end of the experiment.

This photocorrosion model strongly resembles the Avrami model for crystal growth in metals. This model predicts the fraction Φ of material converted into a new phase (in this case: the material etched away) as a function of time t with the equation:¹³²

$$\Phi = 1 - \exp(-kt^n) \quad (3.4)$$

Here, the constant k is the product of a shape factor, the effective number of nuclei, and the direction-averaged growth rate. The exponent n is the sum of the dimension of the crystal growth process (1 for needle-like, 2 for plate-like, and 3 for 3-D growth) and an integer value describing the nucleation rate (1 for constant nucleation rate, 0 for the absence of nucleation). In this model we assume that the corrosion rate in the lateral direction is constant. Furthermore, since the size of the pin holes is several orders of magnitude larger than the film thickness (micrometers vs. tens of nanometers, see Figure 3-6), etching will mostly take place in the lateral direction and the process will most likely be 2-dimensional.

If we assume that O_2 production at the photo-anode is negligible, the fraction of material that has been corroded can be described by integrating the corrosion current I_{corr}

$$\Phi = \frac{1}{dA\rho_M N_A q} \int_0^t \frac{1}{\eta} I_{corr} dt \quad (3.5)$$

In this equation, d is the thickness of the film (in m), A the total surface area of the electrode ($2.82 \times 10^{-5} \text{ m}^2$), ρ_M the molar density (mol/m^3), N_A Avogadro's number, q the elementary charge (C) and η the number of electrons consumed per reaction(-). Combining equation (4) and (5) and integration yields

$$I_{corr} = \alpha n k t^{n-1} (\exp(-kt^n)) \quad (3.6)$$

With

$$\alpha \equiv dA\rho_M q \eta \quad (3.7)$$

The total current can be expressed as the sum of the recombination current, $I_{recomb.}$, the corrosion current, I_{corr} , and a linear equation ($at + b$) that is used to fit the sloping part of the curve that is visible at the second half of the curve:

$$I = \alpha n k t^{n-1} (\exp(-k t^n)) + I_0 \exp\left(-\frac{t}{\tau}\right) + at + b \quad (3.8)$$

The fit parameters are α , n , k , τ , a , and b .

The equation was used to fit the experimental data given in Figure 3-4, which shows the photocurrent transient of a CdS sample coated with 200 cycles ALD in 0.1 M KOH. Figure 3-7 shows the best possible fit to the data.

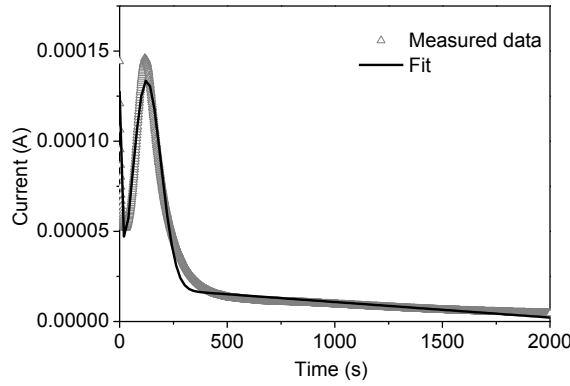


Figure 3-7: Photocurrent transient after turning on the light at $t=0$ (grey triangles) and a fit of the data with the equation (8) (black line).

The fit results in a value of $3.6 \times 10^{-6} \text{ s}^{-n}$ for k and, more importantly, an exponent n equal to 2.5. Assuming that no additional pinholes or other corrosion nuclei are formed during the corrosion process (which means that all nuclei are imperfections in the TiO_2 coating and that no other nuclei are formed), the part of the exponent that is related to the nucleation rate can be assumed to be 0. The corrosion is then partly plate-like (2-dimensional) and partly in three dimensions, which means that the layer dissolves in the lateral direction starting from the initially present pinholes.

The value for α is equal to 17.5 mC. From this, the film thickness d can be calculated with Eq. 5. With a CdS molar density of 33.4 kmol/m^3 , a surface area of $2.82 \times 10^{-5} \text{ m}^2$ and the

standard values of N_A and q ($6.02 \times 10^{23} \text{ mol}^{-1}$ and $1.6 \times 10^{-19} \text{ C}$ respectively), the calculated value for the thickness d is equal to 96.6 nm, which indeed matches well with the measured film thickness of approximately 100 nm. This confirms our initial assumption that the photocurrent can be entirely attributed to photocorrosion, with negligible contribution from water oxidation.

In contrast to what the model predicts, the photocurrent does not go entirely to zero after the main current peak ($t > 500 \text{ s}$), but instead shows a linear decrease. This suggests that part of the photoactive layer remains on the FTO substrate and corrodes much slower than the rest of the CdS layer. Alternatively, part of the linearly-decreasing photocurrent may be due to water oxidation at the exposed FTO surface.

To investigate this, the composition of the surface of a corroded sample has been analyzed with XPS and compared to that of the as-deposited samples (with 60 and 200 cycles ALD, Figure 3-8). The as-deposited samples reveal a small but clear Ti signal. In contrast, no Ti signal can be observed for the fully etched sample (Fig. 6, bottom curve). This confirms that the TiO_2 coating is completely removed during etching. Surprisingly, however, the fully corroded sample shows no Sn signal that would indicate the presence of the underlying FTO film. This indicates that at least a few nm of CdS remain on the surface, and that little or no FTO is exposed to the electrolyte. The thin CdS layer apparently is able to generate a persistent photocurrent after 500 s. This suggests that the CdS layers initially grown on the FTO are more resilient to etching. The reason for this is unknown and calls for further investigation.

Interestingly, the spectra of the as-deposited samples with both 60 and 200 ALD- TiO_2 cycles still show strong Cd and S peaks. The penetration depth of XPS is typically $< 5 \text{ nm}$, which means that both Cd and S are present within the uppermost 5 nm of the sample. Because the deposited film is much thicker than 5 nm (7 and 24 nm for 60 and 200 cycles respectively) this means that either Cd has diffused through the TiO_2 during the thermal anneal or that the TiO_2 coating is not homogeneous.

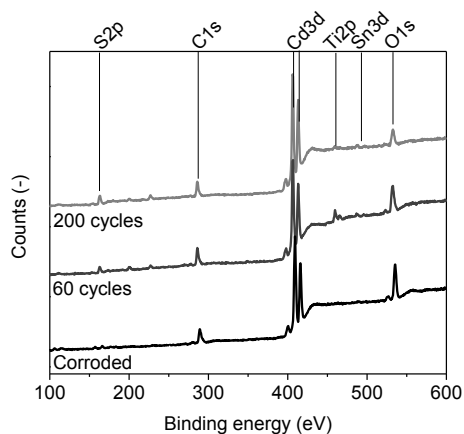


Figure 3-8: XPS spectra of a fully corroded sample that was originally coated with 200 cycles ALD (1) and as-deposited samples with 60 (2) and 200 (3) cycles ALD. The vertical lines indicate the most prominent element peaks. The spectra are offset for clarity.

Extensive diffusion of Cd through TiO_2 is unlikely. No data on diffusion rate is available in literature, but based on the much larger ionic radius of Cd^{2+} compared to that of Ti^{4+} (95 vs. 61 pm, respectively¹³³), it is reasonable to assume that Cd diffusion through solid TiO_2 is very slow. The fact that we nevertheless observe a Cd signal suggests that the TiO_2 layer does not fully cover the CdS. The presence of uncovered CdS, possibly in the form of pin holes, is indeed consistent with the photocorrosion that we observed and described above.

The molar fractions calculated from the XPS data (given in Table 3-1) indicate that the concentration of O atoms at the surface is more than 2 times higher than the concentration of Ti, whereas the concentration of S is lower than that of Cd. This strongly suggests that other components, such as CdSO_4 , CdS_2O_3 , CdO or $\text{Cd}(\text{OH})_2$ are present at the surface due to partial oxidation or hydroxylation of the CdS. Furthermore, the broadness of the C1s peak, with contributions at above 287 eV, indicates that carbon impurities are present in the form of carbonates.

Table 3-1: The table gives the atomic composition of the samples. The numbers between brackets indicate surface area of the corresponding peaks.

	<i>As-deposited 60 c. ALD</i>	<i>As-deposited 200 c. ALD</i>	<i>Corroded 200 c. ALD</i>
C	43.4 (35561)	41.2 (401013)	36.8 (7670)
Cd	20.7 (316291)	15.5 (282556)	16.9 (65913)
O	22.1 (44489)	31.8 (76043)	42.1 (21520)
S	11.8 (17316)	6.7 (11669)	4.2 (1556)
Ti	2.1 (11962)	4.8 (32798)	0.0 (0)
Sn	0.0 (0)	0.0 (0)	0.0 (0)

An alternative protection strategy is to use an electrolyte that reacts with the holes on a time scale that is much faster than the CdS oxidation reaction. This would kinetically stabilize the photoanode. Na₂SO₃ was used as such a ‘hole scavenger’ because the oxidation of sulfite to sulfate is a two-electron redox reaction which is known to be much faster than the four-electron water oxidation reaction.¹³⁴

The effect of using Na₂SO₃ electrolyte rather than KOH becomes clear when comparing the IV curves in Figure 3-9 with the IV curves of a sample in KOH given in Figure 3-3. The sample in KOH shows instability of the photocurrent upon cycling, whereas the sample in Na₂SO₃ shows little or no decay after cycling.

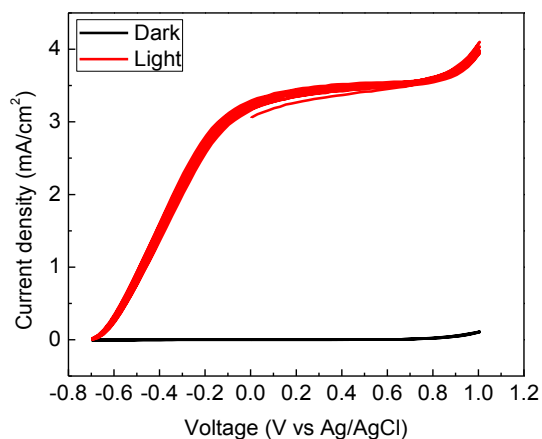


Figure 3-9: IV curves of uncoated CdS in Na_2SO_3 in dark conditions and under solar radiation, measured at scan rates of 100 mV/s.

Even though the Na_2SO_3 stabilizes the sample during the IV measurements, long term experiments (>40 minutes) show that even with a hole-scavenger present the photocurrent decreases over time. This is clearly visible in Figure 3-10, where the current under chopped illumination over time is given of a CdS sample in Na_2SO_3 electrolyte (The insert shows the photocurrent over a 1 minute time span).

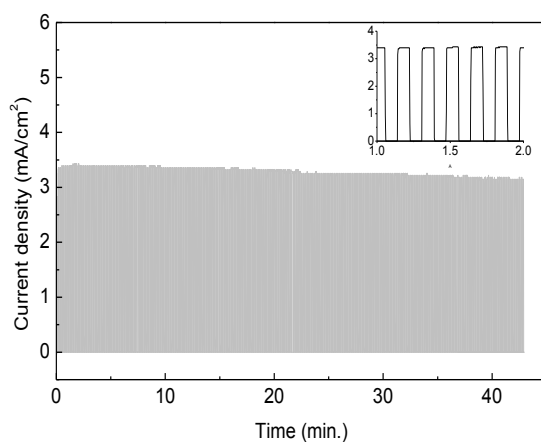


Figure 3-10: Current in time for an uncoated CdS sample in Na_2SO_3 electrolyte at 0.5 V vs. Ag/AgCl.

Assuming that the absorption of incident light by the CdS is linearly dependent on the layer thickness, the corrosion rate can be estimated from the time-dependent decrease of photocurrent and the dependence of the photocurrent on the amount of absorbed light. The decay in photocurrent is approximately $0.12 \text{ } (\mu\text{A}/\text{cm}^2)/\text{s}$. Assuming that an initial film thickness of $\sim 100 \text{ nm}$ gives a photocurrent of $3.2 \text{ mA}/\text{cm}^2$ (Figure 3-9), the decay in photocurrent corresponds to a dissolution rate of approximately $12.5 \text{ pmol}/\text{cm}^2/\text{s}$, or $4 \text{ pm}/\text{s}$. The sulfite oxidation rate at $t = 0$, assuming that all photocurrent is used for sulfite oxidation, is $36 \text{ nmol}/\text{cm}^2/\text{s}$. Two assumptions have to be made for the estimated rates to be valid: a) the change in Na_2SO_3 concentration at the sample surface is negligible and b) the efficiency of light absorption, charge separation, and charge transfer to the electrolyte remains constant. The reduction of sulfite concentration, calculated by integrating the photocurrent over time and subtracting this from the initial concentration is $<1\%$, which is indeed negligible. As the anode material does not change but merely dissolves slowly over time, the second assumption is also likely to hold. Hence, we conclude that the sulfite oxidation rate is ~ 3 orders of magnitude faster than the photocorrosion rate. This is clearly insufficient to guarantee long-term stability of the CdS photoanode.

3.4 Conclusions

Although films deposited with ALD are supposed to be highly conformal, we find that thin ALD- TiO_2 films are not able to protect CdS films against photocorrosion in aqueous KOH solutions. The corrosion starts from pinholes in the TiO_2 protection layer where the CdS is in direct contact with the electrolyte. The observed photocurrents are mainly due to corrosion, as opposed to water oxidation. The photocurrent shows a well-defined and reproducible oscillation peak that can be fitted with an Avrami-type model that suggests a partly lateral (2-D), partly 3-D photocorrosion mechanism of the CdS film.

XPS analysis of the samples confirms that the samples are indeed not completely coated with TiO_2 , and that a mixture of CdS and partially oxidized or hydroxylated phases (e.g. $\text{Cd}(\text{OH})_2$) are present at the surface. The XPS analysis also revealed that a thin layer of CdS

remains present at the surface, even after prolonged exposure to light. The reason for the high photochemical stability of the bottom part of the CdS layer is not fully understood.

Using Na_2SO_3 as a hole scavenger greatly improves the stability of the CdS films. It does not, however, completely solve the photocorrosion problems of CdS. In the end, having a protective layer that a) can conduct holes, b) is stable in aqueous solutions, and c) is completely free of pinholes will provide a more lasting protection.

4 FLUIDIZED-BED ATOMIC LAYER DEPOSITION REACTOR FOR THE SYNTHESIS OF CORE-SHELL NANOPARTICLES*

The design of a fluidized bed atomic layer deposition reactor is described in detail. The reactor consists of three parts that have all been placed in one protective cabinet: precursor dosing, reactor and residual gas treatment section. In the precursor dosing section, the chemicals needed for the ALD reaction are injected into the carrier gas using different methods for different precursors. The reactor section is designed in such a way that a homogeneous fluidized bed can be obtained with a constant, actively controlled, reactor pressure. Furthermore, no filters are required inside the reactor chamber, minimizing the risk of pressure increase due to fouling. The residual gas treatment section consists of a decomposition furnace to remove residual precursor and a particle filter and is installed to protect the pump. In order to demonstrate the performance of the reactor, SiO₂ particles have been coated with TiO₂ using TDMAT and H₂O as precursors. Experiments with varying pulse times show that saturated growth can be obtained with TDMAT pulse times larger than 600 s. Analysis of the powder with HAADF-STEM and EDX confirmed that after 50 cycles, all SiO₂ particles were coated with a 1.6 nm homogenous shell of TiO₂.

* This chapter has been published as: Arjen P. Didden, Joost Middelkoop, Diana E. Nanu, Wim F.A. Besling, and Roel van de Krol: Fluidized-Bed Atomic Layer Deposition Reactor for the Synthesis of Core-Shell Nanoparticles, *Review of Scientific Instruments* **85** (2014) 013905

4.1 Introduction

In this chapter the design of the Fluidized Bed Atomic Layer Deposition reactor (FB-ALD reactor) is described in detail. In a FB-ALD reactor, first developed by Wank et al.,³⁰ nanoparticles are coated in a fluidized bed reactor with the thickness control of Atomic Layer Deposition (ALD). Because ALD can be used for the deposition of a wide range of materials, various types of nanoparticles have been coated with a range of oxide and nitride coatings.^{30, 135-143}

One of the limitations of previously reported FB-ALD designs is the use of a metal tube as the reactor vessel. Visual inspection of the reactor bed, which provides valuable information on the behavior of the particles (e.g. to see the occurrence of bubbling or slugging in the fluidized bed), is not possible with these designs. Furthermore, the placement of particle filters inside the reactor itself makes them susceptible to fouling, which can lead to increased reactor pressure and, hence, a reduced superficial gas velocity that can cause a collapse of the fluidized bed.

In this chapter, we describe a reactor design that solves the aforementioned issues. The reactor section consists of a glass tube that is heated with lamp heating (as was also used by Beetstra et al.¹⁴⁴) or, if needed, with heating tape, providing the possibility of visual inspection as well as more flexibility in reactor chamber design. The reactor chamber design also includes an expansion section that is used to reduce loss of particles due to entrainment without having to use filters. To reduce particle losses even more, the reactor chamber is evacuated via a soft-start valve. The reactor also has an active pressure control loop that makes sure the pressure in the reactor is constant throughout the process and enables a more stable fluidization and deposition process. The gas supply system, vacuum pumps, exhaust treatment and the reactor itself are all integrated in a closed cabinet that isolates the reactor from its environment, making it suitable to be placed safely in any laboratory.

The capabilities of the reactor are demonstrated by coating SiO_2 nanopowder with thin TiO_2 layers. This has been achieved with a low-temperature ALD process using *tetrakis*-titanium (TDMAT) and H_2O as precursors,^{44, 145} which is a new deposition chemistry for FB-ALD. The self-limiting nature of the film growth has been verified using chemical analysis of the powder. The core-shell structure of the particles as well as the growth per ALD cycle has been recorded using Transmission Electron Microscopy (TEM).

4.2 Apparatus description

The FB-ALD process can be divided into three different sections. In the first part, the carrier gas is mixed with the ALD precursors. The second part is the reactor in which the actual coating process takes place. The third part is the downstream section in which the leftover chemicals are thermally decomposed and entrained particles are removed from the stream. The process flow diagram of the FB-ALD, depicting the three sections of the process, is given in Figure 4-1. All three process sections as well as the process control and safety aspects will be described separately.

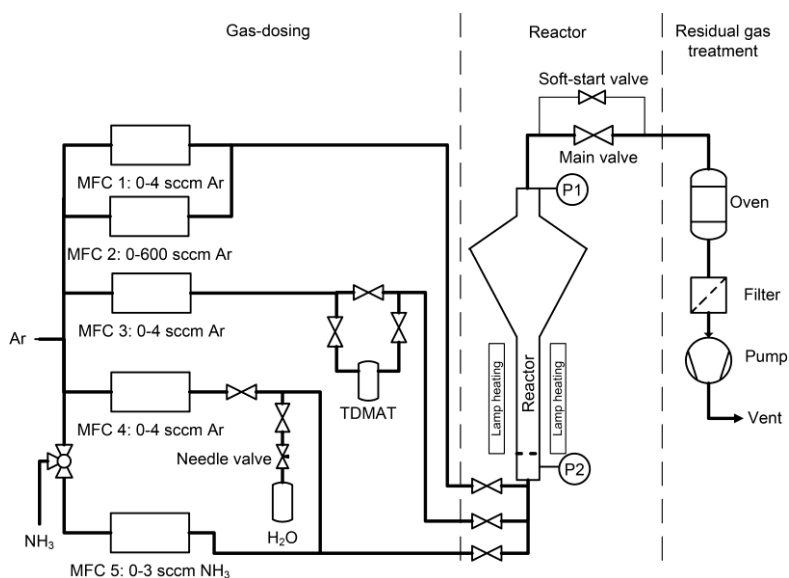


Figure 4-1: Process flow diagram of the fluidized-bed ALD reactor.

4.2.1 Precursor dosing

The precursor dosing section is made of 1/8" stainless steel tubes that follow the process flow diagram presented in Figure 1. In order to prevent precursor condensation, all tubes are heated to 90 °C by trace heating. All automatic valves are Swagelok high temperature ALD valves. Three MFCs (Brooks SLA 5850S mass flow controller) with a range of 0-4 sccm (standard cubic centimeter per minute, 7.45×10^{-7} mol/s) supply the Ar (argon 5.0, Linde gas) that is used as fluidization gas, carrier gas, and purge gas. Typical linear gas flow velocities needed to fluidize nanoparticle agglomerates at low pressures are 0.2 – 8 cm/s,^{73, 146, 147} which corresponds to 0.1– 2 sccm for an operating pressure of 1 mbar and a reactor diameter of 2 cm. A MFC with a larger flow rate (600 sccm) is installed to allow removal of the nanoparticles from the reactor by purging with inert gas.

The ALD precursor vapors are added to the Ar flow using three different methods. For liquid precursors with a low vapor pressure (such as TDMAT, which has a vapor pressure of 3.4 mbar at 75 °C), argon is bubbled through the liquid phase to become saturated with precursor. For more volatile liquids, (such as water, with a vapor pressure of 30 mbar at 25 °C), the vapor pressure is sufficiently high to extract the vapor from the liquid container without inert gas bubbling. Gaseous precursors (e.g. ammonia) are administered via a separate MFC with special NH₃-compatible seals.

To maintain a stable fluidized bed, the gas flow should remain within a certain range. Too low gas flows make the bed collapse; too high flows cause entrainment of the particles and subsequent loss of particles via the exhaust. During the precursor pulse, the MFCs are kept at their steady setpoint. This means that the total gas flow that goes through the reactor increases during the pulses. For precursors with a low vapor pressure (TDMAT), the increase in flow is too small to have any effect on the bed. For precursors with a high vapor pressure (H₂O), the vapor flow easily becomes too high to maintain a fluidized bed and particles will be entrained. To quench the flow and thus minimize particle loss from the reactor, a needle valve has been installed at the exit of the water precursor vessel (cf. Figure 4-1).

4.2.2 Reactor

The core of the reactor system is a 30 cm long glass tube with an inner diameter of 2 cm and a wall thickness of 2 mm. To prevent the particles from getting entrained by the gas flow, the upper part of the tube expands to a diameter of 10 cm (Figure 4-2). The expansion has an angle of 25° with respect to the axis of the tube. The gas velocity decreases 25 times in this part of the reactor, which is an efficient method to prevent most of the particles and particle agglomerates from being carried away to the exhaust. The total length of the reactor tube is approximately 50 cm.

Because nanoparticles usually show strong adhesive Van der Waals forces, they are often difficult to fluidize. These forces can be overcome by vibration of the particle bed, which strongly improves the fluidization behavior.^{69, 146, 148-150} A pneumatic piston vibrator (LöPre Vibrator Type VP 2) is installed to agitate the entire reactor system. The frequency of vibration is 90 Hz, and the total vibration force that can be generated is 150 N. The benefit of using this pneumatic, linear vibrator is that it is more compact than the vibrating table used in previous works making it easier to build it into the reactor cabinet. To isolate the vibrating part from the rest of the setup, the reactor is mounted in a pivoting rack that rests on two rubber feet (Figure 4-2, part 9). Flexible, stainless steel bellows tubes are used to connect the reactor to the gas dosing system, pressure gauges, and the residual gas treatment section.

In order to obtain a homogeneous fluidized bed, the fluidization gas needs to be distributed homogeneously. To achieve this, the gas stream is injected into a small chamber, a so-called “wind box”, via a nozzle with six radial distributed holes. By distributing the gas in a radial direction, a homogeneous upward gas flow is obtained. The gas then travels through the distribution plate. This sintered metal plate (Bekaert Bekipor ST type 5 AL3 S), is placed in the reactor to prevent the particles from falling into the windbox and to further homogenize the gas flow. This is essential in order to obtain high-quality homogeneous coatings. An O-ring made from nitrile butadiene rubber (NBR) is

used to ensure a gas-tight seal between the distribution plate and the reactor tube. An exploded view of the distribution plate assembly is shown in Figure 4-2.

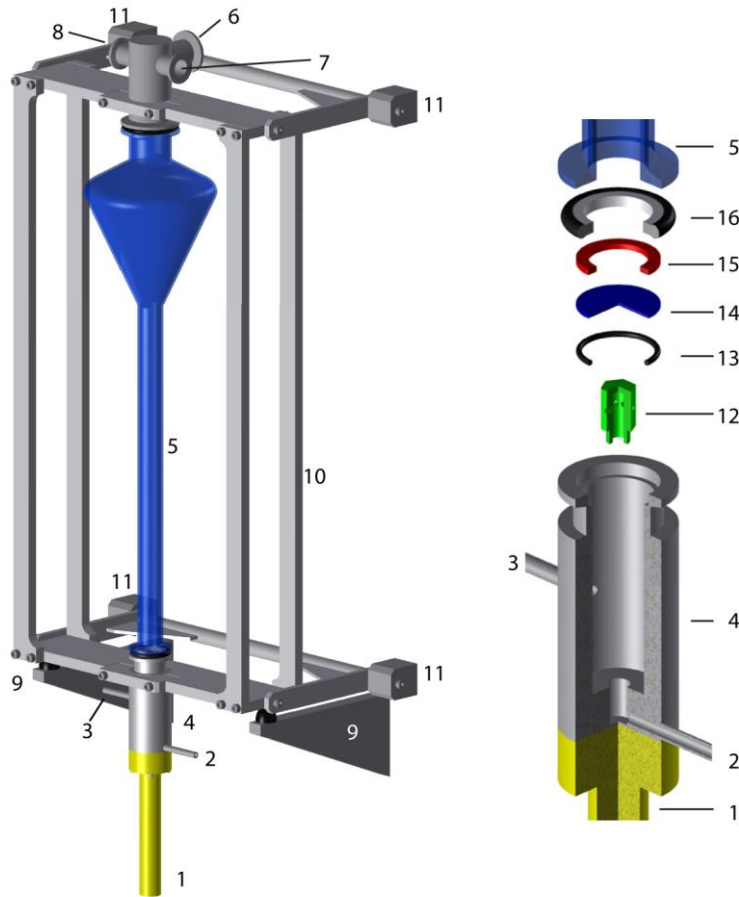


Figure 4-2: Assembly drawing the reactor section and an exploded three quarter section view of the windbox assembly with the vibrator (1), the gas inlet (2), the pressure gauge connection (3), the windbox (4), the reactor tube (5), the gas exit (6), pressure gauge connection (7), soft start gas exit (8), support with rubber feet (9), pivoting rack (10), wall mounting of pivoting rack (11), gas injection nozzle with 6 holes (12), O-ring seal (13), distributer plate (14), washer ring (15), and KF25 seal (16).

The reactor is operated at absolute pressures between 0.5 and 1 mbar. The low pressure is obtained by a lubricant- and particulate-free dry roughing pump (ADIXEN ACP 15G) with a variable rotation speed that can be used to obtain pressures ranging from several millibars down to 10^{-2} mbar. The reactor and vacuum pump are connected via a 1" stainless steel flexible bellows tube with KF25 flanges and a KF25 gate valve. The gate valve is bypassed with a small all-metal manual valve connected via 1/8" stainless steel tubing. This bypass is used to soft-start the initial evacuation of the system in order to prevent the particles from being blown out of the reactor.

The reactor section can be heated by trace heating or by four halogen heater lamps (Phillips halogen lamps, 30 cm long, 1000 W each). The lamps are vertically suspended in such a way that the reactor tube remains visible from the outside, thus allowing for visual inspection or in-situ measurements.

4.2.3 Residual gas treatment

The gas coming out of the reactor can contain relatively large quantities of particles and corrosive chemicals. To avoid pollution and damage to the vacuum pump, the gas needs to be cleaned first. Towards this end, the gas is led through a tube furnace operated at a temperature well above the decomposition temperature of the precursor (200 °C in the case of TDMAT^{46, 151, 152}). After the gas has gone through the furnace, the particles are removed by a custom-made filter that has been specifically designed to have both a small pressure drop and good filtration efficiency. We found that without such a filter the lifetime of the pump was limited to a few months instead of years. The filter, shown in Figure 4-3, consists of a cylindrical vessel with a diameter of 30 cm and a height of 50 cm. The gas is fed tangentially into the bottom of the vessel. Because of the large diameter, the gas velocity is more than 200 times lower than in the reactor. A substantial fraction of the particle agglomerates that were entrained in the gas flow at the exit of the reactor will settle at the bottom of the vessel. Any remaining (smaller) agglomerates are captured by the filter cartridge, which is filled with steel wool and placed at the exit at the top of the vessel.

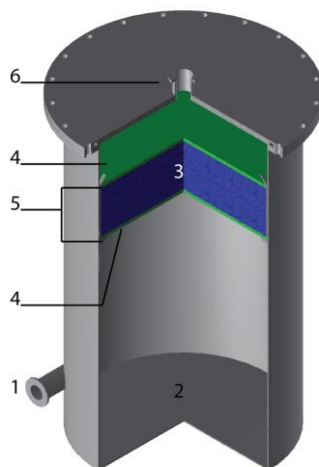


Figure 4-3: Three quarter section view of the particle filter, with gas inlet (1), settling zone (2), filter material, e.g. steel wool (3), sieve plates (4), filter cartridge (5) and gas outlet (6).

4.2.4 Process control

The pressure in the reactor is coarsely regulated by the pump's rotational speed. However, because the pump speed can only be controlled in discrete steps, and the pressure obtained in the reactor also depends on parameters such as temperature and gas flow, further control of pressure is needed. This is done by first setting the rotation speed of the pump to obtain a pressure that is slightly below the desired pressure. The pressure is then regulated to the desired value by admitting N_2 gas into the gas purge of the pump via a PID-controlled MFC (Bronkhorst). A higher purge gas flow results in a higher pressure. The pressure at the top-end of the reactor (P1 in Figure 1) is used as the process value since it is less sensitive to gas flow variations during the precursor pulses than the pressure below the distribution plate (P2). A scheme of the process control loop is given in Figure 4-4.

The heating of the reactor tubes, precursor vessels and reactor itself is controlled by a Eurotherm Mini-8 system. To prevent condensation, the tubing is always kept at a temperature that is at least 10 °C higher than the bubbler temperature.

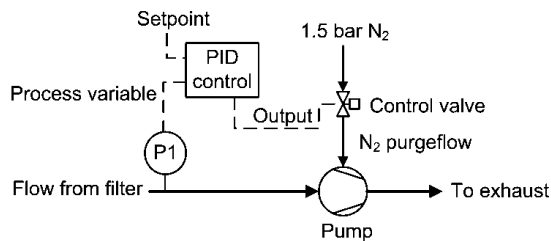


Figure 4-4: Pressure control scheme. Solid lines are gas flows, dashed lines are (electrical) control signals.

4.2.5 Safety

Processing nanoparticles and highly reactive precursors in a glass reactor tube does pose certain safety issues. To minimize the risks and consequences of failure, several safety precautions have been taken. The complete system has been built in a closed cabinet, with separate compartments for the three reactor sections depicted in Figure 1. A fourth (separate) compartment houses all the electronics. The reactor and residual gas treatment compartments both have openings at the top above which fume extraction arms are positioned. This greatly reduces the chances of particles becoming airborne and released into the lab should the glass reactor tube fail. Another advantage of the enclosures is that they greatly reduce the noise levels due to the vacuum pump and the pneumatic vibrator.

One possible failure mechanism is the clogging of the distribution plate or the particle filter by nanoparticles or condensed precursor liquid. This can lead to pressure build-up and eventually reactor failure. Since clogging by nanoparticles is difficult to prevent entirely, the software automatically shuts down the complete reactor system if the pressure exceeds a predetermined set-point.

To minimize the chance of leakage, Swagelok VCR connections have been used for all gas connections between the precursor bubblers and the reactor. Amine-resistant Buna-N O-ring seals have been used for the reactor and the gas treatment sections. Two exceptions

are the O-ring seals of the decomposition furnace. At these positions, Kalrez O-rings have been used since they have the required temperature tolerance.

4.2.6 Precursor selection

The selection of appropriate precursors for the FB-ALD is based on different criteria than conventional ALD. The reasons for this are found in the large surface area of the powder and the relatively high reactor pressure required for the fluidization of particles. Because the surface area of nanopowders can be in the order hundreds of square meters, the amount of precursor that is needed for monolayer coverage is relatively large compared to conventional ALD process. This imposes more strict requirements on the amount of precursor that can be introduced in the reactor, and requires careful consideration of the much larger amounts of undesired by-products that may be formed.

The TDMAT process was chosen for this work instead of the more commonly used TiCl_4 - and TTIP-processes. In the TiCl_4 -process, corrosive HCl is formed as a by-product and, because of the large amounts produced in the FB-ALD reactor, this precursor could not be used. The decision between TDMAT and TTIP was based on the vapor pressure of the two precursors. TTIP has a much lower vapor pressure and, hence, evaporation rate than TDMAT (in the maximum allowable temperature window of the precursor dosing system). A lower evaporation rate causes a longer required pulse time.

4.3 Experimental Verification

To demonstrate the performance of the FB-ALD reactor, SiO_2 nanoparticles were coated with thin TiO_2 shells using tetrakis-dimethylamino titanium (TDMAT, SAFC Hightech®, electronic grade) and H_2O (ultrapure, Milli-Q). The SiO_2 nanoparticles (Aerosil 90, ~90 m^2/g , Evonik) were first sieved through a 500 μm mesh to remove the largest agglomerates. Approximately 0.5 gram of the sieved powder was fed into the reactor. Before deposition, the particles were dried under vacuum (1 mbar, 100 °C) under a small Ar gas flow (0.2 sccm) for at least 6 hours.

After drying, the particles were brought into the fluidized state by increasing the flow of Ar. The minimum fluidization velocity, at a pressure of 1 mbar and with the aid of vibration, is approximately 1.5 sccm (determined from Figure 4-5). This corresponds to an average gas velocity of 8 cm/s in the reactor.

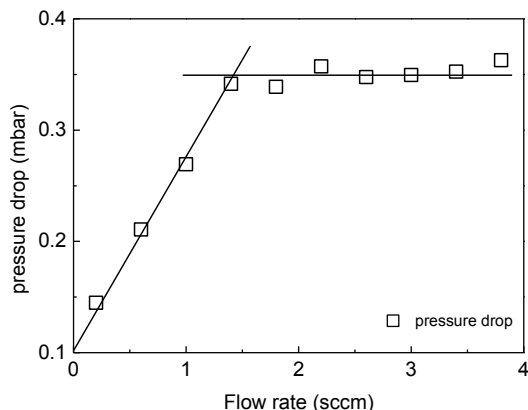


Figure 4-5 Pressure drop as a function of the Ar flow. The crossing point of the lines indicates the minimum fluidization velocity

The total surface area of the nanopowder ($\sim 50 \text{ m}^2$ for 0.5 g) is 2 – 3 orders of magnitude larger than the typical surface areas that need to be covered in conventional ALD reactors (e.g. $\sim 0.07 \text{ m}^2$ for a 300 mm Si wafer). Assuming a surface coverage of $\sim 2 \times 10^{18}$ molecules of TDMAT per m^2 (based on a kinetic molecule diameter of 7 \AA),⁴⁹ approximately 0.15 mmol of TDMAT is needed per ALD cycle. This large amount of precursor already suggests that long pulse times are required to coat nanopowders. To estimate the required pulse times, the flow of TDMAT needs to be known. The amount of vapor that is extracted from a bubble vessel can be estimated by assuming the bubbles are fully saturated with the precursor vapor:¹⁵³

$$F_p = F_{cg} \frac{p_{vap}}{p_{total}} \quad (4.1)$$

Here, F_p is the flow of precursor (mol/s), F_{cg} is the flow of carrier gas (mol/s), and p_{total} the

total pressure in the bubbler (mbar). The vapour pressure p_{vap} (mbar) of TDMAT can be estimated with the expression¹⁵⁴

$$p_{vap} = 1.33 \times 10^{\left(8 - \frac{2850}{T+273}\right)} \quad (4.2)$$

where T is the bubbler temperature (75 °C).

The total pressure in the bubbler strongly depends on the Ar flow passing through. The dependence of the bubbler pressure on the flow has been measured using a pressure gauge mounted at the exit of the bubbler. The results are shown in Figure 4-6. The relation between the flow and the pressure drop can be fitted with a second order polynomial, consistent with the Hagen-Poiseuille equation for compressible flow through a tube.⁶⁸

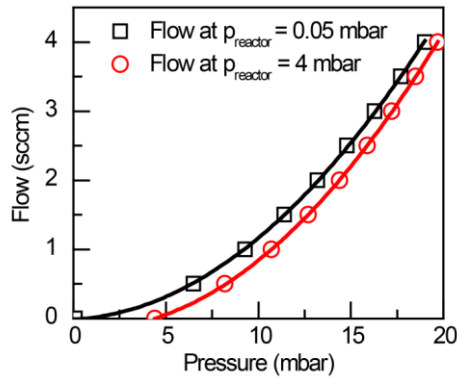


Figure 4-6: Relation between pressure and gas flow at bubbler exit, for two different reactor pressures. The lines are second order polynomial fits.

It should be noted that the pressure at the bubbler exit is only weakly dependent on the pressure in the reactor. This is caused by the inlet assembly and by the relatively long length of narrow tubing between the bubbler exit and the reactor, which both lead to significant pressure drops.

When p_{vap} is calculated from eq. 4.2 and assuming that p_{total} in eq. 4.1 is equal to the bubbler pressure, the flow of TDMAT can be estimated by iteration of eq. 4.1 and the polynomials obtained from fitting the data in Figure 4-6. With a bubbler temperature of 75 °C and a carrier gas flow of 0.5 sccm, the TDMAT flow is 0.34 sccm which is equal to 0.25 $\mu\text{mol/s}$. This means that a minimum time of 600 s is needed to coat 0.5 g of powder with a TDMAT monolayer.

The pulse time is much longer than experiments reported in literature,^{30, 142, 143, 155, 156} but can be decreased by increasing the precursor flow rate. This can be achieved by either increasing the precursor vapor pressure by increasing the bubbler temperature, or by reducing the total pressure in the bubbler by reducing the pressure drop over the tubes. The first solution is limited by the maximum temperature achievable in the reactor hardware and seals (100 °C). The second solution can be achieved by replacing the 1/8" tubes in the reactor section by 1/4". This will reduce the gas velocity in the tube by a factor of 4, resulting in a large decrease in pressure drop. Doing this will, however, increase the precursor residence time and the chances of undesired reactions in the tubes. We did not investigate the effects of these alterations.

A key requirement for true ALD growth is that the TDMAT adsorbs on the surface in a self-limiting fashion. If this is the case, the growth rate of the TiO_2 film per cycle saturates at high TDMAT doses. To investigate the saturation, a series of experiments were performed using the ALD scheme depicted in Figure 4-7. The TDMAT pulse time varied between 200 and 1000 s, while keeping the number of ALD cycles constant at 50. The reactor temperature was kept at 100 °C by tape heating and the air pressure on the vibrator was 6 bar. The total Ar flow during purges was 1.7 sccm, which was delivered through three lines in the following way: 0.2 sccm through MFC 1, 0.5 sccm through MFC 3 and 1.0 sccm through MFC 4 (cf. Figure 1). The flow of precursor then is added to this amount. The H_2O cycle time and flow rate are chosen to ensure full surface coverage. After each run, the particles were removed from the reactor and analyzed.

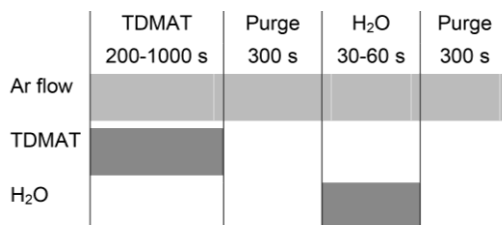


Figure 4-7: Pulse scheme of the ALD process.

Instead of measuring the layer thickness, which is common practice in ALD research on Si wafers but not trivial for powders, the total mass fraction of TiO₂ was measured. This is achieved by dissolving the TiO₂ shell in hot sulfuric acid and measuring the Ti concentration with a UV-vis spectrometer, with the method described by Diebold et al.¹⁵⁷ The concentrations were measured in 1 cm Perspex cuvettes with an Ocean Optics Maya Pro photospectrometer using a halogen light source.

The results are shown in Figure 4-8, in which the mass fraction of TiO₂ is plotted against the precursor dose. Instead of using the unit of Langmuir for the exposure, as is commonly done in the literature, the horizontal axis shows the experimentally more relevant metric of moles of TDMAT per moles needed for monolayer coverage. The latter value is estimated by multiplying the mass of the powder with the specific surface area and the estimated amount of TDMAT molecules per m² for a monolayer ($2 \times 10^{18} \text{ m}^{-2}$). Figure 4-8 reveals that the growth saturates at doses higher than $\sim 1 \text{ mol TDMAT/mol surface sites/cycle}$, as one would indeed expect. Under saturated growth conditions, the powder contains approximately 20 wt% of TiO₂ after deposition.

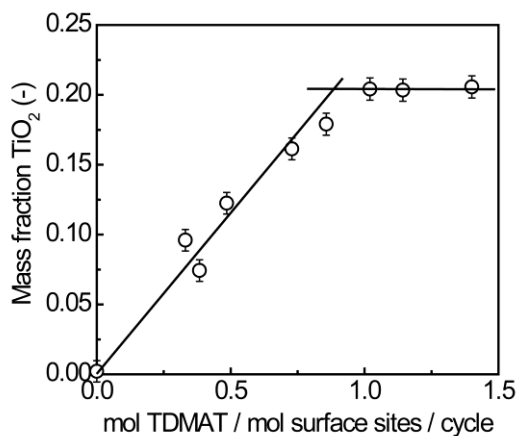


Figure 4-8: Saturation curve of TDMAT

The thickness and homogeneity for TiO_2 shells grown under saturated growth conditions are investigated with TEM (HAADF-STEM, TECNAI F30ST). Figure 4-9 shows images of uncoated particles and particles coated using 50 and 100 ALD cycles. The coated particles show a distinct white outer shell that is not present on the uncoated particles and hence must be the TiO_2 coating. Analysis of TEM images of other particles confirmed that the TiO_2 layer is present on all particles, irrespective of their size and shape.

Energy Dispersive X-ray spectroscopy (EDX) of large particle agglomerates indicate that the particles do not contain Ti before deposition, but that there is Ti present after 50 and 100 cycles of ALD. To confirm the composition of the shell, EDX line scans were performed across the edge of several particles. Typical example of line scans are given in Figure 4-9 (e) and (f) for 50 and 100 cycles respectively. The EDX spectra of the particles contain signals of oxygen, silicon, and titanium. At the point where the arrow crosses the white edge of the particle, clear peaks in the Ti signal and steep decreases in Si signal are observed. This indicates that the edges of the particle contain Ti, but do not contain Si. From this we conclude that SiO_2 - TiO_2 core-shell particles have been synthesized.

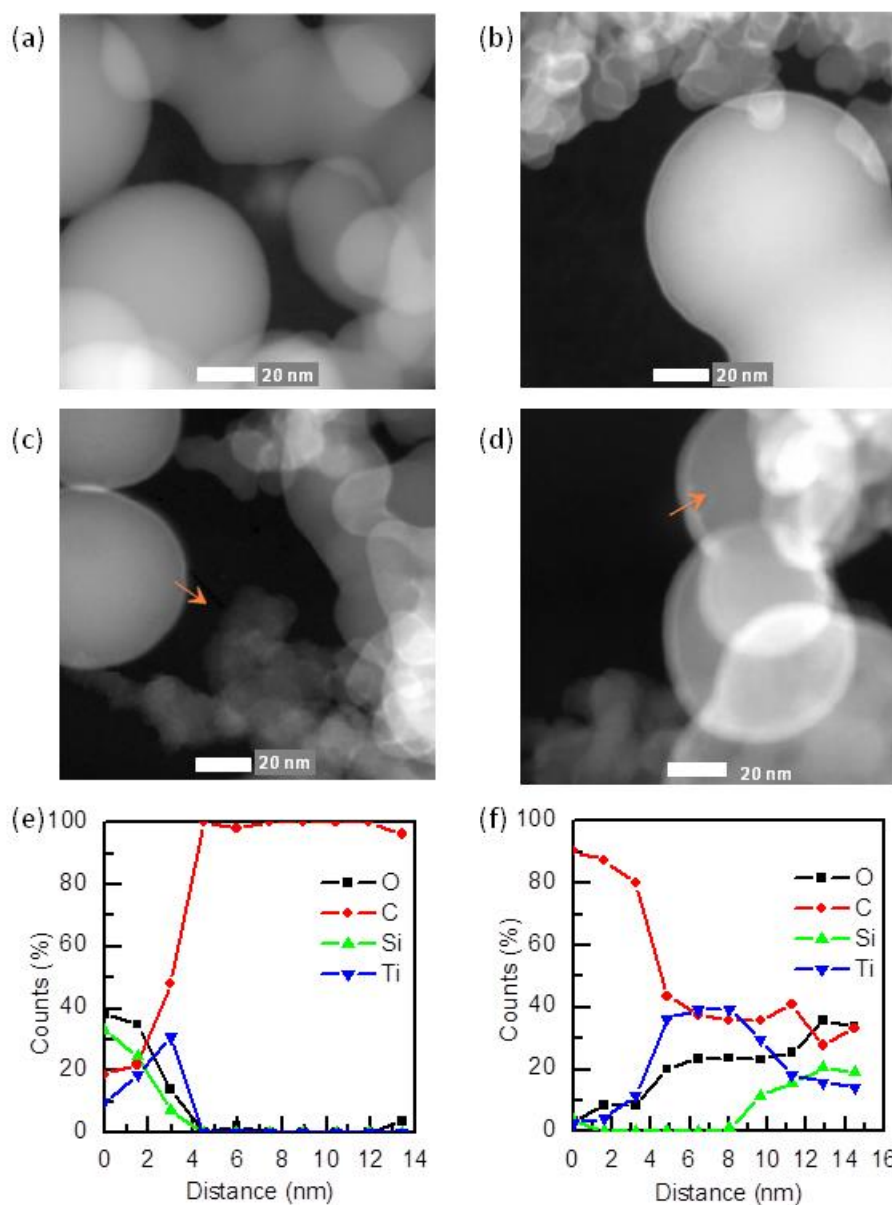


Figure 4-9: TEM images of the particles before (a) and after 50 (b and c), and 100 cycles (d) of ALD. The results of the EDX line scans along the arrows in figures (c) and (d) are shown in figures (e) and (f) respectively. Images were made using a high angle annular dark field (HAADF) detector.

The thickness of the shell, determined at 11 points on 9 particles by measuring the HAADF-STEM signal intensity across the edge of the particle, is 1.6 ± 0.2 nm for particles treated with 50 cycles ALD. This corresponds to a growth rate of 0.32 \AA/cycle . This value is lower than the values between 0.6 and 0.8 \AA/cycle reported in literature.^{39, 40, 44} The exact reason is not known, but can possibly be attributed to an incubation of growth. The nature of the surface can inhibit the growth initiation, causing the layer to be thinner than expected.^{49, 158}

At first sight, a film thickness of 1.6 nm does not seem enough to make up 20 wt\% of TiO_2 in the particle batch. This is true if only the bigger particles are considered. However, the particle size distribution is quite broad. For example, a SiO_2 particle with a diameter of 25 nm and a TiO_2 coating layer of 1.6 nm contains approximately 40 wt\% of TiO_2 whereas a 80 nm particle with an 1.6 nm shell has less than 20 wt\% TiO_2 . The exact particle size distribution could not be determined due to heavy agglomeration of the particles. However, the TEM images suggest that there are a significant number of particles with a diameter larger than the average value of 25 nm for a $90 \text{ m}^2/\text{g}$ powder. Based on this, the 20 wt\% of TiO_2 is not inconsistent with the 1.6 nm shell thickness.

To determine the growth rate per cycle, the powder was coated with 100 ALD cycles. The mass percentage of TiO_2 increased to 48% and the TEM image in Figure 4-9 (e) shows that the shells on the particles indeed are thicker. The shell thickness varied between 1.2 and 3.3 nm, the higher value being in good agreement with the growth rate of 0.32 \AA/cycle measured after 50 ALD cycles.

The spread in shell thickness is considerably larger for 100 cycles than for 50 cycles. The origin of this large spread is unknown but is probably caused by inhomogeneous fluidization. Due to deposition of large quantities of TiO_2 on the SiO_2 nanoparticles the particle agglomerate density and total powder mass increase. This can have an effect on the fluidization of the particles. Gradually increasing the gas flow during the deposition process will most likely improve fluidization and, hence, homogeneity. We did, however, not investigate this any further.

X-ray diffraction (Bruker D8 Advance) showed that the SiO_2 particles and the as-deposited TiO_2 coatings were amorphous. Upon annealing at 450 °C for 6 hours in air, the TiO_2 coatings transform into the anatase phase.

4.4 Conclusion

In this paper we have described the design and operation of a complete, stand-alone fluidized bed atomic layer deposition reactor. The active pressure control helps to stabilize the bed, which can be visually inspected by using a glass reactor vessel. The use of a particle filter inside the reactor was avoided by expansion of the reactor diameter at the top, which decreases the risk of clogging and pressure build-up. All parts of the apparatus have been designed in such a way that the reactor fits into a closed cabinet. The cabinet layout protects the environment and user in case of failure. We have also shown that SiO_2 - TiO_2 core-shell nanoparticles can be synthesized with our FB-ALD reactor. TEM images show that the particles have homogenous shells with a controllable TiO_2 mass fraction and, therefore, shell thickness. The thickness after 50 cycles is 1.6 nm and the mass fraction TiO_2 at saturation is approximately 20 wt%. Saturated growth conditions are achieved with TDMAT pulses that are longer than 600 s and H_2O pulses of 60 s. The deposition process can be adapted to deposit other materials, following the example of TiO_2 deposition given here. Key operating conditions determining the cycle time are gas flow, reactor pressure, and precursor vapor pressure.

5 DEPOSITION OF CONDUCTIVE TIN SHELLS ON SiO₂ NANOPARTICLES WITH A FLUIDIZED BED ALD REACTOR*

Conductive TiN shells have been deposited on SiO₂ nanoparticles (10-20 nm primary particle size) with fluidized bed atomic layer deposition using TDMAT and NH₃ as precursors. Analysis of the powders confirms that shell growth saturates at approximately 0.4 nm/ cycle at TDMAT doses of >1.2 mmol/g of powder. TEM and XPS analysis showed that all particles were coated with homogeneous shells containing titanium. Due to the large specific surface area of the nanoparticles, the TiN shells rapidly oxidize upon exposure to air. Electrical measurements show that the partially-oxidized shells are conducting, with apparent resistivity of approximately ~11 kΩ cm. The resistivity of the powders is strongly influenced by the NH₃ dose, with a smaller dose giving an orders-of-magnitude higher resistivity.

* This chapter has been accepted for publication in the Journal of Nanoparticle Research

5.1 Introduction

Nanoparticles and nanoparticle assemblies are the cornerstones of current material science and engineering. The nanometer size and structure provide properties and functionalities that make the particles interesting for a wide variety of potential applications such as microelectronics, solar energy conversion, sensors, catalysis, and batteries. Much research is being done on the synthesis of core-shell materials, in which the core and the shell are made of different materials and have different functionalities. For example, the shells can be used for corrosion protection^{9, 23-25} or improved catalytic performance,^{28, 29} whereas the bulk can be used as optical absorption center,²⁴ intercalation material for charge storage,¹⁵⁹ or inert support material.

When used in microelectronic devices, a low-resistivity of the nanoparticle assemblies and the ability to fabricate good electrical contacts to the nanoparticles are crucial for proper functioning. This can be very challenging to achieve. One solution is to coat the nanoparticles with a thin, electrically conducting layer using fluidized bed atomic layer deposition (FB-ALD). This technique, developed by Weimer et al.³⁰ combines the wide range of materials that can be deposited with ALD with the ability to coat large amounts of nanoparticles without having the diffusional limitations of ALD coatings in fixed beds,¹⁶⁰ and the scalability provided by fluidized bed reactors.¹⁶¹ ALD offers the possibility to grow ultra-thin coatings of a wide variety of materials in a controlled, atomic layer-by-atomic layer fashion. Earlier research by Hakim et al. shows that with this technique, through the process of dynamic aggregation of nanoparticle agglomerates, it is possible to coat individual nanoparticles with homogeneous layers.^{69, 162, 163}

In this paper, we report on the ALD of conductive TiN shells on non-conducting SiO₂ nanoparticles with a fluidized bed reactor. TiN is a low-cost material that is e.g. used as diffusion barrier for Cu or Al in silicon-based microelectronics and can be deposited at the relatively low temperatures required for nanoparticle processing by metal-organic ALD. Due to its conductivity, TiN also shows enhanced surface plasmon effects¹⁶⁴ that can be useful in applications such as sensors and photocatalysis.¹⁶⁵ Furthermore, TiN coatings,

deposited with conventional ALD have been reported to improve the performance of batteries made with lithium titanate spinel nanoparticles.¹⁶⁶

We have deposited the material with a low temperature process using tetrakis (dimethylamino-) titanium (TDMAT) and NH_3 as precursors. This chemistry was chosen over the more common TiCl_4 deposition process because of the large amounts of by-products that are formed due to the large specific surface area of the powder. When TiCl_4 is used, large amounts of highly corrosive HCl are formed that can damage downstream equipment. Furthermore, the use of TDMAT also avoids contamination of the powder with NH_4Cl , which is known to form in TiCl_4 -based processes.⁵³ Thermal ALD was used rather than plasma-enhanced ALD, even though PE-ALD should give superior coating quality on nanoparticles,¹⁶⁷ because it allows for a less complicated reactor design that is more easily scaled up.

We will show that the chosen chemistry and reactor design results in self-limiting growth of the TiN shells. Although the TiN layers almost completely oxidize after prolonged exposure to air, we find that the SiO_2 -TiN particle network is electrically conducting. These results represent a step forward in highly controlled gas-phase deposition of electrically conducting shells on powder-based nanoparticles.

5.2 Experimental

TiN coatings were deposited on SiO_2 nanoparticles with a specific surface area of $90 \text{ m}^2/\text{g}$ and an average diameter of $\sim 25 \text{ nm}$ (Aerosil 90, Evonik) using the fluidized bed ALD reactor described in chapter **Error! Reference source not found.**. Before deposition, the minimum fluidization velocity was determined by measuring the pressure drop at different Ar flow rates. TDMAT (SAFC hitech, electronic grade) and dried, gaseous NH_3 (Linde gas, grade 3.8) were used as precursors. NH_3 is dried by leading it through a CaO absorption bed to prevent oxidation of the TiN films by water present in the gas. TDMAT was admitted to the reactor by bubbling 1 sccm (standard cubic centimeter per minute) of Ar through the bubbler. The bubbler temperature was 80°C to ensure sufficient vapor

pressure, and the precursor supply lines were kept at 90 °C to prevent condensation. A constant additional flow of Ar (1.5 sccm) was fed into the reactor to assist in the fluidization of the particles. The ammonia was delivered by a mass flow controller with a flow range of 0-3 sccm that was equipped with NH₃-resistant Buna-N seals. The reactor was operated at 150 °C and 0.5 mbar. The temperature was selected in such a way that, according to literature on TDMAT-NH₃ processes,^{55, 57, 65, 84} high growth rates could be obtained without running the risk of TDMAT decomposition in the gas phase and concomitant unsaturated film growth.

The ALD reaction scheme of the TDMAT pulse → purge → NH₃ pulse → Purge cycles is given in Table 5-1. The number of cycles determines the layer thickness. After the last cycle (ending with a NH₃ pulse), a prolonged purge step was used to ensure that the reactor was completely free of TDMAT and NH₃ before being opened to recover the particles.

Table 5-1: Process scheme of FB-ALD reaction.

<i>Reaction step</i>	<i>TDMAT pulse</i>	<i>Purge</i>	<i>NH₃ pulse</i>	<i>Purge</i>
Time	600-1800 s	300 s	300 s	300 s
Ar Flow	2.5 sccm	2.5 sccm	2.5 sccm	2.5 sccm
TDMAT flow	~0.45 sccm*	0	0	0
NH ₃ flow	0 sccm	0 sccm	1 – 3 sccm	0 sccm

* estimated value, calculated by the method described in section 4.3

The Ti content of the powder was determined by first completely oxidizing the TiN to TiO₂ by annealing it at 250 °C in air for 6 hours, and then dissolving the TiO₂ in hot sulfuric acid before measuring the concentration of dissolved Ti with the UV/Vis method described in section 4.3. The core-shell structure was investigated in a transmission electron microscope (TEM, Zeiss Libra 200FE) equipped with an Omega-type energy filter. Zero-loss filtered images as well as elemental maps were acquired¹⁶⁸ using the Ti-L_{2,3}, N-K and O-K edge respectively.

X-ray photoelectron spectroscopy (XPS) measurements were carried out with a Specs XR50 X-ray source (Mg K α radiation) and a Phoibos 100 analyzer.

The conductivity of the powder was assessed by pressing a small amount of powder between two plates of conductive glass (F-doped SnO₂, TEC-15, 15 Ohm/square, Hartford Glass Co.) after which the resistance was measured with a digital multimeter (Keithley 2001). The electrode area was 45 mm² and the distance between the plates 50 μm. Control experiments were done with uncoated Aerosil 90, pure TiN powder (Sigma Aldrich, <3 μm particle size) and pure TiO₂ (Aeroxide P25, Evonik).

5.3 Results and Discussion

5.3.1 Oxidation of TiN Shell

After the deposition process the powders have a very dark green-brown color that is similar to that of fine TiN powder. When opening the reactor after the deposition, the powder rapidly changed to a light brown color upon contact with air. As thin porous TiN films are known to oxidize at the grain boundaries when brought into contact with air,^{57, 64, 169} this is most likely due to oxidation of the TiN to TiO_xN_y. The latter phase indeed has a light-brown to yellow color.

The fast oxidation of ALD-TiN in air means that special care has to be taken when removing the TiN-coated SiO₂ particles from the reactor. During the first test-experiments, the nanoparticles burn red-hot when opening the reactor too quickly. The result was a sintered piece of nanoparticle material. The temperature increase is attributed to the large amount of heat produced during the oxidation reaction: $\text{TiN} + \text{O}_2 \rightarrow \text{TiO}_2 + \frac{1}{2} \text{N}_2$ ($\Delta G^0 = -581 \text{ kJ/mol}$, $\Delta H = -607 \text{ kJ/mol}$). To illustrate how oxidation of a relatively thin shell of a nanopowder can indeed cause significant heating, consider a batch of 0.5 gram SiO₂ powder. With a heat capacity of 0.75 J/(g K) for SiO₂,⁶³ the total energy required to heat this batch of powder from room temperature (25°C) to 700°C is 253 J. This energy can be provided by oxidizing 26 mg of TiN to TiO₂, which corresponds to 5.2% of the total mass of the powder. This translates to a ~0.4 nm TiN shell around a 90 nm diameter SiO₂ particle, assuming both materials are fully dense. This surprisingly small number clearly shows that even incomplete oxidation of a thin TiN shell can generate enough heat to let the powder

become red-hot upon exposure to air (especially when the reaction accelerates itself due to thermal runaway).

To slow down the oxidation reaction, we filled the reactor very slowly with air. Opening the reactor slowly does not completely prevent the oxidation, but it slows down the reaction rate and thus prevents the powder from burning and sintering.

5.3.2 Film growth rate

If film growth occurs in the self-limiting growth regime that is characteristic for ALD, the TiN layer thickness should be independent from the TDMAT dose. To verify this, batches of 0.5 g powder were coated with 50 ALD cycles using different TDMAT dosages while keeping the NH_3 dose constant. The TDMAT flow is calculated from the Ar flow, the pressure in the precursor bubbler, and the saturated vapor pressure of TDMAT, with the method described in section 4.3. The base gas flow rate used for fluidization was 2.5 sccm, and this did not include the additional gas flow due to the precursor doses. The gas flow rate was thus well above the measured minimum fluidization flow rate of 1.5 sccm determined by measuring the gas flow at which the pressure drop remains constant (see Figure 4-5).

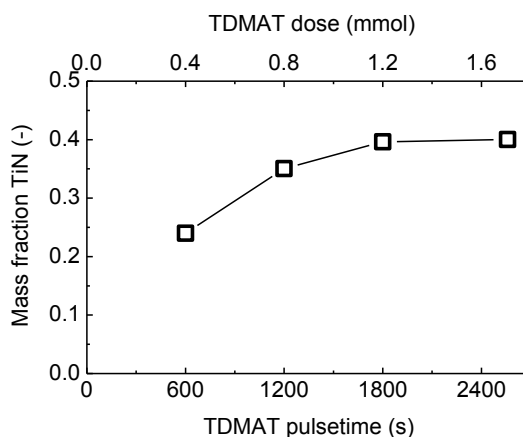


Figure 5-1: concentration of TiN on particles in relation to the TDMAT dose. The mass fractions were measured after 50 ALD cycles for all datapoints. The NH_3 pulse time was 300 s at a flow rate of 1 sccm. The reactor was operated at 150 °C and 0.5 mbar.

The concentration of TiN is calculated from the total amount Ti in the powder as measured by UV-vis. The data presented in Figure 5-1 show that the growth of TiN saturates at TDMAT doses > 1.2 mmol/g/cycle, indicating that we indeed operate in the self-limiting growth regime.

The growth per cycle (*GPC*) can be estimated from the mass fraction x by using the equation

$$GPC = \frac{d_0}{2N} \left(\sqrt[3]{\frac{x}{1-x} \frac{\rho_{SiO_2}}{\rho_{TiN}} + 1} - 1 \right) \quad (5.1)$$

In this equation, d_0 is the primary particle diameter (nm), N the number of cycles, and ρ_{SiO_2} and ρ_{TiN} the density of SiO_2 and TiN, respectively. The derivation of this equation can be found in the appendix. The density of amorphous SiO_2 is 2.65 g/cm^3 ,⁶³ whereas for the density of ALD-TiN an estimated value of 3.0 g/cm^3 (as reported in literature for thermal TDMAT- NH_3 deposition processes)^{65, 84} was used. The estimated primary particle size, based on a specific surface area of $90 \text{ m}^2/\text{g}$ and a density of 2.65 g/cm^3 , is 25 nm. With this particle diameter, the *GPC* is equal to approximately 0.4 \AA/cycle . This value is in the lower range of the $0.4 - 1.2 \text{ \AA/cycle}$ growth rates reported in literature for thermal TDMAT/ NH_3 ALD processes.^{55, 57, 84}

The efficiency of precursor use is calculated by comparing the precursor dose per gram to the mass fraction of TiN. The mass fraction is 0.4, which means that the total amount of TiN deposited is 5 mmol and the deposition efficiency of TDMAT is approximately 16.7%. For NH_3 the efficiency is much higher, roughly 50% of the nitrogen atoms admitted into the reactor as NH_3 ends up in the film. This is much lower than the near 100 % efficiency that one would normally expect for fluidized bed ALD processes¹⁴².

Possible explanation for the lower *GPC* and efficiency is growth inhibition in the first deposition cycles, or incomplete coverage of the particles due to clustering of the nanoparticles (agglomeration). Growth inhibition may occur, but since the *GPC* actually *decreases* after 20 cycles (*vide infra*) it seems unlikely that this can explain the low deposition efficiencies. Agglomeration would lead to some particles being blocked from

contact with the gas. While we cannot rule this out completely, we found no indication whatsoever of partially coated particles in our TEM analysis (*vide infra*). This is consistent with the process of dynamic aggregation as described by Hakim et al., suggestion that our SiO₂ powders only form so-called ‘soft aggregates’ that can be broken up by the fluidization process.^{69, 162, 163}

Another possible cause for the low efficiency is the presence of inhomogeneities in the fluidized bed, which would reduce the mass transfer rate between the gas-phase and the particle surface. In a homogeneously fluidized bed, mass transfer is usually not rate-limiting because the residence time of the gas is orders of magnitude longer than the time-scale at which mass transfer takes place. The presence of large gas bubbles and channeling effects can, however, lead to poor mass transfer between gas-phase and particle surface and, hence, poor precursor efficiency.¹⁷⁰ Although we cannot rule this out, visual inspection of the bed and the data in Fig. 1 did not give any indication of inhomogeneous fluidization.

Besides agglomeration and bed inhomogeneities, there is a growth limitation that is inherent to the TDMAT process. Dimethylamine — a by-product of the deposition reaction — is known to adsorb strongly on TiN surfaces and in such a way block TDMAT adsorption sites.¹⁷¹ Due to the intimate contact between the gas phase and the particles, this effect is more strongly present in fluidized bed ALD reactors than in conventional ALD reactors. The difference between the processes is depicted in Figure 5-2. In conventional ALD (on fixed substrates), re-adsorption of dimethylamine is usually not a major issue because, as soon as the DMA molecules are released from the surface, they are quickly transported to the reactor exit by the feed gas and do not get a chance to re-adsorb to the substrate. However, in a fluidized bed reactor, a dimethylamine molecule will have to pass many particles on its way to the exit, dramatically increasing the chance to re-adsorb on a particle surface. Whereas the increased chance of (re-)adsorption of precursor molecules is the reason that precursor efficiency is usually extremely high in fluidized bed reactors, we believe that the re-adsorption of reaction by-products which block the adsorption sites is the reason that the GPC and the precursor efficiency are rather low for the TDMAT-NH₃ FB-ALD process.

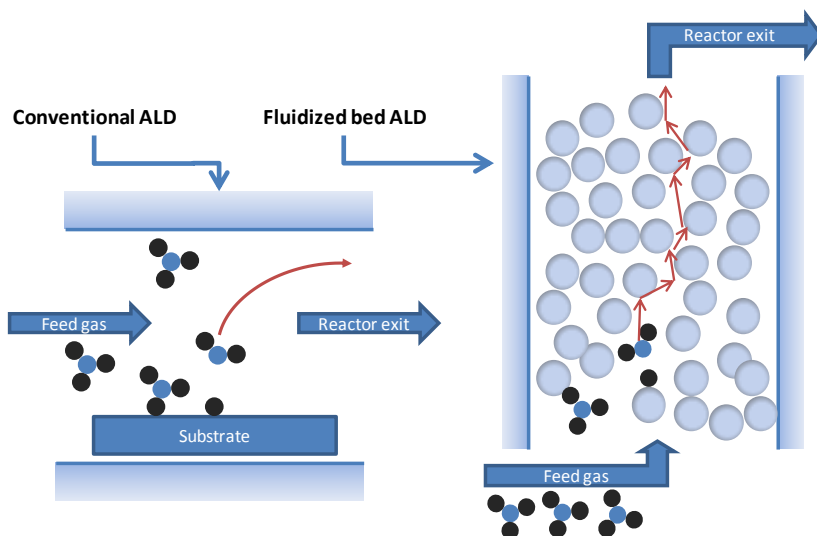


Figure 5-2: Removal of a DMA molecule by sweep gas in a “conventional” ALD reactor with a single substrate and a fluidized bed ALD reactor filled with particles. Once a TDMAT molecule has attached to the substrate surface, the released DMA molecule has to travel through the reactor to the exit.

Knowing the saturated growth rate to be 0.4 \AA/cycle , the next step is to determine whether this growth rate remains constant with increasing number of cycles. To investigate this, batches with identical TDMAT and NH_3 doses (1200 s and 300 s pulses, respectively) but with different number of ALD cycles have been prepared. The data presented in Figure 5-3 (red squares) show that the TiN mass fraction increases with increasing amount of cycles. The growth rate, however, strongly decreases after depositing 50 cycles, as indicated by the black circles in Figure 5-3.

The decreasing average growth rates could indicate that growth enhancement rather than growth inhibition is occurring during the first cycles. This phenomenon has been reported before for TiN-ALD on Si wafers with TDMAT and NH_3 as precursors.⁵⁵

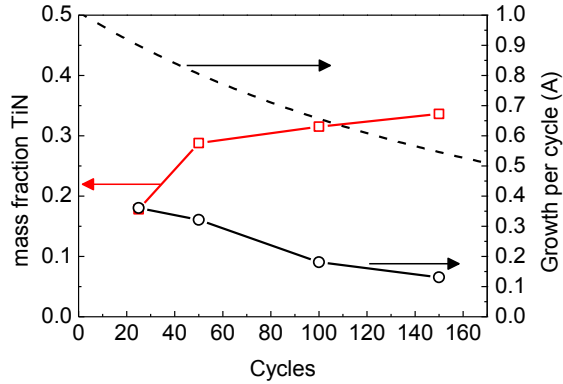


Figure 5-3: TiN mass fraction (squares) and growth per cycle (circles) with constant 1200 s TDMAT and 300 s NH₃ dose. (The lines serve as a guide to the eye). The maximum achievable growth rate per cycle as calculated from the TDMAT and NH₃ doses is indicated by the dashed line.

Another explanation could be under-exposure to either TDMAT or NH₃. To illustrate this, assume that the respective exposures of TDMAT and NH₃ are x and y mol per cycle, and that $x < y$. Then, a maximum TiN deposition rate of x mol per cycle can be achieved. During cycle n , the total amount of TiN per cycle x has to be deposited on a surface area A_{n-1} , causing an increase in particle diameter and, concomitantly, surface area. Assuming that the increase in particle diameter is much smaller than the particle size, the surface area of the particles after cycle n can be estimated with the equation

$$A_n = A_{sp} \frac{\left(d_0 + \frac{2x}{\rho_m A_{n-1}} \right)^2}{d_0^2} \quad (5.2)$$

in which A_{sp} is the total specific surface area for the current batch of powder (m²), d_0 is the average diameter (m) of the uncoated particles, and ρ_m is the molar density (mol/m³). A NH₃ dose of 300 s at a rate of 1 sccm equals 1.3 mmol of NH₃, which means that, if all NH₃ is used, a maximum TiN growth rate of 1.3 mmol per cycle can be achieved (x in equation (2)). The resulting maximum growth per cycle in Ångstroms is given in Figure 5-3 (dotted line). The calculated GPC shows a similar decay with increasing number of cycles as the

experimentally determined GPC, which confirms that under-dosing is indeed a possible explanation for the decrease in GPC. However, since only 16% and 50% of the admitted TMDAT and NH₃ shows up in the deposited shells, respectively, it seems unlikely that the observed decrease in GPC is caused by under-dosing.

A third reason the reduced growth rate can be found in improper fluidization of the particles. When the particle bed is not properly fluidized, gas can by-pass the particle beds, limiting the chances of contact between precursor molecules and particles. The fluidization of particles is influenced by their density, diameter, and the Van der Waals forces between the particle agglomerates. The presence of a conducting TiN shell will influence the density and attractive forces of the particles. Because TiN has a higher density than SiO₂, the density of coated particles and agglomerates is also higher, making them more difficult to fluidize. Furthermore, attractive van der Waals forces (F_{vdW}) between particles are material-dependent. This dependency is characterized by the Hamaker constant A_H in the equation

$$F_{vdW} = \frac{A_H R}{12a^2} \quad (5.3)$$

in which R is the sphere radius and a the separation between the particles. The theoretical Hamaker constant of TiN is approximately 2-3 times higher than that of SiO₂.¹⁷² This means that the attractive forces will increase during TiN deposition, which will negatively influence the ability of the powders to be properly fluidized.¹⁷³ This will reduce the exposure of the particles to TDMAT.

It should be noted here that the exact specific surface area of the batch is unknown and that such measurements would be unreliable due to the rapid oxidation of the particles and the concomitant increase in shell thickness, particle diameter and specific area. Analysis of reactor effluent composition by e.g. mass spectrometry should provide more clear insight in the causes of the low efficiency and decline in GPC.¹⁴² This technique was, however, not available to us during this study.

5.3.3 Shell composition and structure

Three TiN-coated powders, prepared with varying number of ALD cycles and precursor pulse lengths, were removed from the reactor and analyzed with XPS. The results of the XPS analysis, presented in Figure 5-4, shows that all powders contain Ti and N. This provides compelling evidence that some form of titanium nitride has been deposited. At the same time, the strong O signal indicates that, at least part of, the TiN shells were oxidized. This probably occurred when opening the reactor and during transport from the reactor to the XPS system.

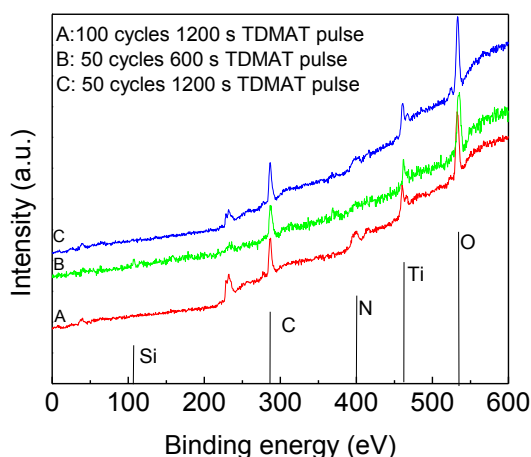


Figure 5-4: XPS analysis of three different core-shell powders produced under different circumstances. The letters A, B, and C in the graph correspond to that in Table 5-2. The curves are offset for clarity.

The unavoidable oxidation of the TiN shell makes it impossible to confirm whether the deposited phase is TiN, Ti_3N_4 , or TiO_xN_y . However, oxide formation during the deposition reaction is highly unlikely because the lack of oxygen-containing compounds during reaction.

Integration of the XPS peaks with dedicated software shows that the surface of the particles in certain cases contain traces of Si (<8.8 atom% for sample B, green curve) This is tentatively attributed to the fact that the penetration depth of the XPS signal (~3 nm)

may slightly exceed the film thickness. However, we cannot rule out the possibility that the shells are not completely closed, so that some of the underlying SiO₂ is still exposed.

Table 5-2: Overview of sample preparation conditions and atomic fractions according to the analysis of the XPS results. The numbers in brackets give the peak area in the XPS measurements.

<i>Powder</i>	<i>A</i>	<i>B</i>	<i>C</i>
Cycles	100	50	50
NH ₃ flow	1	1	1
TDMAT pulse time (s)	1200	600	1200
Weight fraction TiN*	0.32	0.24	0.29
Atomic comp. (%) (peak area)			
C1s	46.9 (24592)	45.7 (15730)	47.2 (27676)
N1s TiN	8 (7043)	3.6 (2091)	6.9 (6766)
O1s SiO ₂	35.8 (46112)	38.8 (32820)	38 (54744)
Si2s SiO ₂	3.2 (1744)	8.8 (3106)	3.2 (1907)
Ti2p TiO ₂	6.1 (22274)	3.1 (7462)	4.8 (19855)
Ratio Si/Ti	0.5	2.8	0.7
Ratio N/Ti	1.3	1.2	1.4

*Estimated TiN of the particles before contact with air.

The homogeneity of the shells was investigated with TEM. The bright-field TEM image of particles treated with 100 ALD cycles given in Figure 5-5a shows a well-defined core-shell structure for all particles. The shell thickness is highly homogeneous and has a value of approximately 4-5 nm, which is higher than the value estimated from the TiN mass fraction of the powder. This difference is most likely due to the (partial) oxidation of the TiN film, or to the fact that the TiN films are not fully dense.

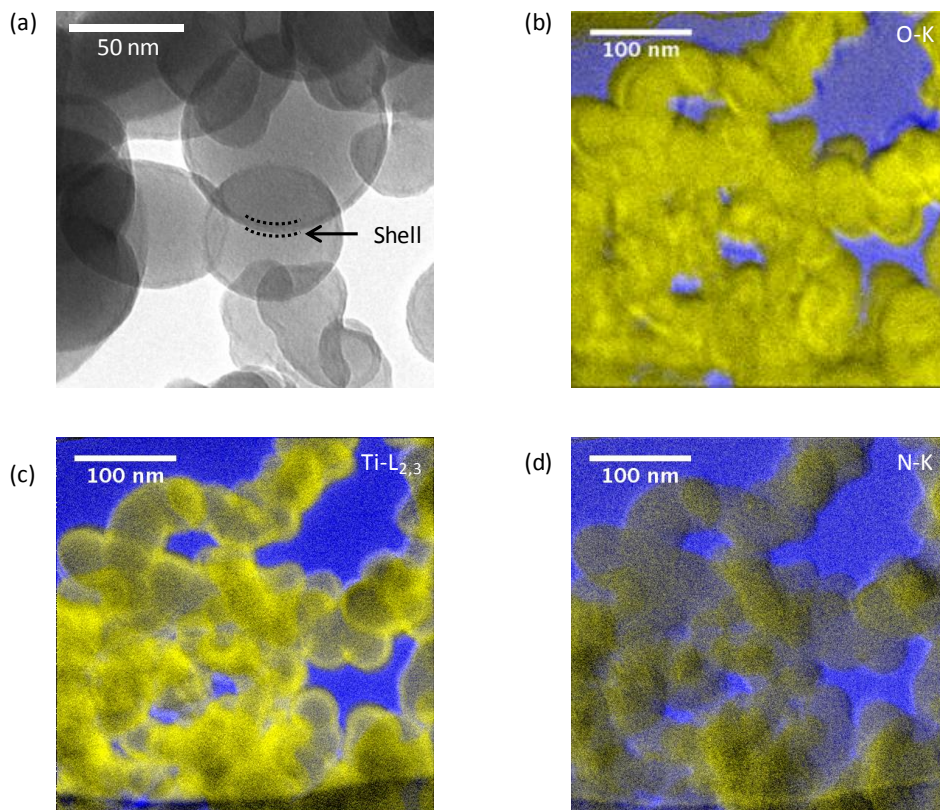


Figure 5-5: (a) zero-loss filtered TEM bright-field images of $\text{SiO}_2\text{-TiO}_2$ nanoparticles after 100 cycles ALD clearly showing the core-shell structure. Images (b), (c), and (d) respectively show the O, Ti, and N distribution as obtained by elemental mapping. The light (yellow) dots indicate presence of O, Ti, and N.

Figure 5-5b, Figure 5-5c, and Figure 5-5d depict the elemental distribution of O, Ti, and N, respectively, for the particles. The higher Ti signal at the edges of the particle silhouettes in figure (c) proves that Ti abundance is indeed higher in the surface layer of the particles. The N distribution shows that the concentration of N atoms is not homogeneously distributed over the different particles. Furthermore, the overall concentration of N-atoms seems much lower than the Ti concentration. The O distribution (Figure 5-5b) is quite homogeneous over the particle and the shells are not clearly visible. This confirms

that the indeed the Ti on the shell was oxidized. This is in agreement with the XPS analysis, and is attributed to (partial) oxidation of the TiN upon exposure to air.

5.3.4 Shell conductivity

To verify that the TiN coating is conductive, the electrical resistance of small amounts (approximately 10 mg) of powder pressed between two 45 mm² conducting glass (FTO) electrodes was measured and compared to control samples. The results given in Figure 5-6 show that a resistance of 10 M Ω was measured for particles produced with a NH₃ dose of 300 s per cycle at 1 sccm, whereas 300 s flow at 3 sccm resulted in a resistance of 1 k Ω .

For comparison, the resistances of commercial TiN, SiO₂ and TiO₂ powders were measured as well. The commercial TiN powder has a negligible resistance; the measured value of 40 Ω is due to the resistance of the FTO glass. This is consistent with small bulk resistivity of TiN (typically less than 100 $\mu\Omega$ cm) from which a powder resistance of <1 Ω is expected. The resistance of the Aerosil powder is beyond the measuring range of the multimeter (200 M Ω), whereas P-25 TiO₂ has a resistance of 2 M Ω . These results clearly show that the TiN shell, even after being partially oxidized, greatly improves the overall conductivity of the SiO₂ powder.

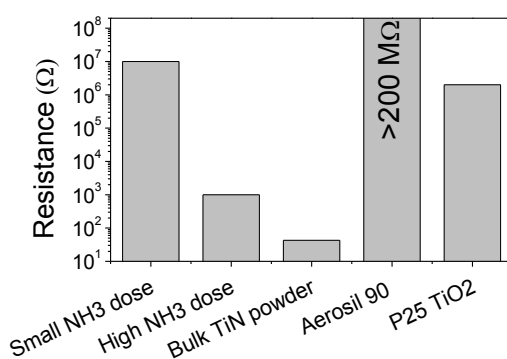


Figure 5-6: Resistance of core-shell powder synthesized with a small and a high NH₃ dose and control samples of pure TiN, uncoated Aerosil powder and P25 TiO₂.

Assuming a powder fill fraction of $\sim 30\%$ and a TiN volume fraction in the particles of approximately 45% (assuming a 2.6 nm shell of pure TiN on a 25 nm particle) an apparent TiN resistivity of 11 k Ω cm is calculated using the equation $\rho = RA\varepsilon V_{\text{TiN}}/L$, in which ε is the volume fraction of powder (-), V_{TiN} is the assumed volume fraction TiN in the powder (-), A is the area of the measurement electrodes (0.45 cm²), and L is the length between the two measurement electrodes (0.005 cm). The measured resistivity of the layer of core-shell particles is thus several orders of magnitude higher than that of bulk TiN, for which the resistivity typically is less than 100 $\mu\Omega$ cm, and ALD-TiN, for which the resistivity is typically in the order of m Ω cm to Ω cm.^{51, 55, 57, 58, 60} The much larger resistance can be caused by different factors. First of all, the resistivity of ALD-TiN depends strongly on the deposition conditions: deposition temperature, NH₃ exposure, and use of plasma-enhanced ALD influence the film structure and impurity concentration in the film.^{57, 58, 60} Earlier work on thermal and plasma-enhanced TiN deposition on nanoparticles even showed that the resistivity of TiN coatings deposited with thermal ALD was so large, it could not be measured.¹⁶⁷ The influence of deposition conditions is also demonstrated in this work by the difference in resistance between the sample with a small and large NH₃ dose. Furthermore, the resistivity of thin TiN films varies strongly with film thickness and is seen to increase sharply at thicknesses smaller than 10 nm (as measured with in-situ ellipsometry during ALD)⁶⁰ or even below 50 nm (measured ex-situ with four-point probe measurements).¹⁷⁴ But the most important factor that increases the resistivity of the films is likely to be the oxidized layer on top of the partially oxidized TiN shell (depicted in Figure 5-7). The insulating oxide layer forms a large potential barrier between two particles that will have a large effect on the total resistance of the powder. Furthermore, the presence of uncoated particles could also affect the apparent resistivity of the material, although it is not expected to have the order-of-magnitude influence that is measured here. We did not, however, investigate this in more detail.

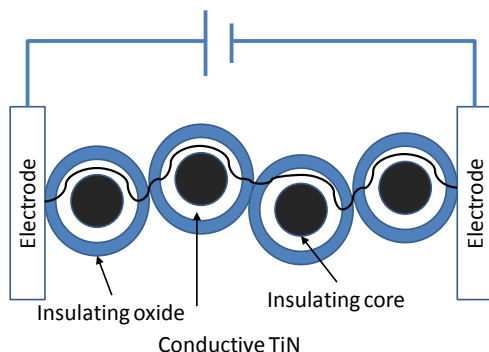


Figure 5-7: Illustration of an electron path through a layer of core-shell particles

5.4 Conclusions

We have successfully deposited conductive TiN shells on SiO_2 nanoparticles with fluidized bed atomic layer deposition. The growth saturated at approximately 0.4 \AA/cycle after 50 cycles with high TDMAT dosage. The growth rate decreased when the number of cycles increased. The particles have the desired core-shell structure and XPS measurements confirm that we indeed have deposited a coating containing Ti and N. However, exposure of the TiN- SiO_2 core-shell nanoparticles to air rapidly oxidizes the TiN to TiO_xN_y , which prevented unequivocal identification of the deposited TiN phase. The (partially oxidized) TiN shells are electrically conducting with an apparent resistivity of $> 10 \text{ k}\Omega \text{ cm}$. This resistivity is much higher than expected for pure TiN shells, which is attributed to the (partial) oxidation of TiN.

5.5 Appendix

The dimensions of the core-shell particle are given in Figure 5-8.

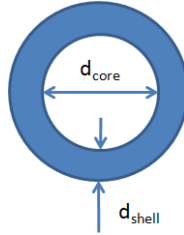


Figure 5-8: Definition of d_{core} and d_{shell}

The mass fraction x is defined as the ratio of the shell mass and the total mass of the core-shell particle.

$$X_{TiN} = \frac{m_{shell}}{m_{shell} + m_{core}} \quad (5.4)$$

The mass of the core is equal to

$$m_{core} = \frac{\pi}{6} \rho_{SiO_2} d_{core}^3 \quad (5.5)$$

The mass of the shell is equal to

$$m_{shell} = \rho_{TiN} \frac{\pi}{6} ((d_{core} + 2d_{shell})^3 - d_{core}^3) \quad (5.6)$$

Using equations 5.5 and 5.6 in 5.4 and rewriting yields

$$d_{shell} = \frac{d_{core}}{2} \left(\sqrt[3]{\frac{x}{1-x} \frac{\rho_{SiO_2}}{\rho_{TiN}} + 1} - 1 \right) \quad (5.7)$$

Assuming a constant growth rate (*GPC*) one can relate the shell thickness to the amount of cycles N .

$$d_{shell} = N \times GPC \quad (5.8)$$

This results in

$$GPC = \frac{d_{core}}{2N} \left(\sqrt[3]{\frac{x}{1-x} \frac{\rho_{SiO_2}}{\rho_{TiN}} + 1} - 1 \right) \quad (5.9)$$

6 SUMMARY AND OUTLOOK

Reducing particle size or material structure size to nanometer scale (10^{-9} m), can make the material properties, such as light absorption and electronic structure, change compared to the same materials at normal scale. This gives them properties that can make them suitable for the development of highly efficient and improved micro-electronics, sensor, medicine, batteries, catalysts and third generation solar cells.

There are, however some challenges that need to be overcome in the development of nanoparticle-based devices. The first is protection of nanoparticles against corrosion and oxidation. This phenomenon is increased by the large surface area available for corrosion. Furthermore, when nanoparticles or nanostructures are used in electronic devices, low-resistive electrical contacts should be made between electrodes and nanoparticles. The second challenge is, thus how to make electrical contacts without compromising the material's nanostructure.

This thesis deals with the development of a synthesis process for core-shell nanoparticles, existing of a core that is coated with a thin layer of material that is able to provide protection, or electrical contacts.

The first chapter describes the electrical contact between titanium nitride (TiN), which is a metallically conductive material that is used as contact material in electronic devices, and cadmium sulfide (CdS), a II-IV semiconductor that is used in (second generation) thin film solar cells and to increase light absorption in Grätzel-type solar cells. The experiments show that indeed we can make a Ohmic contact between TiN and CdS, meaning that the contact resistance between the two materials is low and that current is not blocked by the contact.

The use of thin coatings as protective layers is investigated by coating thin CdS films, which can be used as photo-catalyst in solar hydrogen production cells, with thin, inert titanium dioxide (TiO_2) to protect the CdS from corrosion under influence of solar

radiation. The goal of this research was to deposit a TiO_2 layer that was thick enough to provide full protection against corrosion, yet thin enough to enable electrons to be transferred between the CdS electrode and the electrolyte.

The TiO_2 coating was deposited with Atomic Layer Deposition (ALD), a technique used to deposit extremely thin layers of material by letting two precursors (A and B) react on the surface of a substrate to form product C. The first step in this process is chemisorption of precursor A. This chemisorption reaction is self-limiting and stops whenever the complete substrate is covered with a monolayer of component A. After completion of pulse A, precursor B is fed to the reactor and reacts with component A to form component C and prepare the surface of the substrate for a new pulse of component A. By repeating this cycle coatings can be made atomic layer by atomic layer.

The experiments with TiO_2 -coated CdS films in photoelectrochemical hydrogen production cells show that, even though the samples are coated with protective TiO_2 layers, the CdS remains sensitive to photocorrosion. The photocorrosion mechanism is investigated with electrochemical measurements in which the photocurrent over time can be described with a model that strongly resembles the Johnson-Mehl-Avrami model for phase transitions in solids. Analysis of the experimental results with the model shows that the corrosion starts in small defects in the TiO_2 coating and that the corrosion spreads mostly in lateral directions.

The next step in the research was to deposit coatings on individual nanoparticles with a fluidized bed ALD reactor (FB-ALD) that was specially developed for this purpose. In this reactor, the nanoparticles are agitated by a constant flow of inert carrier gas. The ALD precursors, tetrakis-dimethylaminotitanium (TDMAT) and water, are added to the carrier gas and hence brought into contact with the nanoparticles and layer-by-layer form a TiO_2 shell on the particles. In the design of the reactor that, is used for loose nanoparticles, care has been taken to make the reactor both safe and versatile in operation. Furthermore, the possibility of extensive monitoring of the reactor is provided.

With this reactor, silica (SiO_2) nanoparticles are coated with 1.6 nm TiO_2 layers. The growth rate is 0.32 Å per ALD cycle and independent of precursor pulse time and exposure. Electron microscope analysis (TEM) tells us that particles have a core-shell structure in which the SiO_2 core is coated by a homogenous TiO_2 layer.

To show that this deposition technique can also be used to deposit conductive coatings on nanoparticles, SiO_2 nanoparticles have been coated with conductive TiN layers. In this case TDMAT and ammonia (NH_3) were used as precursors. The growth rate of TiN showed the saturation plateau that is typical for ALD growth but depended on the amount of ALD cycles: more cycles led to a lower growth rate. This decline in growth rate can be attributed to the formation of reaction by-products that can adsorb on the particle surface and hence block the adsorption of precursor molecules. The TiN-coated nanoparticles did show good electrical conductivity, with a resistance that depended strongly on the deposition conditions.

The results of this research are a step towards the use of FB-ALD in the synthesis of core-shell nanoparticles, with batteries and nanostructured third generation solar cells as the most promising applications. Future research should focus on technological challenges of the FB-ALD technique itself and, on a fundamental level, on optimization of the core-shell structure.

The fundamental questions relate to the electronic structure of the nanoparticles: the behavior of nanostructured materials can be fundamentally different from behavior of “normal materials”. Fundamental studies, based on calculations and simulations of electronic structure, can determine the ideal core-shell material combination for each application. The particles can be synthesized in a fluidized bed ALD reactor.

In the further development of the FB-ALD technique, safety, with respect to the processing of loose nanoparticles, will be the most important aspect to be looked at, especially when dealing with (nano-) toxic materials and materials that are easily oxidized in air. This is mostly important for loading fresh particles and unloading of processed particles. The importance of a proper loading and unloading procedure has been

demonstrated with the TiN-coated particles that spontaneously ignited when they came in contact with air.

Another, more practical challenge is controlling nanoparticle agglomeration and maintaining a stable, homogeneously fluidized particle bed at large scale. Several techniques are available, besides the vibrating fluidized bed described in this thesis, to break agglomerates and create an homogeneous fluidized bed at lab scale. Scale-up of these techniques should be investigated. Furthermore, the static head (pressure drop) of large scale fluidized beds is often higher than the desired absolute operating pressure of the ALD reaction. The influence of the relatively large pressure drop over the bed on fluidization homogeneity should be thoroughly investigated.

Despite the technological challenges that come with scaling up of the technique, FB-ALD is a promising technique for the production of core-shell nanoparticles. The flexibility in materials selection, both for the core and the shell, and the homogeneity and quality of the coatings will provide a large advantage over other techniques.

7 SAMENVATTING EN VOORUITBLIK

Door het verkleinen van deeltjes of materiaalstructuren tot de nanometer schaal (10^{-9} m) kunnen de materiaaleigenschappen, zoals lichtabsorptie, elektronenstructuur, wezenlijk veranderen ten opzichte dezelfde materialen op normale schaal. Dit geeft ze interessante eigenschappen die ze geschikt kunnen maken voor het efficiënter maken en verbeteren van micro-elektronica, sensors, medicijnen, batterijen, katalysatoren en derde generatie zonnecellen.

Er zijn echter nog een aantal uitdagingen die de ontwikkeling van praktische toepassingen op basis van nanodeeltjes in de weg staan. De eerste is het beschermen van de nanodeeltjes tegen corrosie en oxidatie. Dit fenomeen wordt versterkt door er een groot oppervlak beschikbaar is voor de oxidatiereactie, waardoor dit extra snel gaat.

Verder moet op nanodeeltjes, wanneer ze gebruikt worden in elektronische toepassingen, een elektrisch contact met een lage weerstand aangebracht kunnen worden. De tweede uitdaging is dus het aanbrengen van goed geleidende elektrische contacten op nanodeeltjes zonder daarbij de nanostructurering teniet te doen.

In dit proefschrift wordt het onderzoek naar de synthese van core-shell nanodeeltjes, een nanodeeltje bestaande uit een kern met daaromheen een dunne coating die zowel bescherming biedt tegen oxidatie als wel elektrisch geleidend is, beschreven.

In het eerste hoofdstuk beschrijven we het elektrische contact tussen titaannitride (TiN), een metallisch geleidende verbinding die veel wordt gebruikt in de elektronica-industrie als contactmateriaal, en cadmium sulfide (CdS), een II-VI halfgeleider die wordt toegepast wordt in (tweede generatie) dunnelaag zonnecellen en om lichtabsorptie te vergroten in zogenaamde Grätzel-zonnecellen. Uit de experimenten met TiN contacten op dunne polykristallijne CdS films blijkt dat het elektrisch contact tussen TiN en CdS Ohms is. Dit betekent dat het contact een lage weerstand heeft en overdracht van elektronen niet blokkeert.

Het gebruik van dunne coatings als bescherm laag voor is onderzocht door dunne CdS films die bijvoorbeeld kunnen worden gebruikt als fotokatalysator in waterstofproductiecellen, te coaten met een inerte titaandioxidelag (TiO_2) om zo corrosie onder invloed van licht tegen te gaan. Het doel van dit onderzoek was om de laagdikte van TiO_2 te bepalen waarbij de laag enerzijds voldoende dik is om CdS te beschermen tegen corrosie, en anderzijds dun genoeg is om het elektrisch contact tussen CdS en het elektrolyet niet in de weg te staan.

De TiO_2 laag is aangebracht met behulp van AtoomLaagDepositie (ALD), een techniek waarbij extreem dunne lagen van een materiaal worden gededponeerd door pulsgewijs kleine hoeveelheden van precursor A en B op een oppervlak te laten neerslaan en te laten reageren tot product C. De eerste stap is chemisorptie van precursor A. Doordat deze neerslagreactie zelf-limiterend is, stopt de reactie nadat het hele oppervlak bedekt is met een monolaag van precursor A. Nadat de verzadiging bereikt is, wordt de het substraat in aanraking gebracht met precursor B die reageert tot stof C en het oppervlak weer klaarmaakt voor een volgende puls van precursor A. Door deze cyclus te herhalen kan, atoomlaag voor atoomlaag, een coating worden aangebracht.

Uit de experimenten met TiO_2 -gecoate CdS films die werden gebruikt als fotoanodes blijkt dat, ondanks de TiO_2 bescherm laag, de CdS films nog steeds zeer gevoelig zijn voor fotocorrosie. Het mechanisme van de corrosie is onderzocht met behulp van elektrochemische metingen waarbij de stroomsterkte over de tijd kan worden gefit met een model dat sterke wiskundige gelijkenissen vertoont met het Johnson-Mehl-Avrami model voor fase-overgangen in vaste stoffen. Uit analyse van de metingen is gebleken dat de corrosie begint in kleine oneffenheden in de TiO_2 coating van waaruit de corrosie zich in laterale richting uitspreidt.

De volgende stap in het onderzoek was om coatings aan te brengen op losse nanodeeltjes. Hiertoe hebben we een fluide bed ALD reactor (FB-ALD) ontwikkeld, waarin de nanodeeltjes in beweging worden gebracht met behulp van een inert draaggas. Aan dit draaggas worden pulsgewijs de precursors tetrakis-dimethylaminotitanium (TDMAT) en

water voor de ALD-reactie toegevoegd. Deze precursors slaan laag voor laag neer op de nanodeeltjes. Bij de ontwikkeling van de reactor die, anders dan de meer gangbare ALD reactoren, niet wordt gebruikt om vaste substraten maar individuele nanodeeltjes te coaten, is enerzijds zorggedragen voor een veilig ontwerp en anderzijds voor flexibiliteit en toegankelijkheid voor de mogelijkheid om het proces op verschillende manieren te monitoren en controleren.

Met behulp deze reactor zijn silica (SiO_2) nanodeeltjes gecoat met 1.6 nm dikke TiO_2 lagen. De groeisnelheid van de lagen is 0.32 Å per ALD cyclus en onafhankelijk van de pulstijd van de precursors. Analyse met de elektronenmicroscop (TEM) laat zien dat de deeltjes een zogenaamde core-shell structuur hebben waarbij de kern van SiO_2 omgeven wordt door een homogene, dichte laag van TiO_2 .

Om te laten zien dat elektrisch geleidende coatings kunnen worden aangebracht op nanodeeltjes zijn met dezelfde depositietechniek geleidende TiN lagen aangebracht op SiO_2 deeltjes. In dit geval hebben we TDMAT en ammonia (in plaats van water) gebruikt als precursors. De groeisnelheid van TiN is onafhankelijk van de TDMAT en NH_3 dosis, maar neemt af naarmate het aantal depositiecycli toeneemt. Dit verschijnsel kan worden toegeschreven aan vorming van bijproducten die kunnen adsorberen op het oppervlak van de nanodeeltjes en daar vervolgens de adsorptie van precursors verhinderen. De TiN-gecoate deeltjes vertonen goede elektrische geleiding, waarbij de weerstand afhangt van de depositie-omstandigheden.

De resultaten van dit onderzoek zijn een eerste stap op weg naar het gebruik van FB-ALD in de synthese van core-shell nanodeeltjes, waarvan de meest veelbelovende toepassingen batterijen en nanogestructureerde derdegeneratie zonnecellen zijn. In vervolgstudies zal enerzijds moeten worden gekeken naar technologische vraagstukken met betrekking tot de productie van de deeltjes en anderzijds, op fundamenteel niveau, zal de optimale core-shell structuur bepaald moeten worden.

De fundamentele vragen hebben betrekking op de elektronische structuur van nanomaterialen. Op basis van het normale gedrag van de materialen kan immers niet

voorspeld worden hoe materialen zich op nanometerschaal gaan gedragen. Uit fundamentele studies en op basis van berekeningen van de elektronische structuur, kan per toepassing gekeken worden welke core-shell materiaalcombinaties het meest veelbelovend zijn om te maken. Synthese van deze core-shell deeltjes kan worden gedaan met behulp van een kleinschalige fluidized bed ALD reactor.

Op technologisch gebied dient vooral gekeken te worden naar het veiligheidsaspect van het werken met losse nanodeeltjes, in het bijzonder als de deeltjes gemaakt zijn van toxische stoffen of van stoffen die spontaan kunnen ontbranden bij contact met lucht. Dit is vooral van belang bij het inbrengen van de deeltjes en bij het verwijderen van de gecoate deeltjes na de reactie. Het belang van een goed strategie om contact met lucht te voorkomen is al gebleken uit de experimenten met TiN op nanodeeltjes waarbij de deeltjes spontaan ontbrandden nadat ze in aanraking gekomen waren met lucht.

Een andere, meer praktische uitdaging is het beheersbaar maken van agglomeratie van nanodeeltjes en het creëren van een stabiel, homogeen fluide bed op grote schaal. Op labschaal zijn er, naast het vibrerend fluide bed zoals beschreven in dit proefschrift, verschillende technieken om agglomeraten op te breken en het fluide bed te homogeniseren waarvan zal moeten worden bekeken hoe deze opgeschaald kunnen worden. Verder is de statische hoogte (drukval) van fluide bedden op grote schaal groter dan de druk waarbij ALD reactoren bij voorkeur geopereerd worden. Er zal moeten worden uitgezocht wat dit relatief grote drukverschil voor invloed heeft op de homogeniteit van het fluide bed.

Al met al is FB-ALD, ondanks de technologische uitdagingen die de opschaling van de techniek nog biedt, een veelbelovende techniek waarbij de flexibiliteit in materiaalkeuze en de grote homogeniteit van de deeltjes een groot voordeel zijn.

REFERENCES

1. P. Colombari, *J. Nano Res.* **8**, 109- (2009).
2. E. Rikkinen, A. Santasalo-Aarnio, S. Airaksinen, M. Borghei, V. Viitanen, J. Sainio, E. I. Kauppinen, T. Kallio and A. O. I. Krause, *J. Phys. Chem. C* **115** (46), 23067-23073 (2011).
3. V. Polshettiwar and R. S. Varma, *Green Chem.* **12** (5), 743-754 (2010).
4. A. Z. Moshfegh, *J. Phys. D: Appl. Phys.* **42** (23), 233001 (2009).
5. A. S. Arico, P. Bruce, B. Scrosati, J.-M. Tarascon and W. van Schalkwijk, *Nature Mater* **4** (5), 366-377 (2005).
6. S. S. Mao and X. Chen, *Int. J. Energy Res.* **31** (6-7), 619-636 (2007).
7. S. X. Wang and G. Li, *IEEE Transactions on Magnetics* **44** (7), 1687-1702 (2008).
8. T. Trindade, P. O'Brien and N. L. Pickett, *Chem. Mater.* **13** (11), 3843-3858 (2001).
9. S. Magdassi, M. Grouchko and A. Kamyshny, *Materials* **3** (9), 4626-4638 (2010).
10. T. A. P. F. Doll, S. Raman, R. Dey and P. Burkhard, *J. Royal Soc. Interface* **10** (80) (2013).
11. V. Sanna and M. Sechi, *Nanomed. Nanotechnol.* **8**, **Supplement 1** (0), S31-S36 (2012).
12. F. Yang, C. Jin, S. Subedi, C. L. Lee, Q. Wang, Y. Jiang, J. Li, Y. Di and D. Fu, *Cancer Treat. Rev.* **38** (6), 566-579 (2012).
13. J. L. Vivero-Escoto, R. C. Huxford-Phillips and W. Lin, *Chem. Soc. Rev.* **41** (7), 2673-2685 (2012).
14. M. Perfezou, A. Turner and A. Merkoci, *Chem. Soc. Rev.* **41** (7), 2606-2622 (2012).
15. E. C. Dreaden, A. M. Alkilany, X. Huang, C. J. Murphy and M. A. El-Sayed, *Chem. Soc. Rev.* **41** (7), 2740-2779 (2012).
16. H. Jans and Q. Huo, *Chem. Soc. Rev.* **41** (7), 2849-2866 (2012).
17. N. Lee and T. Hyeon, *Chem. Soc. Rev.* **41** (7), 2575-2589 (2012).
18. T. L. Doane and C. Burda, *Chem. Soc. Rev.* **41** (7), 2885-2911 (2012).
19. A. J. Nozik, *Chem. Phys. Lett.* **457** (1-3), 3-11 (2008).
20. H. W. Hillhouse and M. C. Beard, *Curr. Opin. Colloid In.* **14** (4), 245-259 (2009).
21. E. Talgorn, Y. Gao, M. Aerts, L. T. Kunnean, J. M. Schins, T. J. Savenije, M. A. van Huis, H. S. J. van der Zant, A. J. Houtepen and S. L. D. A., *Nat. Nano* **6** (11), 733-739 (2011).
22. A. J. Nozik, *Physica E* **14** (1-2), 115-120 (2002).
23. C. A. Amarnath, S. S. Nanda, G. C. Papaefthymiou, D. K. Yi and U. Paik, *Crit. Rev. Sol. State* **38** (1), 1-56 (2013).
24. N. Ma, A. F. Marshall, S. S. Gambhir and J. H. Rao, *Small* **6** (14), 1520-1528 (2010).
25. H. Khurshid, C. G. Hadjipanayis, H. Chen, W. Li, H. Mao, R. Machaidze, V. Tzitzios and G. C. Hadjipanayis, *J. Magn. Magn. Mater.* **331** (0), 17-20 (2013).
26. A. Pandey and P. Guyot-Sionnest, *Science* **322** (5903), 929-932 (2008).

27. S. Wei, Q. Wang, J. Zhu, L. Sun, H. Lin and Z. Guo, *Nanoscale* **3** (11), 4474-4502 (2011).
28. H. Zhang, M. Jin and Y. Xia, *Chem. Soc. Rev.* **41** (24), 8035-8049 (2012).
29. K. Tedsree, T. Li, S. Jones, C. W. A. Chan, K. M. K. Yu, P. A. J. Bagot, E. A. Marquis, G. D. W. Smith and S. C. E. Tsang, *Nat Nano* **6** (5), 302-307 (2011).
30. J. R. Wank, S. M. George and A. W. Weimer, *Powder Technol.* **142** (1), 59-69 (2004).
31. D. M. King, X. H. Liang and A. W. Weimer, *Powder Technol.* **221**, 13-25 (2012).
32. Image from NanoComposix via <http://nanocomposix.com/products/gold/silica-coated/17-nm>
33. R. L. Puurunen, *J. Appl. Phys.* **97** (12), 121301-121353 (2005).
34. D. R. G. Mitchell, D. J. Attard and G. Triani, *Thin Solid Films* **441** (1-2), 85-95 (2003).
35. R. L. Puurunen, T. Sajavaara, E. Santala, V. Miikkulainen, T. Saukkonen, M. Laitinen, Leskel and Markku, *J. Nanosci. Nanotechnol* **11** (9), 8101-8107 (2011).
36. J. Aarik, A. Aidla, H. Mändar and T. Uustare, *Appl. Surf. Sci.* **172** (1-2), 148-158 (2001).
37. N. G. Kubala, P. C. Rowlette and C. A. Wolden, *J. Phys. Chem. C* **113** (37), 16307-16310 (2009).
38. J. Aarik, A. Aidla, T. Uustare, K. Kukli, V. Sammelselg, M. Ritala and M. Leskelä, *Appl. Surf. Sci.* **193** (1-4), 277-286 (2002).
39. Q. Xie, J. Musschoot, D. Deduytsche, R. L. Van Meirhaeghe, C. Detavernier, S. Van den Berghe, Y.-L. Jiang, G.-P. Ru, B.-Z. Li and X.-P. Qu, *J. Electrochem. Soc.* **155** (9), H688-H692 (2008).
40. J. J. Yang, N. P. Kobayashi, J. P. Strachan, M. X. Zhang, D. A. A. Ohlberg, M. D. Pickett, Z. Y. Li, G. Medeiros-Ribeiro and R. S. Williams, *Chem. Mater.* **23** (2), 123 (2011).
41. C.-S. Lee, J. Kim, J. Y. Son, W. Choi and H. Kim, *Appl. Catal. B: Environ.* **91** (3-4), 628-633 (2009).
42. V. R. Rai and S. Agarwal, *J. Phys. Chem. C* **112** (26), 9552-9554 (2008).
43. J. Aarik, A. Aidla, T. Uustare, M. Ritala and M. Leskelä, *Appl. Surf. Sci.* **161** (3-4), 385-395 (2000).
44. Q. Xie, Y. L. Jiang, C. Detavernier, D. Deduytsche, R. L. Van Meirhaeghe, G. P. Ru, B. Z. Li and X. P. Qu, *J. Appl. Phys.* **102** (8), 083521-083256 (2007).
45. C. J. Howard, T. M. Sabine and F. Dickson, *Acta Crystall. B* **47** (4), 462-468 (1991).
46. J. Driessen, J. Schoonman and K. F. Jensen, *J. Electrochem. Soc.* **148** (3), G178-G184 (2001).
47. V. Sammelselg, A. Rosental, A. Tarre, L. Niinistö, K. Heiskanen, K. Ilmonen, L. S. Johansson and T. Uustare, *Appl. Surf. Sci.* **134** (1-4), 78-86 (1998).
48. K. S. Finnie, G. Triani, K. T. Short, D. R. G. Mitchell, D. J. Attard, J. R. Bartlett and C. J. Barbé, *Thin Solid Films* **440** (1-2), 109-116 (2003).
49. J. Dendooven, S. P. Sree, K. De Keyser, D. Deduytsche, J. A. Martens, K. F. Ludwig and C. Detavernier, *J Phys. Chem. C* **115** (14), 6605-6610 (2011).

50. H.-E. Cheng, C.-M. Hsu and Y.-C. Chen, *J Electrochem. Soc.* **156** (8), D275-D278 (2009).
51. H. Kim, *J Vac. Sci. Technol. B* **21** (6), 2231-2261 (2003).
52. R. G. Gordon, D. Hausmann, E. Kim and J. Shepard, *Chem. Vap. Dep.* **9** (2), 73-78 (2003).
53. K. E. Elers, V. Saanila, P. J. Soininen, W. M. Li, J. T. Kostamo, S. Haukka, J. Juhanoja and W. F. A. Besling, *Chem. Vap. Dep.* **8** (4), 149-153 (2002).
54. S. B. S. Heil, J. L. v. Hemmen, C. J. Hodson, N. Singh, J. H. Klootwijk, F. Roozeboom, M. C. M. v. d. Sanden and W. M. M. Kessels, *J Vac. Sci. Technol. A* **25** (5), 1357-1366 (2007).
55. J. Musschoot, Q. Xie, D. Deduytsche, S. Van den Berghe, R. L. Van Meirhaeghe and C. Detavernier, *Microelectron. Eng.* **86** (1), 72-77 (2009).
56. M. Ritala, M. Leskelä, E. Rauhala and P. Haussalo, *J. Electrochem. Soc.* **142** (8), 2731-2737 (1995).
57. J. W. Elam, M. Schuisky, J. D. Ferguson and S. M. George, *Thin Solid Films* **436** (2), 145-156 (2003).
58. K.-E. Elers, J. Winkler, K. Weeks and S. Marcus, *J Electrochem. Soc.* **152** (8), G589-G593 (2005).
59. H. Van Bui, A. W. Groenland, A. A. I. Aarnink, R. A. M. Wolters, J. Schmitz and A. Y. Kovalgin, *J. Electrochem. Soc.* **158** (3), H214-H220 (2011).
60. E. Langereis, S. B. S. Heil, M. C. M. van de Sanden and W. M. M. Kessels, *J. Appl. Phys.* **100** (2), 10 (2006).
61. M. Bosund, A. Aierken, J. Tiilikainen, T. Hakkarainen and H. Lipsanen, *Appl. Surf. Sci.* **254** (17), 5385-5389 (2008).
62. A. Satta, J. Schuhmacher, C. M. Whelan, W. Vandervorst, S. H. Brongersma, G. P. Beyer, K. Maex, A. Vantomme, M. M. Viitanen, H. H. Brongersma and W. F. A. Besling, *J. Appl. Phys.* **92** (12), 7641-7646 (2002).
63. H. M. Hayes and D. R. Lide, *CRC Handbook of Chemistry and Physics*. (2015).
64. S. Logothetidis, E. I. Meletis, G. Stergioudis and A. A. Adjaottor, *Thin Solid Films* **338** (1-2), 304-313 (1999).
65. V. Miikkulainen, M. Leskela, M. Ritala and R. L. Puurunen, *J. Appl. Phys.* **113** (2), 021301 (2013).
66. D. Kunii and O. Levenspiel, *Fluidization Engineering*, 2 ed. (Butterworth-Heinemann Boston, 1991).
67. M. F. Llop, F. Madrid, J. Arnaldos and J. Casal, *Chem. Eng. Sci.* **51** (23), 5149-5157 (1996).
68. R. B. Bird, W. E. Stewart and E. N. Lightfoot, *Transport Phenomena*, 2 ed. (John Wiley & Sons Inc., Hoboken, NJ 2002).
69. L. F. Hakim, J. L. Portman, M. D. Casper and A. W. Weimer, *Powder Technol.* **160** (3), 149-160 (2005).
70. K. Kusakabe, T. Kuriyama and S. Morooka, *Powder Technol.* **58** (2), 125-130 (1989).
71. W. Yao, G. Guangsheng, W. Fei and W. Jun, *Powder Technol.* **124** (1-2), 152-159 (2002).

72. J. Jung and D. Gidaspow, *J Nanopart. Res.* **4** (6), 483-497 (2002).
73. C. Zhu, Q. Yu, R. N. Dave and R. Pfeffer, *AIChE J.* **51** (2), 426-439 (2005).
74. J. R. van Ommen, J. Valverde and R. Pfeffer, *J. Nanopart. Res.* **14** (3), 1-29 (2012).
75. I. Repins, M. A. Contreras, B. Egaas, C. DeHart, J. Scharf, C. L. Perkins, B. To and R. Noufi, *Prog. Photovolt.* **16** (3), 235-239 (2008).
76. D. Cunningham, K. Davies, L. Grammond, E. Mopas, N. O'Connor, M. Rubcich, M. Sadeghi, D. Skinner and T. Trumbly, *Conf. Rec. of the Twenty-Eighth IEEE Photovoltaic Specialists Conference - 2000*, 13-18 (2000).
77. N. Golovan and V. Smyntyna, *Sensors Actuat. B-Chem.* **6** (1-3), 289-292 (1992).
78. B. K. Miremadi, K. Colbow and Y. Harima, *Rev. Sci. Instr.* **68**, 3898-3903 (1997).
79. X. F. Duan, C. M. Niu, V. Sahi, J. Chen, J. W. Parce, S. Empedocles and J. L. Goldman, *Nature* **425** (6955), 274-278 (2003).
80. F. Y. Gan and I. Shih, *IEEE T. on Electron Dev.* **49** (1), 15-18 (2002).
81. T. Ota, K. Takahash and K. Kobayash, *Solid-State Electron.* **15** (12), 1387 (1972).
82. E. Talgorn, R. D. Abellon, P. J. Kooyman, J. Piris, T. J. Savenije, A. Goossens, A. J. Houtepen and L. D. A. Siebbeles, *Acs Nano* **4** (3), 1723-1731.
83. B. P. Luther, S. E. Mohny and T. N. Jackson, *Semicond. Sci. Technol.* **13** (11), 1322-1327 (1998).
84. F. Fillot, T. Morel, S. Minoret, I. Matko, S. Maitrejean, B. Guillaumot, B. Chenevier and T. Billon, *Microelectron. Eng.* **82** (3-4), 248-253 (2005).
85. J. Fritsche, D. Kraft, A. Thissen, T. Mayer, A. Klein and W. Jaegermann, *Thin Solid Films* **403**, 252-257 (2002).
86. R. K. Swank, *Phys. Rev.* **153** (3), 844 (1967).
87. S. Gupta, D. Patidar, N. S. Saxena and K. Sharma, *Chalcogenide Lett.* **6** (12), 723-731 (2009).
88. A. A. M. Farag, I. S. Yahia and M. Fadel, *Int. J. Hydrogen Energ.* **34** (11), 4906-4913 (2009).
89. S. Gupta, D. Patidar, N. S. Saxena, K. Sharma and T. P. Sharma, *Optoelectron. Adv. Mater.* **2** (4), 205-208 (2008).
90. I. O. Oladeji, L. Chow, J. R. Liu, W. K. Chu, A. N. P. Bustamante, C. Fredricksen and A. F. Schulte, *Thin Solid Films* **359** (2), 154-159 (2000).
91. H. Khallaf, I. O. Oladeji, G. Y. Chai and L. Chow, *Thin Solid Films* **516** (21), 7306-7312 (2008).
92. I. O. Oladeji and L. Chow, *J. Electrochem. Soc.* **144** (7), 2342-2346 (1997).
93. K. S. Ramaiah, R. D. Pilkington, A. E. Hill, R. D. Tomlinson and A. K. Bhatnagar, *Mater. Chem. Phys.* **68** (1-3), 22-30 (2001).
94. M. D. Archbold, D. P. Halliday, K. Durose, T. P. A. Hase, D. Smyth-Boyle and K. Govender, *Conference Record of the Thirty-First IEEE Photovoltaic Specialists Conference - 2005*, 476-479 (2005).
95. N. B. Chaure, S. Bordas, A. P. Samantilleke, S. N. Chaure, J. Haigh and I. M. Dharmadasa, *Thin Solid Films* **437** (1-2), 10-17 (2003).
96. R. Ortegaborges and D. Lincot, *J Electrochem. Soc.* **140** (12), 3464-3473 (1993).
97. S. G. P. D. D. G. R. Mahieu, *Thin Solid Films* **515**, 1229-1249 (2006).
98. W. G. Spitzer and C. A. Mead, *J Appl. Phys.* **34** (10), 3061 (1963).

99. S. Gautier, P. Komninou, P. Patsalas, T. Kehagias, S. Logothetidis, C. A. Dimitriadis and G. Nouet, *Semicond. Sci. Technol.* **18** (6), 594-601 (2003).
100. J. Hu, M. Ameen, G. Leusink, D. Webb and J. T. Hillman, *Thin Solid Films* **308**, 589-593 (1997).
101. A. Paranjpe and M. Islamraja, *J Vac. Sci. Technol. B* **13** (5), 2105-2114 (1995).
102. D. K. Schroder, *Semiconductor material and device characterization*. (John Wiley & Sons Inc., New York, 1998).
103. D. W. Niles, G. Herdt and M. AlJassim, *J. Appl. Phys.* **81** (4), 1978-1984 (1997).
104. D. Lincot and R. O. Borges, *J. Electrochem. Soc.* **139** (7), 1880-1889 (1992).
105. C. H. Hsu and F. Mansfeld, *Corrosion* **57** (9), 747-748 (2001).
106. E. H. Roderick and R. H. Williams, *Metal-Semiconductor contacts*, 2 ed. (Oxford University Press, Oxford, 1988).
107. M. E. Ozsan, D. R. Johnson, M. Sadeghi, D. Sivapathasundaram, G. Goodlet, M. J. Furlong, L. M. Peter and A. A. Shingleton, *J. Mater. Sci.-Mater. El.* **7** (2), 119-125 (1996).
108. H. Chavez, M. Jordan, J. C. McClure, G. Lush and V. P. Singh, *J. Mater. Sci.-Mater. El.* **8** (3), 151-154 (1997).
109. E. H. Rhoderick and R. H. Williams, *Metal-Semiconductor Contacts*. (Oxford University Press, Oxford, 1988).
110. S. M. Sze, *Physics of Semiconductor Devices*. (John Wiley & Sons, New York, 1981).
111. S. K. Mandal, A. B. Maity, J. Dutta, R. Pal, S. Chaudhuri and A. K. Pal, *Physica Status Solidi A* **163** (2), 433-443 (1997).
112. B. K. Patel, K. K. Nanda and S. N. Sahu, *J. Appl. Phys.* **85** (7), 3666-3670 (1999).
113. R. H. Lammoreaux, D. L. Hildebrand and L. Brewer, *J. Phys. Chem. Ref. Data* **16** (3), 419-443 (1987).
114. Due to charge neutrality, oxygen atoms at anion sites (OSx) are not taken into account in this equation.
115. P. E. Lippens and M. Lannoo, *Phys. Rev. B* **39** (15), 10935 (1989).
116. H. P. Maruska, F. Namavar and N. M. Kalkhoran, *Appl. Phys. Lett.* **61** (11), 1338-1340 (1992).
117. M. F. Finlayson, B. L. Wheeler, N. Kakuta, K. H. Park, A. J. Bard, A. Campion, M. A. Fox, S. E. Webber and J. M. White, *J. Phys. Chem.* **89** (26), 5676-5681 (1985).
118. D. Meissner, R. Memming and B. Kastening, *J. Phys. Chem.* **92** (12), 3476-3483 (1988).
119. A. Paracchino, V. Laporte, K. Sivula, M. Gratzel and E. Thimsen, *Nature Materials* **10** (6), 456-461 (2011).
120. A. Paracchino, N. Mathews, T. Hisatomi, M. Stefiak, S. D. Tilley and M. Gratzel, *Ener. Environ. Sci.* **5** (9), 8673-8681 (2012).
121. K. Yu, X. Lin, G. Lu, Z. Wen, C. Yuan and J. Chen, *RSC Adv.* **2** (20), 7843-7848 (2012).
122. M. Shalom, S. Dor, S. Ru'he, L. Grinis and A. Zaban, *J. Phys. Chem. C* **113** (9), 3895-3898 (2009).
123. S. Hu, M. R. Shaner, J. A. Beardslee, M. Lichterman, B. S. Brunschwig and N. S. Lewis, *Science* **344** (6187), 1005-1009 (2014).

124. A. Paracchino, V. Laporte, K. Sivula, M. Grätzel and E. Thimsen, *Nat Mater* **10** (6), 456-461 (2011).
125. B. Diaz, E. Harkonen, V. Maurice, J. Swiatowska, A. Seyeux, M. Ritala and P. Marcus, *Electrochimica Acta* **56** (26), 9609-9618.
126. X. Du, K. Zhang, K. Holland, T. Tombler and M. Moskovits, *Appl. Opt.* **48** (33), 6470-6474 (2009).
127. C. X. Shan, X. Hou and K.-L. Choy, *Surf. Coat. Technol.* **202** (11), 2399-2402 (2008).
128. G. Bech-Nielsen, M. Jaskula, I. Chorkendorff and J. Larsen, *Electrochimica Acta* **47** (27), 4279-4290 (2002).
129. D. Meissner, R. Memming and B. Kastening, *J. Phys. Chem.* **92** (12), 3476-3483 (1988).
130. A. J. Bard and M. S. Wrighton, *J. Electrochem. Soc.* **124** (11), 1706-1710 (1977).
131. D. J. Fermin, E. A. Ponomarev and L. M. Peter, *J. Electroanal. Chem.* **473** (1-2), 192-203 (1999).
132. M. Avrami, *J. Chem. Phys.* **8** (2), 212-224 (1940).
133. Y.-M. Chiang, D. P. Birnie and W. D. Kingery, *Physical Ceramics: Principles for Ceramic Science and Engineering*. (John Wiley & Sons, 1996).
134. T. Inoue, T. Watanabe, A. Fujishima and K. Honda, *J. Electrochem. Soc.* **124** (5), 719-722 (1977).
135. X. Liang, Y. Zhou, J. Li and A. W. Weimer, *J. Nanopart. Res.* **13** (9), 3781-3788 (2011).
136. J. D. Ferguson, K. J. Buechler, A. W. Weimer and S. M. George, *Powder Technol.* **156** (2-3), 154-163 (2005).
137. L. F. Hakim, C. L. Vaughn, H. J. Dunsheath, C. S. Carney, X. Liang, P. Li and A. W. Weimer, *Nanotechnol.* **18** (34) (2007).
138. D. M. King, X. Liang, P. Li and A. W. Weimer, *Thin Solid Films* **516** (23), 8517-8523 (2008).
139. D. M. King, X. Liang, Y. Zhou, C. S. Carney, L. F. Hakim, P. Li and A. W. Weimer, *Powder Technol.* **183** (3), 356-363 (2008).
140. C. Wilson, D. Goldstein, J. McCormick, A. Weimer and S. George, *J. Vac. Sci. Technol. A* **26** (3), 430-437 (2008).
141. O. J. Kilbury, K. S. Barrett, X. W. Fu, J. Yin, D. S. Dinair, C. J. Gump, A. W. Weimer and D. M. King, *Powder Technol.* **221**, 26-35 (2012).
142. D. M. King, J. A. Spencer, X. Liang, L. F. Hakim and A. W. Weimer, *Surf. Coat. Technol.* **201** (22-23), 9163-9171 (2007).
143. M. K. Wiedmann, D. H. K. Jackson, Y. J. Pagan-Torres, E. Cho, J. A. Dumesic and T. F. Kuech, *J. Vac. Sci. Technol. A* **30** (1), 01A134 (2012).
144. R. Beetstra, U. Lafont, J. Nijenhuis, E. M. Kelder and J. R. van Ommen, *Chem. Vap. Dep.* **15** (7-9), 227-233 (2009).
145. W. J. Maeng and H. Kim, *Electrochem. Sol. St. Lett.* **9** (6), G191-G194 (2006).
146. C. H. Nam, R. Pfeffer, R. N. Dave and S. Sundaresan, *AIChE Journal* **50** (8), 1776-1785 (2004).
147. X. S. Wang, V. Palero, J. Soria and M. J. Rhodes, *Chem. Eng. Sci.* **61** (16), 5476-5486 (2006).

148. E. Jaraiz, S. Kimura and O. Levenspiel, *Powder Technol.* **72** (1), 23-30 (1992).
149. Y. Mawatari, T. Koide, Y. Tatemoto, S. Uchida and K. Noda, *Powder Technol.* **123** (1), 69-74 (2002).
150. M. A. S. Quintanilla, J. M. Valverde, A. Castellanos, D. Lepek, R. Pfeffer and R. N. Dave, *Chem. Eng. Sci.* **63** (22), 5559-5569 (2008).
151. J. Y. Yun, M. Y. Park and S. W. Rhee, *J. Electrochem. Soc.* **146** (5), 1804-1808 (1999).
152. E. T. Norton and C. Amato-Wierda, *Chem. Mater.* **13** (12), 4655-4660 (2001).
153. F. Maury, F. D. Duminica and F. Senocq, *Chem. Vap. Dep.* **13** (11), 638-643 (2007).
154. Data obtained from SAFC Hitech, supplier of TDMAT
155. D. M. King, S. I. Johnson, J. Li, X. Du, X. Liang and A. W. Weimer, *Nanotechnol.* **20** (19), 195401 (2009).
156. D. M. King, X. Liang, C. S. Carney, L. F. Hakim, P. Li and A. W. Weimer, *Adv. Funct. Mater.* **18** (4), 607-615 (2008).
157. M. P. Diebold, R. A. Kwoka, S. R. Mehr and R. W. Vargas, *JCT Research* **1** (3), 239-241 (2004).
158. D. R. G. Mitchell, G. Triani, D. J. Attard, K. S. Finnie, P. J. Evans, C. J. Barbe and J. R. Bartlett, *Smart Mater. Struct.* **15** (1), S57 (2006).
159. M. M. Ren, Z. Zhou, X. P. Gao, W. X. Peng and J. P. Wei, *J. Phys. Chem. C* **112**, 5689-5693 (2008).
160. D. Longrie, D. Deduytsche and C. Detavernier, *J. Vac. Sci. Technol. A* **32** (1), 010802 (2014).
161. J. R. van Ommen, C. U. Yurteri, N. Ellis and E. M. Kelder, *Particuology* **8** (6), 572-577 (2010).
162. L. F. Hakim, S. M. George and A. W. Weimer, *Nanotechnol.* **16** (7), S375-S381 (2005).
163. L. F. Hakim, J. Blackson, S. M. George and A. W. Weimer, *Chem. Vap. Dep.* **11** (10), 420-425 (2005).
164. M. B. Cortie, J. Giddings and A. Dowd, *Nanotechnol* **21** (11), 115201 (2010).
165. S. V. Boriskina, H. Ghasemi and G. Chen, *Mater. Today* **16** (10), 375-386 (2013).
166. M. Q. Snyder, S. A. Trebukhova, B. Ravdel, M. C. Wheeler, J. DiCarlo, C. P. Tripp and W. J. DeSisto, *J. Power Sources* **165** (1), 379-385 (2007).
167. D. Longrie, D. Deduytsche, J. Haemers, P. F. Smet, K. Driesen and C. Detavernier, *ACS appl. Mater. Interf.* **6** (10), 7316-7324 (2014).
168. T. Heil and H. Kohl, *Ultramicroscopy* **110** (7), 745-750 (2010).
169. J. Zhao, E. G. Garza, K. Lam and C. M. Jones, *Appl. Surf. Sci.* **158** (3-4), 246-251 (2000).
170. F. Grillo, M. T. Kreutzer and J. R. van Ommen, *Chem. Eng. J* **268**, 384-398 (2015).
171. L. A. Okada and S. M. George, *Appl. Surf. Sci.* **137** (1-4), 113-124 (1999).
172. S. Eichenlaub, C. Chan and S. P. Beaudoin, *J. Colloid Interf. Sci.* **248** (2), 389-397 (2002).
173. J. Visser, *Powder Technol* **58** (1), 1-10 (1989).
174. L. Assaud, K. Pitzschel, M. Hanbucken and L. Santinacci, *ECS J. Sol. State Sci. Technol.* **3** (7), 253-258 (2014)

DANKWOORD

Een proefschrift schrijf je nooit alleen. Daarom wil ik deze plek gebruiken om een aantal mensen te bedanken die hebben bijgedragen aan de totstandkoming ervan.

Allereerst wil ik mijn promotor en dagelijks begeleider Roel van de Krol bedanken: ik heb veel bewondering voor jouw drive, passie voor de wetenschap en doorzettingsvermogen, maar ook voor je openheid en eerlijkheid. Onze samenwerking was af en toe stormachtig, maar altijd leerzaam.

Mijn dankbaarheid gaat ook uit naar Bernard Dam: jij hebt een grote voorliefde voor het goede in het leven. Goede wetenschap door de goede vragen te stellen, goede presentaties met de goede plaatjes, maar ook goede relaties, goede werksfeer, goed eten, goede kunst. Hiermee maak je van MECS ook een goede groep om in te werken.

Ik wil ook graag mijn dank uitspeken aan de leden gebruikerscommissie: Wim Besling (NXP) en Diana Nanu (AST). Jullie inzichten en bijdragen aan de bijeenkomsten en papers zijn erg gewaardeerd. De bouw van de FB-ALD reactor die aan de basis staat van dit proefschrift is voor het grootste deel gedaan door de mensen van AST: Ben Meester, Ad Hendrikx en Heino van der Meer. De TEM-opnames die zijn gebruikt in hoofdstuk 4 zijn gedaan Monja Kaiser (Phillips Innovation Service) en bekostigd door NXP.

Joost Middelkoop en Herman Schreuders: jullie technisch inzicht, handigheid en geduld zijn onmisbaar geweest voor mij. Also many thanks for the MECS group: Heleen, my room mates: Yevheniy, Lennard, Sander, and Joris, our two eminent part-time group members Wim Haije and Hans Geerlings, the master students Hemme Battjes and Jeroen van de Waterbeemd and all the other group members for creating a social, friendly, inspiring atmosphere.

I would also like to thank Philipp Hillebrand (Helmholtz-Zentrum Berlin) for the XPS measurements in chapters 3 and 5, and Markus Wollgarten (Helmholtz-Zentrum Berlin) for the TEM images of the core-shell particles in chapter 5.

Aletta Wubben, onze gesprekken zijn heel verhelderend geweest. Jouw levensles “gedachten zijn krachten” heeft mij al heel vaak verder geholpen. Dank daarvoor.

Ik ben zeer dankbaar voor mijn familie en mijn vrienden. De vreugde die jullie bieden is van grote waarde en ik hoop daar nog lang van te kunnen genieten.

Sanne, als laatste wil ik jou bedanken voor de liefde, de zorg en het vertrouwen dat je me altijd weer geeft. Je weet niet half hoeveel dat voor me betekent.

CURRICULUM VITAE

Arjen Didden was born on August 17, 1981 in Koudekerk aan den Rijn, the Netherlands. After high school he studied chemical engineering at the Hague University of Applied Sciences, where he obtained his Bachelor of Applied Sciences in 2005. He wrote his bachelor thesis on the production of phenol with a Ti-silicalite catalyst at the Shell Research and Technology Centre Amsterdam.



He continued his studies at the Delft University of Technology where he obtained his Master of Science degree in January 2008. He wrote his Master thesis on the production of hydrogen through photoelectrochemical water splitting on a Fe_2O_3 photo-anode, under the supervision of Prof dr. ir. Roel van de Krol, Prof Dr. Joop Schoonman, and dr. Yongqi Liang.

After graduating, he started his PhD research at the Delft University of Technology in the group Materials for Energy Conversion and Storage. He was supervised by Prof. dr. ir. Roel van de Krol and prof. dr. Bernard Dam. The results of his research are presented in this thesis.

Arjen currently works as an R&D Engineer at Frames, where he is working on the development of natural gas treatment technologies.

PUBLICATIONS

Arjen Didden, Hemme Battjes, Raymond Machunze, Bernard Dam, and Roel van de Krol: TiN: a new Ohmic contact material for n-type CdS, *Journal of Applied Physics* **110** (2011) 033717

Arjen P. Didden, Joost Middelkoop, Diana E. Nanu, Wim F.A. Besling, and Roel van de Krol: Fluidized-Bed Atomic Layer Deposition Reactor for the Synthesis of Core-Shell Nanoparticles, *Review of Scientific Instruments* **85** (2014) 013905

Arjen Didden, Philipp Hillebrand, Bernard Dam, and Roel van de Krol: Photocorrosion mechanism of TiO₂-coated photoanodes, *International Journal of Photoenergy* **2015** (2015) 457980

Arjen Didden, Philipp Hillebrand, Markus Wollgarten, Bernard Dam and Roel van de Krol: Deposition of conductive TiN shells on SiO₂ nanoparticles with a fluidized bed ALD reactor, accepted for publication in *Journal of Nanoparticle Research* (2015)